Universidad de Santiago de Compostela
FACULTAD DE FÍSICA
Departamento de Física de Partículas

Pre- and postsaddle fission dynamics using lead on proton reactions in complete kinematic measurements

José Luis Rodríguez Sánchez

Septiembre de 2015


USC
UNIVERSIDADE
DE SANTIAGO
DE COMPOSTELA

Universidad de Santiago de Compostela
FACULTAD DE FÍSICA
Departamento de Física de Partículas

Pre- and postsaddle fission dynamics using lead on proton reactions in complete kinematic measurements

Memoria presentada por:
José Luis Rodríguez Sánchez
como disertación para optar al
Grado de Doctor
en Ciencias Físicas
Septiembre de 2015


USC
UNIVERSIDADE
DE SANTIAGO
DE COMPOSTELA

USC
UNIVERSIDADE
DE SANTIAGO
DE COMPOSTELA

UNIVERSIDAD DE SANTIAGO DE COMPOSTELA

José Benlliure, Catedrático de Física Atómica, Molecular y Nuclear de la Universidad de Santiago de Compostela

CERTIFICA:
que la memoria titulada **Pre- and postsaddle fission dynamics using lead on proton reactions in complete kinematic measurements** ha sido realizada bajo su dirección por **José Luis Rodríguez Sánchez** en el **Departamento de Física de Partículas de esta Universidad** y constituye el trabajo de **tesis** que presenta para optar al grado de **Doctor en Ciencias Física**.

Santiago de Compostela, a 21 de Septiembre de 2015

Fdo. José Benlliure

Fdo. José Luis Rodríguez Sánchez

USC
UNIVERSIDADE
DE SANTIAGO
DE COMPOSTELA

Acknowledgments

I wish to acknowledge the help provided by the people who participated in this work. First of all I would like to express my gratitude to the people who participated in the SOFIA and ANDES experiments. Without their great experience and motivation this work would not have been possible. I also wish to express my sincere gratitude to the members of the committee who evaluated and commented this thesis.

I would like to express my very great gratitude to my supervisor Prof. José Benlliure, who gave me the opportunity to work in the fascinating world of nuclear physics. Thanks to him I joined the Experimental group of Nuclei and Particles (GENP) at the University of Santiago de Compostela, where I developed this work.

I am particularly grateful to Laurent Audouin, Guillaume Boutoux, Gilbert Bélier, Audrey Chatillon, Fanny Farget, Thomas Gorbinet, Andreas Heinz, Aleksandra Kelić-Heil, Beatriz Jurado, Nick Kurz, Benoit Laurent, Julie-Fiona Martin, Eric Pellereau, Carme Rodríguez-Tajes, Karl-Heinz Schmidt, Julien Taïeb and Bernd Voss for everything I learned from them during the development of this work.

And of course, I especially thank my colleagues of the GENP group: Hector Álvarez, Yassid Ayyad, Saúl Beceiro, Juan Manuel Boillos, Pablo Cabanelas, Manuel Caamaño, Javier Cortes, Enrique Casarejos, Dolores Cortina, Paloma Díaz, Ignacio Durán, Beatriz Fernández, David González, Piotr Konczykowski, Esther Leal, Juan Llerena, Magdalena Mostazo, Vanesa Nimo, Juan Ramón Pereira, Xesus Pereira, Benjamin Pietras, Carlos Paradela, Diego Ramos, Marisol Robles, Hanan Saleh, Raquel Sorribas, Diego Tarrío and Jossitt Vargas for all the great moments we shared together. I wish you all the best in your future.

Finalmente, me gustaría agradecer a mis padres y a mi familia el apoyo incondicional que me han demostrado durante todos estos años. Gracias a ellos pude llegar hasta aquí.


USC
UNIVERSIDADE
DE SANTIAGO
DE COMPOSTELA

Contents

List of publications

Proton-induced fission cross sections on ^{208}Pb at high kinetic energies, Physical Review C **90**, 064606 (2014).

Abstract:
Total fission cross sections of ^{208}Pb induced by protons have been determined at 370A, 500A, and 650A MeV. The experiment was performed at GSI Darmstadt where the combined use of the inverse kinematics technique with an efficient detection setup allowed us to determine these cross sections with an uncertainty below 6%. This result was achieved by an accurate beam selection and registration of both fission fragments in coincidence which were also clearly distinguished from other reaction channels. These data solve existing discrepancies between previous measurements, providing new values for the Prokofiev systematics. The data also allow us to investigate the fission process at high excitation energies and small deformations. In particular, some fundamental questions about fission dynamics have been addressed, which are related to dissipative and transient time effects.

Complete characterization of the fission fragments produced in reactions induced by ^{208}Pb projectiles on proton at 500A MeV, Physical Review C **91**, 064616 (2015).

Abstract:
The two fragments produced in fission reactions induced by ^{208}Pb projectiles impinging on a liquid hydrogen target at 500A MeV have been fully identified in coincidence. The experiment was performed at GSI Darmstadt, where the combined use of the inverse kinematics technique with an efficient detection setup permitted one to detect and to fully identify the fission fragments in a range from $Z = 27$ to $Z = 52$. The corresponding isotopic cross sections and velocities of the fission fragments were measured with high accuracy. The results are compared to state-of-the-art model calculations that reproduce the measured observables. Correlations between the two fragments were used to assess the role of charge polarization and the excitation energy gained by the nascent fragments using the neutron excess of the final fragments.

The analysis of the average velocities of the fission fragments allowed us to parametrize the distance between the two fission fragments at scission as a function of the size of the fissioning system.

Constraining the level density using fission of lead projectiles, Physical Review C **92**, 044612 (2015).

Abstract:

The nuclear level density is one of the main ingredients for the description of the fission process. In this work, we propose to constrain the description of this parameter using fission reactions induced by protons and light ions on ^{208}Pb at high kinetic energies. The experiment was performed at GSI (Darmstadt), where the combined use of the inverse kinematics technique with an efficient detection setup allowed us to measure the atomic number of the two fission fragments in coincidence. This measurement permitted us to obtain the partial fission cross sections and the width of the charge distribution as a function of the atomic number of the fissioning system with high precision. These data and others previously measured, covering a large range in fissility, are compared to state-of-the-art calculations. The results reveal that total and partial fission cross sections cannot unambiguously constrain the level density at ground-state and saddle-point deformations and additional observables, such as the width of the charge distribution of the final fission fragments, are required.

Pre- and postsaddle dissipative effects in fission using complete kinematic measurements, in preparation.

Abstract:

We take advantage of the complete characterization of the two final fission fragments, and in particular their kinematic properties, to access the configuration of the fissioning system at scission. This information together with total fission cross sections and widths of the charge distributions characterizing the fissioning system at saddle will be used to investigate the saddle-to-scission dynamics.

Measurement of light-charged particles emitted in coincidence with fission reactions induced by ^{208}Pb projectiles on protons at 500A MeV , in preparation.

Abstract:

The multiplicities of light-charged particles emitted in coincidence with fission reactions will be used as an additional and independent observable to investigate the fission hindrance at high excitation energies.

List of Figures


USC
UNIVERSIDADE
DE SANTIAGO
DE COMPOSTELA

List of Tables


USC
UNIVERSIDADE
DE SANTIAGO
DE COMPOSTELA

Introduction

Since the discovery of nuclear fission by Hahn, Strassmann and Meitner in 1939 [1], the progress in the understanding of the fission process has not ceased to be stimulated by new experimental results. Although the explanation of nuclear fission on the basis of the liquid-drop model was provided very soon by Bohr and Wheeler [2], new experimental observations revealed more and more the complexity of nuclear fission and created new challenges for theory. The investigation of different experimental observables such as pre- and postscission neutron multiplicities [3], giant dipole resonance (GDR) γ-ray emission [4, 5], multiplicities of charged particles [6], fission and evaporation cross sections [7, 8, 9] established that the dynamical evolution of the fissioning system cannot be explained just in terms of the statistical model of Bohr and Wheeler [2], suggesting that the fission process requires a dynamical approach based on the coupling of intrinsic and collective excitations of the nuclear constituents. Here, transport theories [10] based on Fokker-Plank or Langevin equations have proven to be a suitable tool for the description of the collective evolution of nuclei.

However, the fission process is still far from being fully understood and our theoretical and experimental knowledge is not yet complete. Several works provided evidence that the nuclear friction parameter or the viscosity of the medium could change with the nuclear deformation or with the nuclear temperature [11]. These ideas are still under debate because they could be biased by experimental conditions. The measurement of different observables with high precision and accuracy, such as fission probabilities, masses and atomic numbers of the fission fragments, as well as their total kinetic energies, and γ-rays and light particles emitted during the fission process, is still limited by the available technology. Some examples are fission cross sections and isotopic distributions of fission fragments. Currently, the measurements of fission cross sections using different techniques or setups are not consistent [12].

On the other hand, information on full isotopic distributions of fission fragments is scarce. First experiments, yielding isotopic distributions, were performed at the mass spectrometer Lohengrin [13] at the Institut Laue-Langevin based on thermal-neutron induced reactions [14, 15]. This technique only allowed one for the identification of the light fission fragments because the velocities of the heavy ones are too small to correlate any measurable energy loss with their atomic number. In some cases, some isotopic yields of the heavy fragments could be obtained with radio-chemical techniques [16, 17] or β-delayed γ spectroscopy [18], but with limited precision. Therefore, a significant improvement is needed to address the existing discrepancies in some observables, but also to measure complete isotopic distributions of fission fragments, which may extend the present limits of our understanding of the fission process.

In the late 1990s, with the advance of heavy ion accelerators a new generation of experimental approaches for fission studies was developed, where the use of the inverse kinematics technique permits one a correct identification of the fission fragments in-flight. The first measurements based on this technique were performed at the GSI facilities in Darmstadt (Germany) using the FRS spectrometer [19], where only one of the two fragments was detected and identified in mass and charge by the FRS. However, these measurements provided relevant information on the fission process [20, 21, 22]. To go a step further, an effort has been made recently by the SOFIA collaboration at GSI [23, 24, 25, 26] to overcome the restrictions of conventional fission experiments in order to obtain complete isotopic measurements of both fission fragments.

In the present work, we have investigated the fission of ^{208}Pb at relativistic energies. The experiment was conducted at GSI by using a novel setup especially designed for the investigation of fission in inverse kinematics. This setup allowed us to separate fission from other reaction channels and to facilitate the unambiguous identification of both fission fragments in atomic and mass numbers. The two fission fragments were detected simultaneously with high efficiency and acceptance. These measurements permitted us to obtain the total fission cross sections for the reaction ^{208}Pb($370A$, $500A$, and $650A$ MeV) + p and for the reaction ^{208}Pb($500A$ MeV) + ^{27}Al with high precision. These results are very important for the characterization of spallation targets used as neutron sources.

The total and partial fission cross sections, the width of the charge distributions of the fission fragments and light-charged particle multiplicities are used to investigate dissipative effects at small deformations, between the ground-state and saddle-point configurations. The charge identification of both fission fragments allowed us to reconstruct the atomic number of the fissioning system. This observable is strongly related to the excitation energy gained by the compound nuclei and to the impact parameter [27, 28].

The correlations of the fission cross sections and width of the charge distributions with the atomic number of the fissioning system are used to explore the influence of the excitation energy, where the use of different targets and different beam energies favors this study. We also use the total and partial fission cross sections and width of the charge distributions of the fission fragments to investigate the role of the level densities in fission, in particular the description of the level-density parameter.

The mass and atomic-number identification of the two fission fragments together with their velocities also permitted us to investigate dissipative effects at large deformations, between the saddle-point and scission configurations. Up to now this kind of study has been only performed with fusion-fission reactions using a limited number of observables, such as the mass distribution of the fission fragments or the neutron multiplicities. However, the large angular momentum gained by the compound nucleus could affect the conclusions drawn from such experiments. In the present work the use of spallation reactions, where the fissioning systems are produced with low angular momentum, small deformations and large excitation energies, favors the study of dissipation and also allowed us to define new observables, such as the pre- and postscission neutron multiplicities and the neutron excess of the final fission fragments as a function of the atomic number of the fissioning system. These new observables are used to investigate the value of the dissipation parameter at large deformations. In addition, we also use the isotopic distributions of the final fission fragments and their velocities to study the impact of postscission neutron evaporation and to obtain information on the scission configuration.

The present dissertation is organized as follows: In chapter 1, a review of the basic ideas concerning the dynamics of the fission process at high excitation energies, and different experimental approaches to measure them, are discussed. Chapter 2 includes a detailed description of the experimental setup employed to measure the two fission fragments and the light-charged particles of the reactions described above. Chapters 3 and 4 are dedicated to the experimental results, including both discussions about the physics related with each observable, as well as the sensitivity of each of them to the parameters that affect to the fission process. In particular, chapter 3 is dedicated to investigate the dynamics of the fission process at small deformations, between the ground-state and saddle-point configurations, using the total and partial fission cross sections, the width of the charge distributions of the fission fragments and light-charged particle multiplicities. The objective of chapter 4 is to investigate dissipative effects at large deformations, between the saddle-point and scission configurations, using new observables such as the pre- and postscission neutron multiplicities and the neutron excess of the final fission fragments as a function of the atomic number of the fissioning system. In addition, the isotopic distributions of the final fission fragments and their velocities are used to assess the scission configuration. Finally, chapter 4.5 is dedicated to the conclusions of this work and to forthcoming measurements at the FAIR facilities [29] using knockout reactions like $(p, 2p)$.

Chapter 1

The fission process at high excitation energies

Fission constitutes the most glaring case of a large-scale collective motion in nuclei, where the production of two fission fragments allows a clear identification of this deexcitation mechanism univocally. During the last years, this fact has permitted to introduce a large variety of experimental observables sensitive to the dynamical evolution of the fission process as a result of the development of the experimental techniques. In the following chapter, the most important theoretical and experimental features to study the fission process at high excitation energies are explained together with some related results. The first part of this chapter, section 1.1, is devoted to the current understanding of the nuclear fission process. The most important ingredients of the fission mechanism are introduced, such as the dissipation concept and the nuclear level density, as well as their observed effects. Section 1.2 provides a view of the most used observables for the investigation of the dynamics of the fission process. Finally, in section 1.3, an overview of the reaction mechanism, experimental technique and model calculations used in this work are described.

1.1 Current understanding of fission

During fission a heavy nucleus evolves towards large deformations before splitting into two fragments with comparable mass, as a consequence of the large-scale collective motion of the nucleus constituents. The evolution of the process depends on the initial conditions of the fissioning compound nuclei, such as its mass and atomic numbers, excitation energy and angular momentum, and on the form of its potential-energy landscape that is usually a function of the deformation and mass asymmetry. Historically, several distinctive types of fission were identified, such as particle-induced fission [1, 30], spontaneous fission [31], spontaneously fissioning isomers [32], β-delayed fission [33, 34], electromagnetical-induced fission (Coulomb excitation or Coulex) of radioactive nuclei at relativistic energies [23, 35], photofission [36], and a surrogate type of fission [37, 38].

The experimental techniques used to measure fission can be divided into direct and inverse kinematics. The first experiments were performed using the direct kinematics technique. Among the most outstanding ones, we can mention studies at the mass spectrometer Lohengrin [13] at the Institut Laue-Langevin using thermal-neutron induced reactions [14, 15], where only the light fission fragments were identified in mass and atomic number. The Neutron Time-of-Flight (n_ToF) facility at CERN, which has a long flight path and an intense spallation neutron source [39] that covers a continuous energy range from thermal energies up to 1 GeV, with great accuracy. In this case the fission measurements were carried out with several detectors, such as the Parallel Plate Avalanche Counters (PPACs) [40], Fast Ionization Chambers (FIC) [41] and MicroMegas [42]. This setup, together with a high-intensity neutron flux, made it possible to measure cross sections of neutron-induced reactions in highly radioactive materials. However, these detectors limited the study of fission to the angular distribution of the fission fragments and the cross section of the reaction [40, 43, 44]. Other facilities, such as Los Alamos National Laboratory [45, 46], the Svedberg Laboratory at Uppsala University [47], the Joint Research Center Institute for Reference Materials and Measurements at Geel [48], and the Cyclotron Research Center at Louvain-la-Neuve [49] also investigated fission using neutron-induced reactions. In these cases, the fission products and their cross sections were determined by using ionization chambers [50, 51]. With respect to proton-induced fission, we can mention the CERN Isotope mass Separator On-Line (ISOLDE) facility [52] that allows one the selection of nuclei with a specific mass number A produced in proton-induced fission reactions, although usually no Z selection is obtained. Recently, the coupling of a resonance ionization laser ion source [53] to ISOLDE allows for unique isomer separation, which provides the fission yields for the selected element [54, 55, 56]. Furthermore, we can mention the Ion Guide Isotope Separator On-Line (IGISOL) facility [57] at Jyväskylä, whose technique was also utilized to determine fission yields at the Louvain-la-Neuve cyclotron facility [58], at the Cyclotron and Radioisotope Center in Tohoku University [59], and at the SARA facility [60] in Grenoble.

In the late 1990s, the inverse kinematics technique allowed one for a correct identification of the fission fragments in-flight. The first measurements based on this technique were performed at the GSI facilities in Darmstadt using electromagnetic-, fragmentation- and spallation-induced fission reactions, where the FRS spectrometer [19] was used to detect and to identify one of the two fragments in terms of its mass and charge. Recently, new experiments at GANIL also take advantage of the inverse kinematics technique together with transfer- and fusion-induced fission reactions [61, 62, 63, 64]. One of the fission fragments is identified in mass and atomic number using the spectrometer VAMOS [65], while the second fragment is only identified in atomic number by energy-loss measurements. To go a step further, an effort was made by the SOFIA collaboration at GSI [23, 24, 25, 26] in 2012 to overcome the restrictions of conventional fission experiments. A novel setup, especially designed for the investigation of fission in inverse kinematics, was used to separate fission from other reaction channels and to facilitate the identification of the two fission fragments in atomic and mass number using the spectrometer ALADIN [66], as will be discussed in chapter 2.

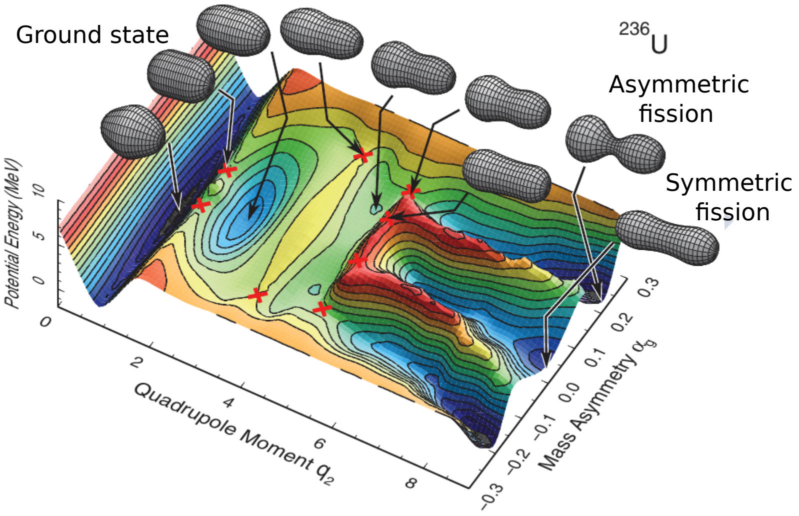

Figure 1.1: *(Color online). Potential-energy landscape for ^{236}U as a function of the dimensionless quadrupole deformation and the mass-asymmetry coordinate. Figure adapted from Ref. [67].*

Fission is the unique tool to probe the nuclear potential-energy landscape and its evolution, as a complex function of elongation, mass asymmetry, spin, and excitation energy, from a single compound system beyond the fission barrier and further to the scission point, culminating in the formation of fission fragments. This evolution involves a subtle interplay of collective (macroscopic) and single-particle (microscopic) effects, such as pairing and shell effects. The latter are responsible for the observed asymmetric-mass distributions for some fissioning isotopes. As shown in Fig. 1.1, the evolution of the process is guided by the potential-energy landscape of the corresponding nucleus, which is a function of the quadrupole deformation and the mass-asymmetry coordinate. The population of the different valleys represented in the potential landscape depends on the initial excitacion energy gained by the compound nucleus with respect to the ground state. As can be seen, lower excitation energies correspond to asymmetric fission modes while high excitation energies result in symmetric contributions. Therefore, fission enables the study of nuclear-structure effects in the heaviest nuclei [68] and in isotopes relevant for the astrophysical r-process [69]. Moreover, fission is a very powerful mechanism to produce nuclei far from the stability line [52]. Apart from its importance for fundamental studies, fission also has many practical applications in medicine.

On the other hand, fission at high excitation energies is extremely important for the development of spallation neutron sources in Accelerator Driven System (ADS) technologies [70]. These neutron sources use spallation reactions of high-energy protons on a heavy target (made of lead, bismuth or tantalum) to produce the amount of neutrons needed to maintain a nuclear chain reaction [71]. Therefore, a good knowledge of the interaction of protons with these materials is mandatory for their characterization. Reactions leading to fission are of interest because they contribute to the production of hazardous remnants, in particular gaseous ones, such as the isotopes of Kr and Xe. The production of these isotopes could be also obtained with fission model calculations, however, one needs to validate these models with accurate data to improve their reliability.

1.1.1 Fission models

The availability of heavy-ion beams in different energy ranges and the emergence of exclusive measurements motivated the development of different microscopic and macroscopic theoretical approaches.

Microscopic theories for large amplitude motion of many body systems are usually based on a mean field description known as time-dependent Hartee-Fock method [72] developed in the 1970s. Application of the time-dependent Hartee-Fock equation requires a large mean free path and hence is a good approximation for low-energy heavy-ion collisions. Recently, this kind of calculation has been improved with pairing effects [73, 74, 75] to provide a more realistic description of fission, however, shell effects are also required [20]. On the other hand, at high collision energies, the mean free path is strongly reduced due to the large excitation energies involved in the process.

Thus the inclusion of residual two-body collisions in a self-consistent mean-field theory is essential for a more realistic description of heavy-ion collisions at high excitation energies [76]. However, because of numerical difficulties to solve the equations, realistic applications of these approaches seem to be difficult even with the fastest available computers.

On the other hand, macroscopic theories based on transport equations [10, 77] were also developed in the 1970s to describe the fission process using a small number of variables. In these theories one distinguishes between collective or macroscopic and intrinsic or microscopic degrees of freedom, where the latter are considered as a heat bath. The collective degrees of freedom of the nucleus correspond to the coordinate motion of part or all the nucleons, for example vibrations, rotations and all kind of deformations. The intrinsic degrees of freedom are the individual states of the nucleons. Here, one is faced with a self-consistency problem since the collective degrees of freedom are made up of the individual nucleons. The fundamental idea underlying the concept of dissipation is that the collective degrees of freedom and the heat bath are coupled, and thus excitation energy can be transferred between them. The process of transfer of energy between the collective degrees of freedom and the heat bath is named dissipation, which is quantified by a reduced dissipation coefficient β.

The most-widely used transport theories are based on the Langevin and Fokker-Planck equations [78]. The Fokker-Planck equation is a partial differential equation which can be solved analytically. On the other hand, the Langevin equations are stochastic differential equations and cannot be treated with analytic methods. This is possibly the reason why the Langevin approach was not used in nuclear physics for a long time. The study of the fission process using these two approaches lead to the investigation of dissipative effects and their dependences on temperature and deformation. In 1940, Kramers [79] developed the first transport theory, derived from the quasi-stationary solution of the Fokker-Planck equation, to describe nuclear fission. For decades, the Kramers' solution was used in most of the statistical fission models to calculate the fission decay width.

1.1.2 Nuclear potential and fission barriers

The nuclear potential energy is one of the most important ingredients for the description of nuclear fission. The potential energy was first described in terms of a liquid-drop model as the sum of a shape-dependent surface and Coulomb energy terms. This description was first invoked by Meitner and Frisch [80]. In this model the Coulomb and surface energies are expressed as an expansion of the reflection- and axially-symmetric shape in Legendre polynomials, where up to the fourth power in the lowest order polynomial was retained. Using this approximation, it was possible to determine the macroscopic part of the fission-barrier heights.

In the late 1960s, new developments in the liquid-drop model were performed by Cohen and collaborators [81] to include rotational effects. This model, the so-called rotating liquid-drop model, provided a simplified calculation of the potential energies of rotating nuclei. However, the comparison of the results of this model with experimental data from heavy-ion induced fission, such as fission and evaporation-residue cross sections, showed that the model overestimates the fission-barrier heights [82, 83]. This discrepancy was attributed to the finite range of the nuclear force and the diffuseness of the nuclear surface, which leads to a reduction of the potential energy [84]. For this reason the liquid-drop model was improved to take these facts into account. The surface energy was replaced by the Yukawa-plus-exponential nuclear energy, which models the effects of the finite range of the nuclear force, the nuclear saturation, and the finite surface thickness. The Coulomb energy was calculated for a charge distribution with a realistic surface diffuseness, and the moment of inertia was calculated for rigidly rotating nuclei with a realistic surface density profile. These changes provided a new version of the liquid-drop model, the so-called finite-range liquid-drop model [85]. The fission barriers calculated from this model of potential energy were found to be less than 1 MeV of those which reproduce fission and evaporation-residue cross sections most accurately for a variety of nuclei with masses ranging from 150 to above 200 [85].

Earlier in 1955, Swiatecki [86] suggested that a more realistic fission barrier could be obtained by adding a correction energy, so-called shell correction, to the fission barrier calculated with the liquid-drop model. This correction, which is responsible for the observed asymmetric mass distributions [87], was calculated as the difference between the experimentally observed nuclear ground-state mass and the mass given by the liquid-drop model. These effects are especially strong in low energy fission and are not expected to be significant at large excitation energies [88]. In 1967, Strutinsky [87] developed a macroscopic-microscopic method to calculate these shell corrections theoretically, and currently, the fission barriers calculated with the finite-range liquid-drop model [85] together with the shell corrections are most-widely used in model calculations at high excitation energies.

The potential-energy landscape can also be described using fully dynamical microscopic models based on Hartree-Fock and Hartree-Fock-Bogoliubov methods [74, 89, 90, 91] using reasonable effective nucleon-nucleon interactions [92, 93]. However, the precision of these theoretical models in the prediction of some key observables, such as the mass-yield curve of the fission fragments, is limited due to the complexity of the many-body calculations involved. Furthermore, a complete microscopic calculation demands tremendous computing time, even with the most powerful computers.

1.1.3 Nuclear level density

The nuclear level density also plays a key role in the theoretical modeling of fission and more generally in the decay of compound nuclei. At present, the most abundant information on level densities comes from the counting of low-lying levels and from neutron resonances [94, 95]. These techniques have also been extensively exploited to obtain the level-density parameter ($\widetilde{a}$), which relates the nuclear temperature (T) with the excitation energy (E^*) according to $E^* = \widetilde{a}T^2$, and to investigate the evolution of $\widetilde{a}$ with the excitation energy [96].

Different sophisticated models have been developed to calculate the nuclear level density. These models employ various techniques ranging from microscopic combinatorial methods [97] and Hartree-Fock approaches [98] to phenomenological analytical expressions [99]. It is desirable to model the nuclear density of states using a microscopic approach since it contains detailled information of nuclear levels. However, the amount of computing time needed for microscopic calculations limits the applicability of this approach. On the other hand, most of the studies related to nuclear reaction calculations prefer the analytical level density descriptions because they allow one to describe the experimental data very well for hundreds of different isotopes. Presently, two phenomenological models, the constant temperature model of Gilbert-Cameron [100] and the Fermi gas model [101] based on the Bethe formula, are used in the level-density calculations. In these models the excitation energy can be shifted to take the shell and pairing corrections according to Refs. [102, 103] into account.

According to the Fermi gas model [101], the level density can be calculated as a funtion of the excitation energy E^* and the angular momentum J, and is expressed as:

$$\rho(E^*, J) = \frac{J+1/2}{\sqrt{2\pi}\sigma^3} e^{-\frac{J(J+1)}{2\sigma^2}} \frac{\sqrt{\pi}}{12} \frac{e^S}{\widetilde{a}^{1/4} E^{*5/4}} \tag{1.1}$$

where σ^2 is the spin cut-off factor given by $\sigma^2 = \frac{\Im T}{\hbar^2}$ with $\Im$ as the moment of inertia of the nucleus and T the nuclear temperture, E^* is the excitacion energy of the system, S is the entropy and $\widetilde{a}$ is the level-density parameter in units of MeV^{-1}. Generally, this last parameter can be written as [104, 105]:

$$\widetilde{a} = \alpha_v A + \alpha_s B_s \cdot A^{2/3} + \alpha_k B_k A^{1/3} \tag{1.2}$$

where A is the mass of the nucleus and α_v, α_s and α_k are the coefficients that correspond to the volume, surface and curvature components of the single-particle level densities, respectively. The values of these coefficients were calculated by Ignatyuk [105] (α_v=0.095, α_s=0.073, and α_k=0 in units of MeV^{-1}) and are the most-frequently used in model calculations. In the equation, B$_s$ represents the ratio between the surface of the deformed nucleus and a spherical nucleus while B_k corresponds to the ratio between the integrated curvature of the deformed nucleus and a spherical nucleus.

In order to account for the role of collective excitations in the decay of excited compound nuclei, the level density of Eq. 1.1 is corrected using the vibrational and rotational enhancement factors according to:

$$\rho(E,J) = K_{vib} K_{rot} \rho(E,J)_{int} \tag{1.3}$$

where $\rho(E,J)_{int}$ is given by Eq. 1.1, K_{vib} represents the vibrational enhancement factor and K_{rot} corresponds to the rotational factor. For nuclei with highly deformed saddle point or with a large ground-state deformation the collective enhancement factor arises from the appearance of rotational bands above the intrinsic single-particle levels. In this case, the vibrational factor K_{vib} can be thus considered negligible while the rotational enhancement factor is calculated according to Refs. [106, 107] in terms of the rigid-body moment of inertia. By contrast, for spherical nuclei the collective motion is calculated on the basis of low-frequency vibrational modes. At present, the factor K_{vib} can be calculated from the statistical sum of harmonic vibrational modes [106] or by using phenomenological approaches [108].

1.1.4 Dynamical effects at high excitation energy

For a long time, the quasi-stationary solution of the Fokker-Planck equation proposed by Kramers [79] was coupled to the statistical evaporation model developed by Weisskopf [109] to explain experimental fission data. In this kind of model, the deexcitation of the compound nucleus depends on the decay width for each channel and the process follows a sequence of deexcitation steps until a minimum excitation energy is reached. However, in the 1980s, Weidenmüller and collaborators [10] followed the line of Kramers' approach and adopted the diffusion model to investigate how the quasi-stationary flow over the fission barrier is attained. Their study was motivated by experimental findings where the predictions based on the approach of Kramers overestimated particle multiplicities [3]. They succeeded in obtaining a time-dependent solution of the two-dimensional Fokker-Planck equation after considering an initial system at ground-state deformation with high excitation energy and low angular momentum. Based on these assumptions, they found a time-dependent fission decay width $\Gamma_f(t)$ by calculating the probability flux across the saddle point. Their work showed that for finite values of the dissipation coefficient β, there is a delay or "transient time“ which elapses between the start of the induced fission process and the attainment of the stationarity fission flux across the barrier. This transient time manifests itself only at high excitation energies where the average decay time of the fissioning system is comparable to the relaxation time of its degrees of freedom, leading to a reduction of the fission probability. Further, experimental evidence for fission as a slow process came from measurements of prescission neutron multiplicities [110, 111, 112, 113, 114], charged particles [115], Giant Dipole Resonance (GDR) γ-rays [116, 117], fission fragment mass and kinetic energy distributions [113, 114], and evaporation residue cross sections [118].

On the other hand, the dynamics of the fission process does not end at the saddle point. As soon as the fissioning system passes the fission barrier, it evolves up to the scission point where the fission fragments are produced. Along this path, the fissioning system could still evaporate a few neutrons that will then contribute to the total and prescission neutron multiplicities. According to this idea, Grangé and collaborators [119, 120] considered that the emission of prescission neutrons should be related to the total fission time, which can be obtained as the sum of the fission lifetime calculated with the fission decay width and the average time needed by the fissioning system to descend from the saddle point to the scission point. The latter was calculated by Hofmann and Nix [121] by integrating the Fokker-Planck equation from the saddle point to the scission point. This model has been used in some works to investigate the value of the dissipation parameter at large deformations and the fission time scales [114, 120, 122, 123].

It is now well known that the gross features of the fissioning system can be described in terms of a small number of parameters, the so-called collective degrees of freedom. Dissipation represents the average effect of the interactions between the collective and intrinsic degrees of freedom. In this picture, the interaction between these degrees of freedom results in a fluctuating force influencing the collective dynamics, which in effect causes the diffusion of the dynamical coordinates (elongation, mass asymmetry, ...). Therefore, dissipation and diffusion are not independent of each other and, in fact, they are related through the Einstein's fluctuation-dissipation theorem [124].

Therefore, dynamical effects can be atributed to the dissipation mechanism. In this description, two kinds of dissipation mechanisms are generally considered in the dynamical models of nuclear reactions. One is the one-body dissipation and the other is the hydrodynamical two-body dissipation. The concept of the one-body dissipation mechanism was first introduced by Gross [125], who deduced a classical equation of motion including frictional forces from the general many-body Schrodinger equation for two colliding heavy ions. The interactions between the nucleons are approximated by using a mean-field potential and the collective dynamics is described by the shape evolution of this potential. On the other hand, hydrodynamical two-body dissipation models [126] are based on the assumption that nuclear dissipation arises from individual two-body collisions of nucleons. It was, however concluded, based on the analysis of extensive experimental data, that the hydrodynamical two-body viscosity cannot provide a consistent explanation of both neutron multiplicities and fission fragment kinetic energy distributions [127]. A strong two-body viscosity is required to reproduce the observed neutron multiplicities. Whereas, the total kinetic energy calculated with this value of two-body viscosity is far smaller than given by the Viola systematics [128]. A consistent explanation of neutron multiplicities and fragment kinetic energies rather supports one-body friction [129].

On the other hand, other questions such as the onset of dissipation and the temperature or deformation dependences of the dissipation parameter are still under debate [11]. A systematic study was carried out by Thoennessen et al. [4] to find the threshold excitation energy where the pure statistical model starts losing its validity. Their work opened up the problem of understanding the properties of nuclear dissipation and its dependence on the excitation energy. It was found that the ratio of the threshold temperature and the temperature-dependent fission barrier was independent of the mass of the fissioning nucleus and equal to 0.26. The authors suggested that this could reflect an onset of dissipation with increasing temperature. According to this conclusion, Hofman and collaborators [5] found an analytical expression for the temperature dependence of dissipation based on the study of γ-ray multiplicities associated with fusion-fission and quasifission reactions. According to this dependence, a dissipative parameter proportional to T or to T^2 could reproduce the experimental data rather well. However, the authors of Ref. [130] showed that this systematic behaviour could be explained without any assumption of an onset of dissipation effects or temperature dependence. This work also demonstrated that the reason why the statistical model fails to reproduce the experimental data for $T_{threshold}/B_f > 0.26$ is because at that point the dynamical delay time starts to be larger than the decay time predicted by the statistical model. These same conclusions were also found by Lestone and McCalla [8], who were able to describe evaporation and fission cross sections as well as light-charged particle multiplicities of fusion reactions without considering any temperature dependence of dissipation.

In contrast to this, the most recent works concerning the study of γ-ray multiplicities in fusion-fission reactions were interpreted assuming a deformation dependence of dissipation instead of a temperature dependence. Under this hypothesis, Shaw and collaborators [131] were able to reproduce the γ-ray multiplicity emitted in the fission of ^{240}Cf at different energies by using a value of $\gamma_{ground-saddle} = 2$ inside the saddle point and of $\gamma_{saddle-scission} = 5-10$ beyond the saddle point. Note that γ_i (where the subscript i denotes ground-saddle or saddle-scission) is related with the reduced dissipation parameter according to $\gamma_i = \beta_i/2\omega$, being ω the frequency of the inverted oscillator potential at the saddle point. Diószegi and co-workers [132] were able to investigate dissipation at small and large deformations by separating the presaddle and the saddle-to-scission γ-ray components. They used the evaporation-residue cross sections of the reaction ^{9}F + ^{181}Ta at 161 and 181 MeV to determine the dissipative parameter up to the saddle point, $\gamma_{ground-saddle} = 3$. Fixing this value of the dissipation coefficient at the saddle deformation, they varied the dissipation coefficient from saddle to scission to reproduce the γ-ray multiplicities obtaining $\gamma_{saddle-scission} = 10$. Such a deformation dependence with very low values of dissipation for the compact shapes up to saddle seems to be compatible with the results obtained by Fröbrich and collaborators [133]. These authors analyzed the prescission neutron multiplicities and fission probabilities with one-dimensional Langevin calculations coupled to a statistical evaporation code. They found that the experimental observables could only be described with a deformation-dependent dissipative parameter by considering a constant value $\beta_{ground-saddle} = 2 \times 10^{21}$ s^{-1} at small deformation, and a linear increase with the deformation when the fissioning system descends from the saddle to the scission point.

1.2 Experimental observables

The aim of this section is to introduce the most-widely used observables for investigating the dynamics of the fission process. As will be discussed, most of these observables are sensitive to dissipation and transient effects such as fission and evaporation-residue probabilities, post- and prescission particle multiplicities, γ-ray emission and fission fragment properties.

1.2.1 Fission and evaporation-residue cross sections

Fission and evaporation-residue cross sections are the most proposed observables suggested for the investigation of the effects of the nuclear dissipation during the evolution of the fissioning system from the ground state to the saddle point. Nuclear dissipation reduces the asymptotic value of the fission width predicted by the transition-state approach, that led to a reduction of the fission cross section and an increase of the complementary evaporation-residue cross section with respect to the statistical calculations. At high excitation energies ($E^* > 100$ MeV), the manifestation of the transient time also affects fission and evaporation-residue cross sections, increasing the effects mentioned above.

Benlliure and collaborators [134] investigated dissipation effects in spallation induced fission reactions using the inverse kinematics technique. The compound nuclei were produced in collisions of a ^{197}Au beam impinging on a proton target at relativistic energies. Evaporation and fission cross sections were investigated to extract information about the presaddle dynamics. However, the interpretation of dissipative effects by using fission and evaporation-residue cross sections needs the support of model calculations, where the initial conditions (excitation energy, angular momentum and deformation), the ratio of level-density parameter a_{sd}/a_{gs} (a_{sd} and a_{gs} denote the level-density parameter at the saddle-point and ground-state configurations, respectively) and the fission barriers play an important role. Therefore, Benlliure and co-workers [134] compared the data with different model calculations and inferred a dissipation strength of $\beta = 2 \times 10^{21}\mathrm{s}^{-1}$ and a transient time of $t_{trans} = (3 \pm 1) \times 10^{-21}\mathrm{s}$ by considering a step function to evaluate the time-dependent fission decay width. The effects of the level densities on the cross section were also investigated considering different ratios of level-density parameters at ground-state and saddle deformations (a_{sd}/a_{gs}). The authors found that the best description of the data was provided by the parametrization of the level-density parameter proposed by Ignatyuk et al. [105] coupled to the dissipative calculation mentioned above.

Based on these results, the model calculations were improved by Jurado and collaborators [135] including an analytical solution of the Fokker-Planck equation in order to extract realistic conclusions on dissipative and transient effects. In that case, a dissipation parameter of $\beta = 2 \times 10^{21}\mathrm{s}^{-1}$ and a transient time of $t_{trans} = (1.7 \pm 0.4) \times 10^{-21}\mathrm{s}$ were obtained [135]. A few years later, Schmitt and collaborators [136] showed that the quantitative values of the dissipation parameter and transient time obtained by Jurado and collaborators were affected by the initial deformation of the fissioning nuclei that were investigated, leading to new values of $\beta = 4.5 \times 10^{21}\mathrm{s}^{-1}$ and $t_{trans} = (3.3 \pm 0.7) \times 10^{-21}\mathrm{s}$ [137]. Recently, these results were confirmed by Ayyad and collaborators [138] using proton-induced fission cross sections of ^{181}Ta.

The value of the transient time was also investigate by Jing and collaborators [7] but using light-ion induced fusion-fission of pre-actinides, where the comparison of their fusion-fission cross sections with different model calculations led to a transient time of $t_{trans} = 10 \times 10^{-21}$s.

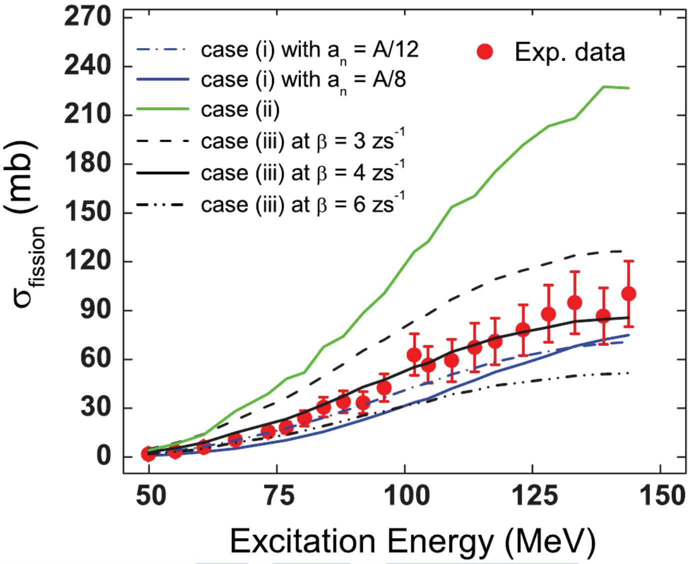

Figure 1.2: *(Color online). Fits to measured excitation function data of fission cross sections (denoted by red circles with error bars) in the* $^3He + {}^{197}Au$ *system [139]. Curves represent various theoretical calculations: case (i) statistical model without friction but with* $a_{sd}/a_{gs} = 1$, $a_{gs} = A/12$ *(dashed dotted blue line) and* $a_{gs} = A/8$ *(solid blue line); case (ii) statistical model without friction but with* $a_{sd}/a_{gs} \neq 1$ *(green line) and case (iii) Langevin model with* $a_{sd}/a_{gs} \neq 1$ *at friction strengths* $\beta = 3 \times 10^{21}\ s^{-1}$ *(dashed black line),* $4 \times 10^{21}\ s^{-1}$ *(solid black line), and* $6 \times 10^{21}\ s^{-1}$ *(dashed-double dot black line). Figure taken from Ref. [9].*

These dissipative effects have also been investigate in a very recent work performed by Ye and Wang [9] using fusion-fission cross sections of pre-actinides [139], as shown in Fig. 1.2. The authors combined the Langevin approach with a statistical decay model to investigate the dissipative effects and the impact of the level-density parameter. They showed that a statistical calculation coupled to different parametrizations of the level-density parameter cannot reproduce the data; cases (i) and (ii) in the figure. However, a dynamical calculation considering a reduced dissipative parameter of $\beta = 4 \times 10^{21}\text{s}^{-1}$ together with a description of the level-density parameter based on the parametrization given by Ignatyuk et al. [105] provides a satisfactory description of the data. Similar results for the dissipation parameter were also found by Lestone and McCalla [8] by using fusion-fission and fusion-evaporation cross sections of pre-actinides from $Z = 74$ to $Z = 84$. They compared the data with calculations performed with the statistical code JOANNE4 [140], extracting a dissipation parameter of $\beta = 3 \times 10^{21}\mathrm{s}^{-1}$.

1.2.2 Post- and prescission particle multiplicities and γ-ray emission

Fission of a compound nuclei formed in heavy-ion induced fusion reactions at energies above the Coulomb barrier has been investigated quite extensively, both experimentally and theoretically, during the last two decades. The multiplicities of prescission neutrons, light charged particles and γ-rays have been measured [110, 111, 112, 113, 114, 115, 116, 117] and compared with the predictions of statistical models [3, 6, 142]. These investigations have revealed that the statistical model of nuclear fission based on the transition-state method [2], where effects due to nuclear dissipation are not considered, is inadequate to describe fission of a highly excited heavy nuclei, and consequently dissipative dynamical models [127, 135, 141] are found to be essential to account for the experimental data.

The measurement of prescission particle and γ-ray multiplicities provides suitable clocks to probe the fission time scale and nuclear dissipation. Neutron and γ-ray clocks have been extensively described in the review articles of Hilscher and Rossner [3] and Paul and Thoennessen [142], respectively. Both authors compared the data with statistical and dynamical calculations and showed the need of considering nuclear dissipation in the fission process. Fröbrich and collaborators [133] also performed detailed studies about the influence of dissipation on prescission neutron, charged particle and γ-ray multiplicities, on the energy spectra of these particles, and on fission time distributions combining a Langevin approach with a statistical evaporation model. The authors also showed that a dynamical calculation considering dissipation provides a better description of the data. A very recent work performed by Vardaci and collaborators [143] also pointed out the same conclusion when combining the multiplicities of the light-charged particles with fission and evaporation residue cross sections.

On the other hand, Hinde and collaborators [144] investigated the sensivility of the prescission neutron multiplicities to the ratio of the level-density parameter at the ground-state and saddle-point deformations (a_{sd}/a_{gs}). The authors compared the prescission neutron multiplicities measured in fusion-fission reactions with statistical calculations varying the ratio a_{sd}/a_{gs}, showing that the prescission neutron multiplicities can change in a factor 2 varying the ratio a_{sd}/a_{gs} from 1 to 1.06.

1.2.3 Width of the fission fragment distributions

The temperature at the saddle point (T_{sad}) is a key parameter for understanding the fission dynamics because the modification of the fission probability during the transient time also alters the excitation energy (temperature) at the saddle point. However, one cannot directly measure T_{sad} and thus other observables are needed.

According to the statistical model [145], the widths of the mass and atomic-number distributions of the fission fragments (σ_A and σ_Z respectively) are related to the temperature at the saddle point, following the equations:

$$\sigma_A^2 = \frac{A_{fiss}^2 T_{sad}}{16 d^2V/d\nu^2} \quad and \quad \sigma_Z^2 = \frac{Z_{fiss}^2 T_{sad}}{16 d^2V/d\nu^2} \tag{1.4}$$

where $d^2V/d\nu^2$ is the second derivative of the potential with respect to the mass-asymmetry degree of freedom at the saddle point $\nu = (4/A_{fiss})/(M - A_{fiss}/2)$. A_{fiss} and Z_{fiss} correspond to the mass and atomic numbers of the fissioning nucleus, respectively, and M represents the mass number of the corresponding fragment. Due to the high probability of neutron evaporation compared to proton emission beyond the saddle-point configuration, the width of the atomic-number distribution of the fission fragments (σ_Z) is more suitable to constrain the temperature at the saddle point.

Based on these ideas, Benlliure and collaborators [134] used this observable to investigate dissipative effects in spallation reactions of ^{197}Au, but also to study the influence of the ratio of the level-density parameter at the ground-state and saddle-point deformations (a_{sd}/a_{gs}). They showed that the ratio of the level-density parameter calculated with the parametrization of Ignatyuk [105], together with a dynamical calculation considering dissipative effects, provide the best description of this observable. Based on this idea, Jurado et al. [27, 135] and Schmitt et al. [137] also investigated the dissipative and transient time effects but using peripheral relativistic heavy-ion collisions. In these works both fission fragments were measured with a novel experimental setup [35], similar to the one used in this work, which allowed to investigate this observable as a function of the atomic number of the fissioning system as shown in Fig. 1.3. The authors of these works demonstrated that dissipative and transient time effects are needed to reproduce the data (dashed lines). Recently, Ayyad and collaborators [28] also measured this observable for spallation reactions of ^{208}Pb on proton and deuterium targets at 500A MeV, showing that this observable is independent of the entrance channel. Therefore, this conclusion suggests that this observable could be used to constrain model calculations.

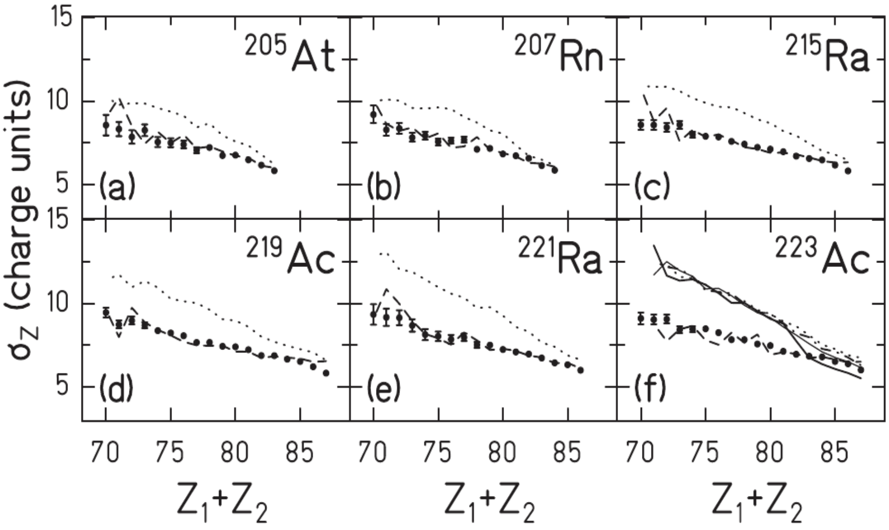

Figure 1.3: Width σ_Z plotted as a function of $Z_1 + Z_2$ for a set of radioactive beams. The data (large black dots) are compared to Kramers- (dotted line) and transient- (dashed line) type calculations, both assuming $\beta = 4.5 \times 10^{21}$ s^{-1}. For the ^{223}Ac secondary projectiles, additional Kramers-type calculations are shown with $\beta = 7 \times 10^{21}$ s^{-1} (dash-dotted line), $\beta = 10 \times 10^{21}$ s^{-1} (solid thin line) and $\beta = 20 \times 10^{21}$ s^{-1} (solid thick line). The staggering that can be observed in the calculations is attributable to statistical fluctuations only. Experimental error bars smaller than the symbols are not shown. Figure taken from Ref. [137].

1.3 Proposed investigation

1.3.1 Spallation and fragmentation reactions at relativistic energies

There exist several reaction mechanisms to excite nuclei and to induce fission. According to the work of Grangé and collaborators [146], the ideal conditions to investigate dissipative and transient time effects are high excitation energies ($E^* > 100$ MeV), low angular momentum and compound nuclei with small deformations. These same conditions could also be a good approach to investigate the role of the level-density parameter because the influence of the rotational and vibrational excitations on the level densities washes out at excitation energies around ∼40 MeV [108, 147].

These initial conditions are determined by the reaction mechanism. The most used mechanism to probe dissipative effects is the called fusion-fission reaction. The fissioning systems formed in this kind of reaction have a well-defined excitation energy, mass and atomic number and a broad angular momentum distribution. However, due to the characteristics of this reaction mechanism, the excitation energies are generally below 140 MeV. These conditions could prevent the manifestation of the effects of the transient time. If the fissioning system is produced by nucleon-transfer reactions the situation is similar to that of the fusion-fission reactions, although with lower excitation energies (below 80 MeV).

Spallation and fragmentation reactions at relativistic energies fulfill the conditions established by Grangé et al. [146] for the manifestation of dissipative and transient times effects. These reactions can be described as two-stage processes [148]. Initially, due to the fast interaction between the projectile and the target, a highly excited compound nucleus is well formed with a narrow shape distribution and with collective degrees in the ground state deformation. During the second stage, the thermalization and deexcitation of the system occur by evaporation of neutrons, light-charged particles, intermediate-mass fragments (IMFs), γ-ray emission and eventually by fission.

1.3.2 Complete kinematic measurements

In the present work, we have used a new experimental approach to perform complete kinematic measurements of the two fission fragments in coincidence with the emitted light particles. Different targets and beam energies were used to investigate the fission of ^{208}Pb, which allowed us to cover a wide range of excitation energy. These measurements are used to investigate the observables discussed above and to validate previous results on dissipation at small deformations. The new data are also used to investigate dissipative effects beyond the saddle point, at large deformations, and the impact of the postscission neutron evaporation on the isotopic distributions. Moreover, the measurement of the isotopic distributions of the fission fragments together with their velocities permits us to obtain relevant information on fission at the scission-point configuration.

1.3.3 Model calculations

The observables measured in this work allow us to characterize the fissioning nuclei at the saddle point (by measuring the fission cross sections and the width of the charge distribution of the fission fragments) and at the scission point (by investigating the isotopic composition and the velocities of the fission fragments). However, the initial conditions of the fissioning nuclei have to be based on reliable model calculations. These calculations are also used to interpret the measured observables in terms of dynamical variables such as the dissipation parameter and the transient time. Therefore, in this section we briefly describe the model calculations used in this work.

Spallation reactions are generally modeled as a two-stage process. In the first stage, nucleon-nucleon collisions inside the nucleus induce the loss of a few nucleons, which acquire kinetic energies that exceed their binding energy, resulting in the formation of excited prefragments [149, 150]. There are numerous models to calculate the distribution of excited prefragments before the decay process starts. The main differences among them are the accuracy of predicting the prefragments and the computing time. Some examples are pre-equilibrium models [151], intranuclear cascade models [149, 150, 152, 153, 154], abrasion models [155, 156], and models based on the Boltzmann-Uehling-Uhlenbeck (BUU) and Vlasov-Uehling-Uhlenbeck (VUU) transport equations [157, 158].

In this work we will use the Liège intranuclear cascade code INCL4.6 [159] because it represents a good compromise among accuracy, computing time and facility to be coupled to deexcitation models. This model describes the reaction between the proton and the lead nucleus as a series of independent nucleon-nucleon collisions, which leave an excited remnant nucleus at the end of the process. This nucleus usually deexcites by emitting particles or by fission. This process is described by the deexcitation code ABLA07 [160].

In the first stage, the interaction between the nucleons of the projectile and those of the target nucleus is described as a succession of binary collisions (and decays) between the nucleons along a complete cascade event. Particles are moving along straight-line trajectories between collisions inside the working sphere considering relativistic kinematics. The nucleons are divided into participants and spectators. When the participants leave the working sphere, they are considered as ejectiles and do not interact any more. Pions and Δ-resonances are produced during the nucleon-nucleon interactions, following the reactions $NN \rightleftharpoons N\Delta$ and $\Delta \rightleftharpoons \pi N$. For the nucleons and pions an average isospin-dependent potential well considering the reflection and/or transmission at the border of this potential is used. Pauli blocking is implemented to avoid the population of occupied final states and to reject unphysical situations. The code uses experimental threshold values for the emission of particles and separation energies, based on mass tables. Moreover, the model also considers the possibility of fusion reactions at low excitation energies.

The final excitation energy and angular momentum induced in the system at the end of the intranuclear cascade is determined by particle-hole excitations and holes produced in the initial Fermi distribution of the target. The evolution of every particle in the system is followed as time evolves and, at the end of the cascade process, the velocities of all emitted particles and the characteristics of the remnant nucleus are calculated. The cascade ends at a certain time named stopping time [150] determined in the code by a systematic investigation for different systems, incident energies and impact parameters. However, this time is modified at low excitation energies if the time of passage of the incident particle through the working sphere along a diameter exceeds the usual stopping time, by using the larger time.

In the deexcitation stage, described by the code ABLA07 [160], the emission of γ-rays, neutrons, light-charged particles and intermediate-mass fragments (IMFs) are calculated according to the Weisskopf formalism [109], which provides a good description of the evaporation residues produced in spallation and fragmentation reactions of nuclei from iron to uranium [134, 150, 161, 162, 163, 164]. The fission decay width is described by the Bohr-Wheeler transition-state model [2] following the formulation given by Moretto [165]:

$$\Gamma_f^{BW} = \frac{T}{2\pi}\frac{\rho_{sp}(E - B_f, J)}{\rho_{gs}(E, J)} \tag{1.5}$$

where $\rho_{sp}(E - B_f, J)$ and $\rho_{gs}(E, J)$ are the level densities at the saddle-point and ground-state configurations, respectively, and B_f is the fission-barrier height obtained from the finite-range liquid-drop model of Sierk [85] taking into account the influence of angular momentum and considering the ground-state shell effects [103]. The diffussion process above the fission barrier is described by the Fokker-Planck equation, where the quasi- stationary solution of this equation was introduced by Kramers [79] and provides a reduction of the fission decay width due to dissipation:

$$\Gamma_f^K = \left[\sqrt{1 + \left(\frac{\beta}{2\omega_0}\right)^2} - \frac{\beta}{2\omega_0}\right]\Gamma_f^{BW} \tag{1.6}$$

Here β is the reduced dissipation coefficient and ω_0 is the frecuency of the harmonic oscillator describing the inverted potential at the fission barrier. This equation provides the asymptotic value of the fission decay width.

The analytical approximation to the solution of the one-dimensional Fokker-Planck equation [166] for the time-dependent fission-decay width was developed by Jurado and collaborators in Refs. [135, 167], using a Gaussian distribution centred at the spherical shape as initial condition. The mean values and the widths of the initial Gaussian distributions in space and momentum are given by the entrance channel. In this approximation, the time-dependent fission-decay width is defined as:

$$\Gamma_f(t) = \frac{W_n(x = x_b; t, \beta)}{W_n(x = x_b; t \to \infty, \beta)} \Gamma_f^K \tag{1.7}$$

where W(x; t, β) is the normalized probability distribution at the saddle-point deformation x$_b$. The saddle-point deformations are calculated according to Ref. [168].

The level density is described as a function of the excitation energy and angular momentum, according to Eq. 1.1. The main parameter of that description is the level-density parameter that is modeled according to Eq. 1.2. The values for the coefficients α_v, α_s, and α_k are taken from Ref. [105]. Moreover, vibrational and rotational enhancement factors are also considered, according to Eq. 1.3. These factors are calculated based on the phenomenological description proposed by Junghans et al. [108].

The description of the properties of the fission fragments is based on a semi-empirical model developed by Benlliure and collaborators [169]. In this work we will only comment on the most important features related to the super-long fission channel, which dominates at high excitation energies. This fission channel can be explained by the macroscopic properties of the potential-energy landscape that is determined by the characteristics of the fissioning nucleus at the saddle point. In particular, the stiffness of the macroscopic potential along the mass-asymmetry degree of freedom is obtained from the systematics of the width of mass distributions measured in Ref. [170]. The neutron-to-proton ratio (N/Z) of the fission fragments is assumed to be given by the unchanged-charge distribution (UCD). This N/Z ratio is modified by the charge polarization effect calculated in terms of the liquid-drop model (LDM) by assuming a two touching spheres configuration at the scission point [171], and by the evaporation of particles during the descent from saddle to scission [160]. Finally, at the scission point, the two fission fragments are characterized by their atomic numbers $Z_{1,2}$, mass numbers $A_{1,2}$, kinetic energies $E_{kin}^{1,2}$, and excitation energies $E_{exc}^{1,2}$. After the formation of the two fission fragments, their corresponding deexcitation chains are followed until their excitation energies fall below the lowest particle-emission threshold.

The kinetic energies of the fission fragments are calculated according to the semi-statistical scission point model of Wilkins and collaborators [172]. The main contribution to the total kinetic energies released in the fission process comes from the Coulomb repulsion of the two fission fragments at the scission point and, therefore, this total kinetic energy is given by:

$$TKE \sim \frac{Z_1 Z_2}{D} \tag{1.8}$$

where Z_1 and Z_2 refer to the atomic number of the two fission fragments, and D is the distance between the two uniformly-charged spheroids representing the fission fragments. This distance is parametrized as:

$$D = r_0 A_1^{*1/3}\left(1+\frac{2\beta_1}{3}\right) + r_0 A_2^{*1/3}\left(1+\frac{2\beta_2}{3}\right) + d \tag{1.9}$$

where A_1^* and A_2^* refer to the mass number of the two fission fragments at the scission point, β_1 and β_2 are their quadrupole deformations at the scission point, r_0 is the fermi radius, and d is the distance between the tips of the two fission fragments.


USC
UNIVERSIDADE
DE SANTIAGO
DE COMPOSTELA

Chapter 2

New experimental approach

Despite decades of fission studies, information on full isotopic distributions of fission fragments is scarce. First experiments were performed at the mass spectrometer Lohengrin [13] at the Institut Laue-Langevin using thermal-neutron induced reactions [14, 15, 173, 174, 175, 176]. This technique only allowed one for the identification of the light fission fragments because the velocities of the heavy ones are too small to correlate any measurable energy loss with their atomic number. In some cases, the isotopic yields of some heavy fragments could be obtained with radio-chemical techniques [16, 17] or β-delayed γ spectroscopy [18], but with limited precision.

In the late 1990s, different experiments were performed at GSI using the FRS spectrometer [19] to investigate spallation-induced fission in inverse kinematics, accelerating heavy projectiles that impinged on liquid targets of hydrogen and deuterium. In these experiments only one of the two fragments was detected and identified in mass and charge by the FRS. This technique was improved using a novel setup to measure the atomic number of both fission fragments [35], while the FRS spectrometer [19] was used to produce and select secondary beams of fissile nuclei produced in fragmentation reactions of ^{238}U. This experiment allowed to investigate the role of shell effects in the charge distributions of the final fission fragments by Coulomb excitation of the incoming projectiles [20, 35, 177].

Recently, new experiments at GANIL also took advantage of the inverse kinematics technique together with transfer- and fusion-induced fission reactions [61, 62, 63, 64]. In these experiments transfer reactions were identified and reconstructed with an annular segmented silicon detector [63]. One of the fission fragments was identified in mass and atomic number using the spectrometer VAMOS [65], while the second fragment was only identified in atomic number by energy-loss measurements using an ionization chamber and silicon detectors. These experiments provided for the first time complete mass- and atomic-number distributions of the fission fragments and their corresponding kinematics for several actinides such as ^{240}Pu and ^{250}Cf [62].

To go a step further, an effort has been made recently by the SOFIA collaboration at GSI [23, 24, 25, 26] to overcome the restrictions of conventional fission experiments in order to obtain complete isotopic measurements of both fission fragments. This chapter is dedicated to the description of the experimental setup specially designed for the investigation of fission in inverse kinematics, which allowed us to separate fission from other reaction channels and to facilitate the identification of both fission fragments in atomic and mass numbers. Then we will explain the procedure to identify and select the fission events in order to reconstruct the fission fragments in atomic and mass numbers. Finally, we will describe the corrections and reconstruction method utilized in this work to determine the isotopic distribution of the fission fragments.

2.1 Description of the experimental setup

The experiment was performed at the GSI facilities in Darmstadt (Germany), where the SIS18 synchrotron was used to accelerate ions of ^{208}Pb up to 650A MeV with an intensity around 10^5 ions/s. The primary beam was then guided to Cave C where fission reactions were induced in a cylindrical target filled with liquid-hydrogen produced in a cryostat.

Figure 2.1 shows a top-view schematic representation of the detector setup [24, 25, 178] used in this experiment. The experimental setup is divided in two parts, one used to characterize the incoming beam ions and another dedicated to measure the fission fragments. The first part consists of a plastic scintillator detector (start) [179] used to measure the time-of-flight (ToF) of the fragments, a multisampling ionization chamber (MUSIC) [180] and a time projection chamber (TPC) [181]. These last two detectors provided the beam identification and its position on the target, respectively.

The second part consists of a double multisampling ionization chamber (Twin MUSIC) [182], two multiwire proportional counters (MWPCs) [178, 183], a large acceptance dipole magnet (ALADIN) [66] and a ToF Wall [179]. The Twin MUSIC chamber has a central vertical cathode that divides its volume into two active parts, segmented in ten anodes each. These anodes provided ten independent energy-loss and drift-time measurements, which allowed us to obtain the atomic numbers and the angles on the plane X-Z. MWPCs, situated in front and behind the dipole magnet, provided the horizontal (X) and vertical (Y) positions of the fission fragments. Finally, a

ToF Wall made of 28 plastic scintillators allowed us to measure the ToF of the fission fragments with respect to the start signal provided by the plastic scintillator located at the entrance of the experimental setup with a resolution around 40 ps (FWHM) [179]. The ALADIN magnet was set to a magnetic field of 1.6 T and its gap (200 cm long, 50 cm high and 100 cm wide) was filled with helium gas at atmospheric pressure.

In addition, two pipes, also filled with helium gas at atmospheric pressure, were mounted in front of the Twin MUSIC chamber and behind the dipole magnet ALADIN. The pipes were sealed by windows made of aluminized-mylar foils with a thickness of 35 μm and 50 μm, respectively. In all the cases, the helium gas was employed to reduce the energy and angular straggling of the fission fragments.

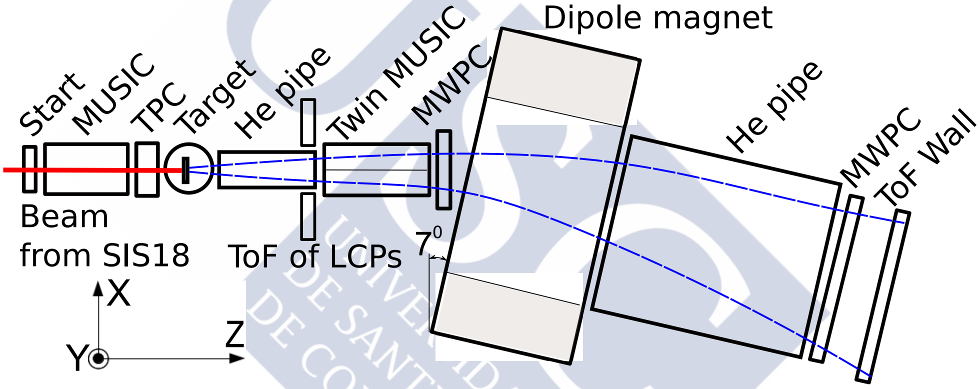

Figure 2.1: (Color online) Top schematic view of the used experimental setup. Sizes are not to scale.

Finally, light-charged particles emitted in coincidence with fission fragments were identified using a ToF wall detector (ToF of LCPs), placed in front of the Twin MUSIC chamber. This detector consisted of two detection planes of segmented plastic-scintillators, one with six horizontal paddles and another with six vertical paddles, which left a square hole in the center for the transmission of the fission fragments.

2.1.1 Twin MUSIC

The Twin MUSIC detector [182] (see the left pad of Fig. 2.2) is a double multisampling ionization chamber that was filled with P25 (74.5% of Argon, 25% of CH_4, and 0.5% of CO_2) gas during the experiment. The chamber was sealed by two windows made of aluminized-mylar foils with a thickness of 25

μm. This detector has a central vertical cathode with a thickness of 12 μm that divides its volume (60 cm long, 20 cm high and 20 cm wide) into two active parts, segmented in twelve anodes each as shown in the right pad of Fig. 2.2. The ten internal anodes were used for the read out of the induced signals, while the external anodes were used to preserve the homogeneity of the electric field inside the chamber. A Frisch-grid placed 0.5 cm in front of the anodes and connected to ground was used to reduce the position dependence of the primary ionization. The induced signal in each anode is read out by a preamplifier, which sends the signal to a fast spectroscopic amplifier (Mesytec MSCF-16). This amplifier divides the signal in two: one signal is integrated and sent to a MC32 Analog to Digital Converter (ADC) module while the other is sent to a Time to Digital Converter (TDC).

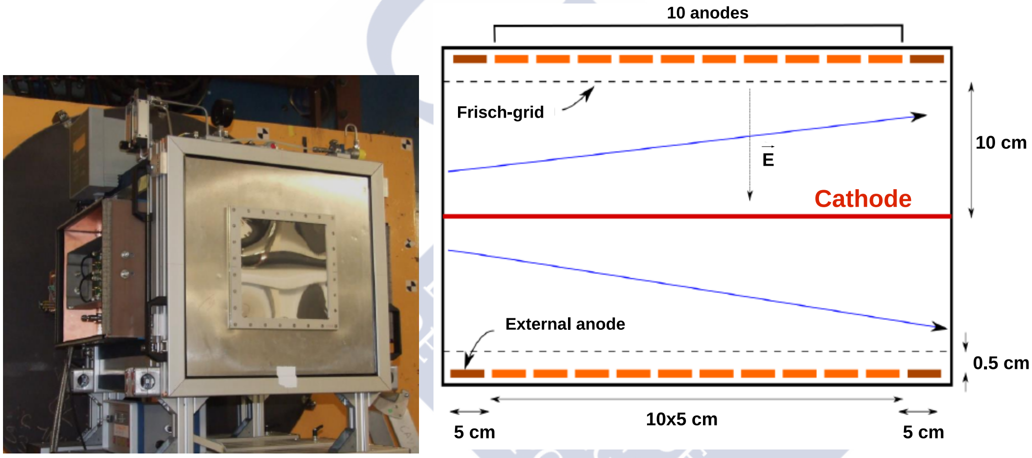

Figure 2.2: *(Color online) Left pad: Picture of the Twin MUSIC detector. Right pad: Schematic view of a multiwire chamber. The wires are connected to a positive voltage while the cathodes of the planes X and Y are connected to the preamplifiers to process the signals.*

The internal anodes provide ten independent energy-loss and drift-time measurements, which allowed us to obtain the atomic numbers with a resolution around 0.43 charge units full width at half maximum (FWHM) and the angles on the plane X-Z with a resolution below 0.6 mrad (FWHM).

2.1.2 MWPCs

MultiWire Proportional Counters (MWPCs) (see the left pad of Fig. 2.3), situated in front and behind the dipole magnet (see Fig. 2.1), provide the horizontal (X) and vertical (Y) positions of the fission fragments. The MWPC situated in front of the dipole magnet is 20 cm high and 20 cm wide while the MWPC situated behind the dipole magnet is 60 cm high and 90 cm wide, both detectors were designed to cover the angular acceptance of the fission fragments. During the experiment both MWPCs were filled with a mixture of Argon (80%) and CO_2 (20%) sealed by two windows made of aluminized-mylar foils with a thickness of 20 μm. The wires for obtaining the horizontal and vertical positions were separated a distance of 3.125 mm and 5 mm, in the horizontal and vertical planes respectively.

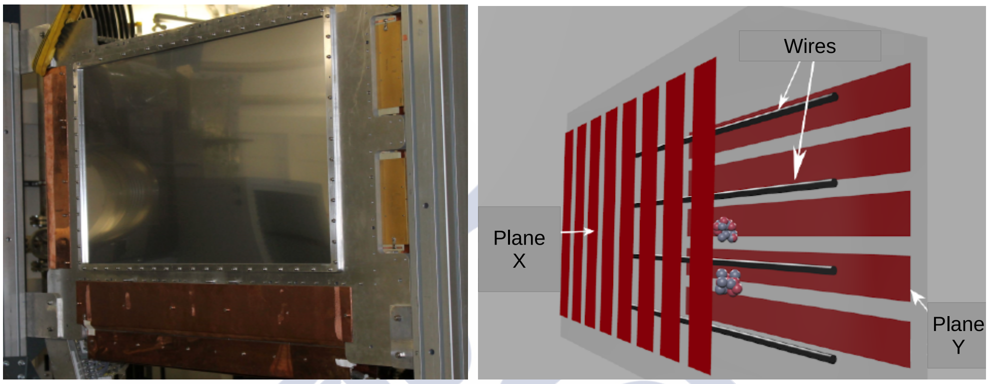

Figure 2.3: *(Color online) Left pad: Picture of the MWPC placed behind the dipole magnet. Right pad: Schematic view of a multiwire chamber. The wires were connected to a positive voltage while the cathodes of the planes X and Y were connected to the preamplifiers to process the signals.*

When the ions (fission fragments or primary beam) pass through the gas (see the right pad of Fig. 2.3), where there is an electric field imposed by a cathode plane (paths) and a plan anode (wires), different primary ionization electrons are created. These electrons are accelerated by the electric field around the wire, causing a localised avalanche. This avalanche induces a signal in the paths of the cathode whose amplitude decreases with the distance between the paths and the ion position. Using these signals, the ion trajectory can be found by computing the amplitudes from all the paths [184, 185]. For this work we have used the hyperbolic secant method described in Ref. [186].

2.1.3 ToF Wall for the fission fragments

The ToF Wall detector (see the left pad of Fig. 2.4) for the fission fragments was made of 28 ELJEN-232 plastic scintillators of 3.2 cm wide, 60 cm long and 0.5 cm thick disposed vertically in one plane covering an are of 60 cm (high) × 90 cm (wide), as shown in the right pad of Fig. 2.4. The scintillators were coupled to HAMAMATSU H6533 (9 paddles) and H10580 (19 paddles) fast photomultipliers in both extremes. The signal of the photomultipliers was read out by special TDCs (VFTX modules) built at GSI with a time resolution around 20 ps. These features allowed us to measure the ToF of the fission fragments with respect to the start signal provided by the plastic scintillator located at the entrance of the experimental setup (see Fig. 2.1) with a resolution around 40 ps (FWHM) [179] and the vertical position with a resolution of 3 mm (FWHM).

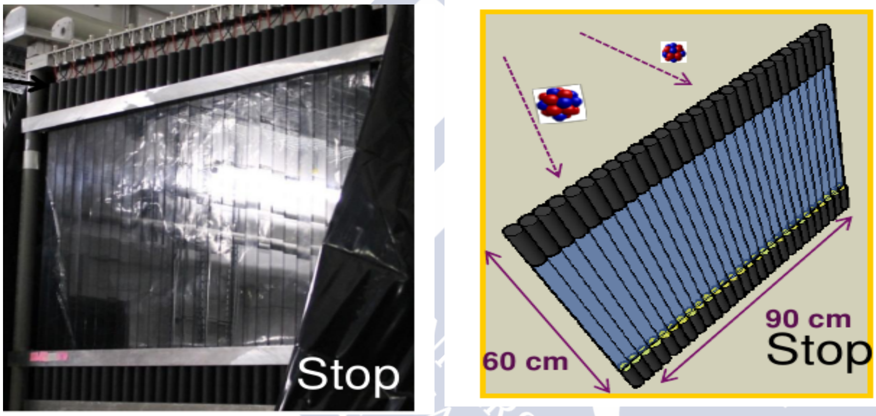

Figure 2.4: *(Color online) Left pad: Picture of the ToF Wall detector for the fission fragments. Right pad: Schematic view of the ToF Wall.*

2.1.4 ToF Wall detector for the light-charged particles

The ToF Wall detector (see Fig. 2.5) for the light-charged particles was placed in front of the Twin MUSIC chamber (see Fig. 2.1). This detector consists of two detection planes of segmented plastic-scintillators (50 cm long, 6 cm wide and 1 cm thick), one with six horizontal paddles and another with six vertical paddles, which leave a square hole (12.5 × 12.5 cm^2) in the center for the transmission of the fission fragments. Because of the reaction kinematics, most of the fission fragments go through the Twin MUSIC, while a large fraction of the light-charged particles escape the target to reach this ToF Wall. The scintillators were coupled to HAMAMATSU R8619 photomultipliers in both extremes to process their signals. The time and charge signals of the scintillators were registered by using a TDC (V795) and a QDC (V785), respectively.

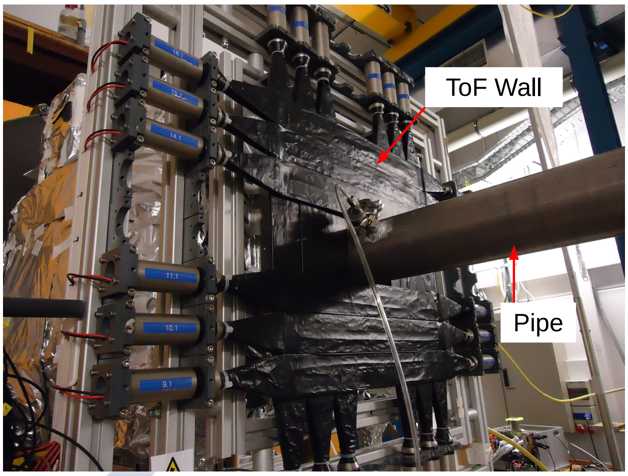

Figure 2.5: *(Color online) Picture of the ToF Wall detector used to detect the light-charged particles.*

2.2 Identification of the fission events

A good identification of the projectiles is needed to exclude contaminants and to determine the number of projectiles impinging on the target. For this purpose, the ionization chamber MUSIC, placed in front of the target, was used to register the projectiles event by event, while recording also their energy loss. This additional information is needed because the incoming ^{208}Pb projectiles may also react in the different layers of matter placed upstream of the liquid-hydrogen target, in particular the plastic scintillator. For those events the lead ions may lose protons or neutrons thus resulting in a cocktail beam reaching the target. Projectiles with atomic numbers different to $Z = 82$ could be identified based on their energy-loss signal measured in the MUSIC chamber in front of the target. Unfortunately, reaction channels in which only neutrons are removed could not be disentangled. However, their nuclear reaction probability in the matter placed before the target was evaluated to be less than 0.5% of the total events, rendering their contribution negligible.

Fig. 2.6 shows the atomic-number histogram deduced from the energy-loss signals registered by the MUSIC chamber. Only the ions with an atomic number inside the window defined by the two vertical lines in Fig. 2.6 are considered as ^{208}Pb projectiles. By fitting the different peaks in the histogram to Gaussian functions one can determine the contribution of each nuclear charge.

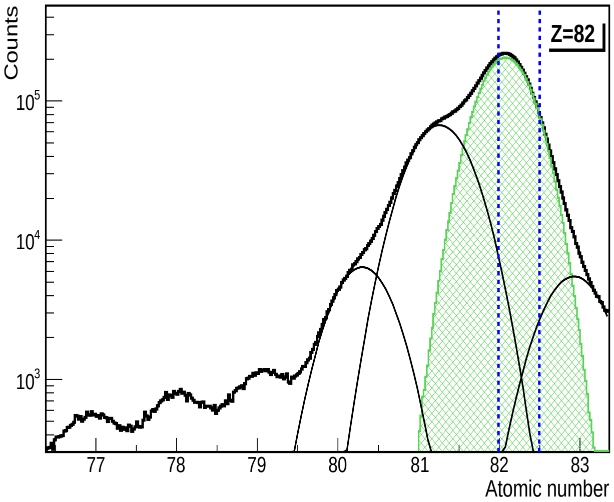

Figure 2.6: *(Color online) Atomic-number histogram of the ions detected with the ionization chamber placed before the target for the reaction* ^{208}*Pb(500A MeV) +* p*.*

As can be seen in the figure, the window contains three nuclear charges leaving the contamination of ions with $Z \neq 82$ to be less than 1.6%, 1.1% for $Z = 81$ and 0.5% for $Z = 83$. $Z = 81$ projectiles are produced in knock-out reactions upstream from the target while $Z = 83$ is attributable to nuclear charge-exchange reactions. Moreover, a TPC chamber, calibrated with a mask, was used to check the impinging position of the projectile ions at the target. Both position distributions are shown in Fig. 2.7. The widths of both distributions are less than 4.5 mm (FWHM). Similar distributions are obtained for the three beam energies used in this work.

Fission fragments can be identified in atomic number using the Twin MUSIC ionization chamber. This detector provides the identification by measuring the energy-loss signals registered by the ten anodes parallel to the common cathode. These anodes provide also the angle and the position of both fission fragments due to their drift time measurements, in the two gas volumes, right and left of the common cathode. Fig. 2.8 shows the two-dimensional spectrum of the energy lost by the fragments (in channels) registered in the two parts of the Twin MUSIC chamber. This spectrum is collected under the condition defined by the window in Fig. 2.6. Fission events are selected by the triangular window indicated in Fig. 2.8. Fragmentation reaction residues and direct beam ions populate the edges of the spectrum. We can also observe beam pileup that is registered in both sides of the chamber and populates the upper right corner of the figure. As can be seen in the figure, fission fragments are well separated from other reaction channels.

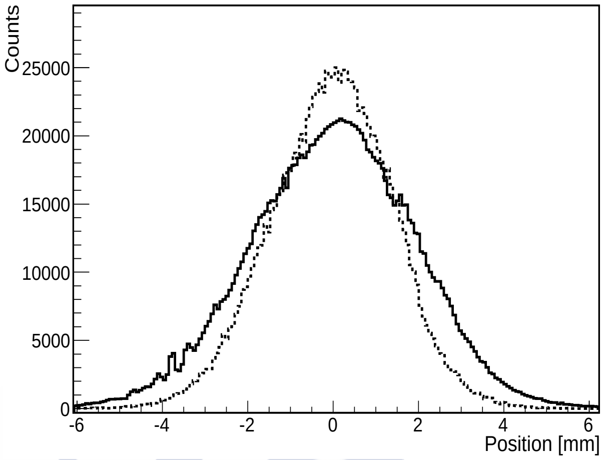

Figure 2.7: *Position distributions of the beam ions in horizontal (solid histogram) and vertical direction (dotted histogram) as determined by the TPC for our measurement at 500A MeV.*

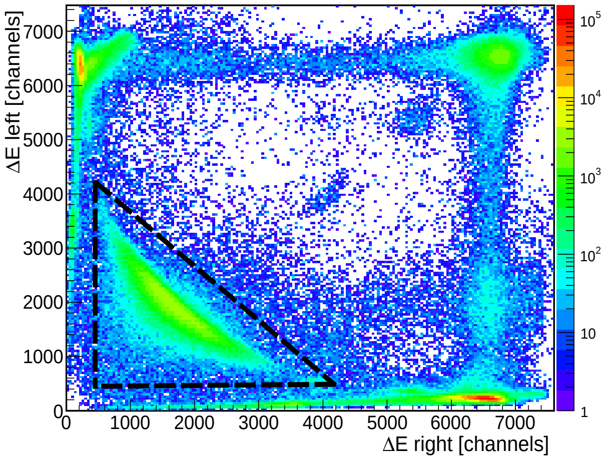

Figure 2.8: *(Color online) Scatter plot of the energy-loss signals register by the two gas volumes of the Twin MUSIC chamber for the reaction* ^{208}*Pb(500A MeV) + p. Fission fragments are located inside the triangular window.*

However, fission events can also be induced in other layers of matter traversed by the beam. Luckily, the contribution to fission of each layer of matter can be tracked back by using the Twin MUSIC, which provides the angle on the plane X-Z and the horizontal position of both fission fragments. The reconstruction is made taking into account that fission fragments follow straight trajectories inside the Twin MUSIC. These trajectories are obtained from linear fits of the drift time signals registered by the ten anodes. The position where fission took place is defined as the intersection point, reaction vertex, between the left and right trajectories. The reconstruction of fission reaction vertex is shown in Fig. 2.9. This spectrum is collected under the conditions defined by the window in Fig. 2.6 and the triangular window in Fig. 2.8. It is clear from the figure that the Twin MUSIC tracking makes it possible to separate between the fission events produced at the target position and fissions originating from other layers of matter, such as the helium gas inside of the pipe or the air between the windows of the target and the helium pipe. However, we can not separate the contribution from the aluminized-mylar windows because these windows have a thickness of 35 μm and their reaction probabilities are negligible. Only events inside the window, defined by the two long-dashed lines in Fig. 2.9, are counted as fission.

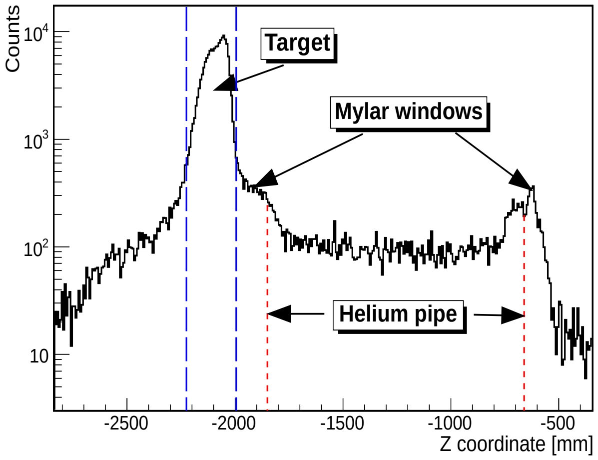

Figure 2.9: *(Color online) Reconstruction of the fission reaction vertex along the Z-coordinate using the tracking capabilities, taking the position of the multi-wire proportional chamber as reference point. The long-dashed lines define the window of fission events taking place inside the hydrogen volume for the reaction* $^{208}Pb(500A\ MeV) + p$.

In Fig. 2.10 we present a cluster plot of the energy loss signals registered by the two sections of the Twin MUSIC taking the conditions indicated in figures 2.6, 2.8 and 2.9 into account. In this figure, we can see a clear identification of fission events.

However, as will be shown in chapter 3, the detection probability of the experimental setup does not fully reach 100% and thus not all fission events are contained inside the window of Fig. 2.9, but this can be easily corrected.

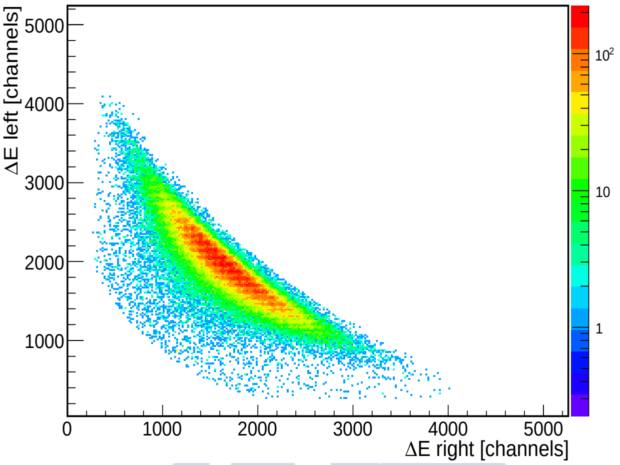

Figure 2.10: *(Color online) Energy loss of the two fission fragments measured independently in the two parts of the Twin MUSIC plotted versus each other under the conditions shown in figures 2.6, 2.8, and 2.9.*

2.3 Isotopic identification of the fission fragments

2.3.1 Atomic-number identification

The atomic number of the fission fragments could be deduced based on the fact that the energy loss is proportional to the atomic number squared. In Fig. 2.11(a) we show the measured atomic-number histogram in the left part of the Twin MUSIC detector (dotted histogram), corrected by the corresponding ToF measurements as shown in Fig. 2.11(b). The final achieved resolution (solid histogram in Fig. 2.11(a)) was better than 0.43 charge units (FWHM). The peaks were then calibrated using a previous measurement of the isotopic distribution of the fission fragments produced in this reaction as a reference [187]. Similar results were obtained for the right part of the detector.

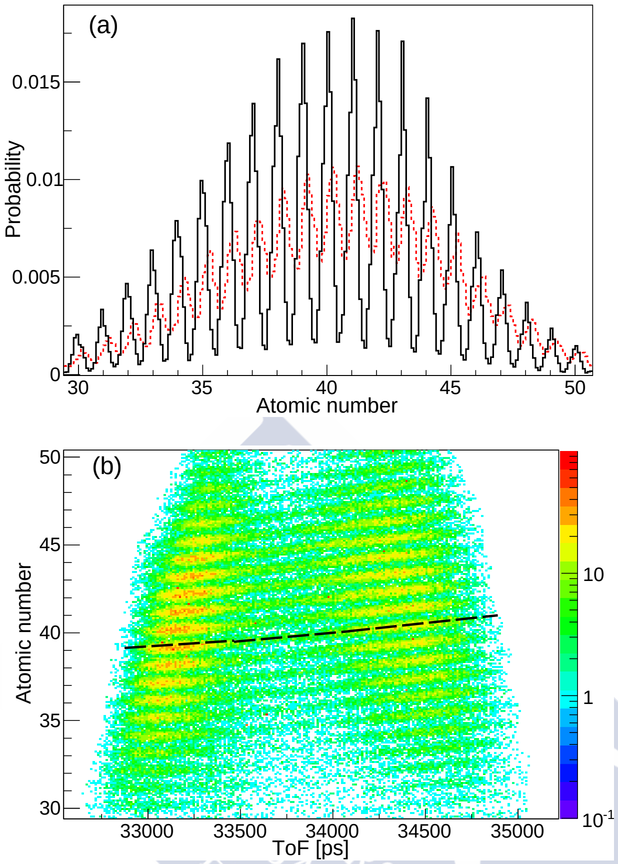

Figure 2.11: *(Color online) (a) Atomic-number histograms of fission fragments detected in the left part of the Twin MUSIC chamber for the reaction* $^{208}Pb(500A$ *MeV) + p. The dotted histogram corresponds to the measured distribution, while the solid histogram represents the same distribution after ToF corrections. (b) Atomic number measured in the left side of the Twin MUSIC detector as a function of the time-of-flight. The dashed line shows an example of the ToF correction needed to improve the resolution of the atomic number.*

The sum of the atomic numbers of the two fission fragments corresponds to the atomic number of the fissioning system ($Z_1 + Z_2$) assuming no proton evaporation after scission. As shown in Ref. [28], the distribution obtained with the sum of the two atomic numbers provides an absolute calibration of the atomic number of the fissioning system. Taking this fact into account, in Fig. 2.12 we show a scatter plot of the atomic numbers registered in both sides of the Twin MUSIC chamber after ToF corrections and based on independent calibrations. As can be seen in the figure, the dashed line corresponds to the atomic number $Z_1 + Z_2 = 83$, which is produced by single charge-exchange processes between projectile and target nuclei [188, 189]. Beyond the dashed line one can also observe spots due to the production of double charge-exchange reactions. These results are in agreement with previous measurements [28].

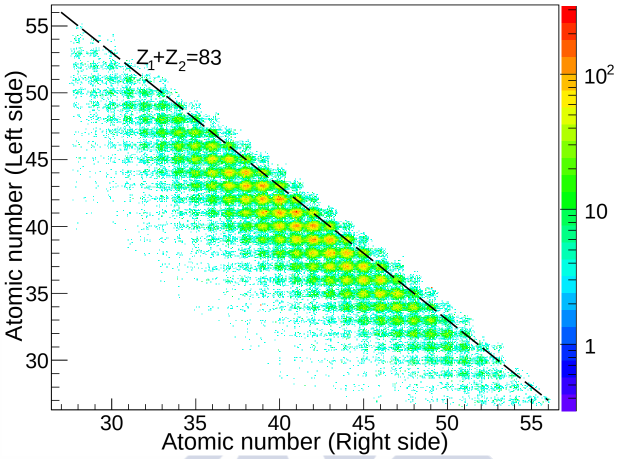

Figure 2.12: *(Color online) Atomic numbers registered in coincidence by the Twin MUSIC in the reaction ^{208}Pb(500A MeV) + p. The dashed line represents the fissioning systems with atomic number $Z_1 + Z_2 = 83$.*

2.3.2 Mass-number identification

The horizontal positions obtained from the MWPCs and the angles from the Twin MUSIC chamber give access to the curvatures of the trajectories of the fragments inside the dipole magnet ALADIN, providing their magnetic rigidity by taking into account the value of the magnetic field (1.6 T). The entrance angles on the plane X-Z were obtained from linear fits of the positions recorded by the ten anodes of the Twin MUSIC chamber. In Fig. 2.13 we present the position resolution (FWHM) of the anodes, obtained as the difference between the linear fit and the positions registered by the corresponding anode, as a function of the atomic number of the fission fragments. The position at each anode was obtained by using its drift-time signal and the velocity of the electrons in the gas. The resolution is shown for the left (solid squares) and right (solid circles) side. As can be seen in the figure, the resolution depends on the atomic number, as expected because the deposited energy in the anodes increases with the atomic number of the fission fragments. Therefore, the signal-to-noise ratio increases with the atomic number, improving the position resolution. In the figure, one can observe that both sections of the Twin MUSIC chamber have similar position resolutions, evolving from 85 μm to 35 μm with the atomic number. These resolutions correspond to angular resolutions between 0.4 mrad and 0.1 mrad, respectively.

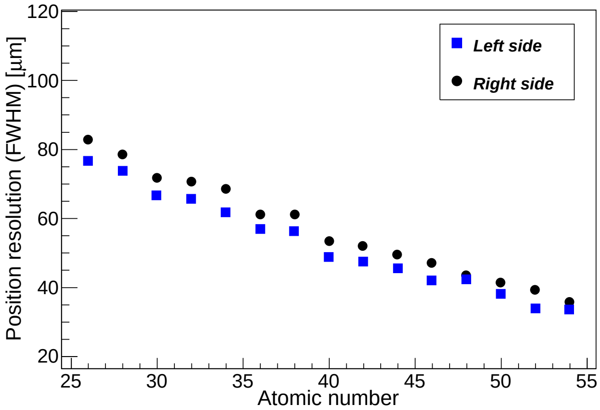

Figure 2.13: *(Color online) Mean position resolution provided by the Twin MUSIC for the anodes used in the tracking as a function of the atomic number of the fission fragments.*

Full identification of the fission fragments is made using a ray-tracing method [190] coupled to GEANT4 simulations [191, 192, 193] to reconstruct their mass numbers. In the simulation, we took into account the composition, dimensions, and positions of the detectors, as well as the magnetic field and helium gas inside the dipole magnet ALADIN. Outside of the magnet we assume that fission fragments follow straight-line trajectories.

The reconstruction of the trajectories is performed using the measured atomic numbers, positions and angles of the fission fragments before the dipole magnet ALADIN, as well as the positions on the target given by the TPC and tracking capabilities of the setup as an input for the simulation. First, different trajectories are simulated for each fission fragment covering the expected range of $B\rho$, between 6−10 Tm. The simulated trajectories are then used to parametrize the experimental $B\rho$ and flight path length of each fission fragment as a function of the position of the MWPC situated behind the dipole magnet, as shown in Figs. 2.14(b) and 2.14(c) respectively. Then, these parametrizations together with the experimental position recorded by the MWPC are used to obtain the experimental flight path length and $B\rho$ of each fission fragment. Finally, the measured ToF together with the reconstructed flight path length are used to deduce the velocity of the fragments with a resolution of $\Delta v/v \sim 0.11\%$ (FWHM).

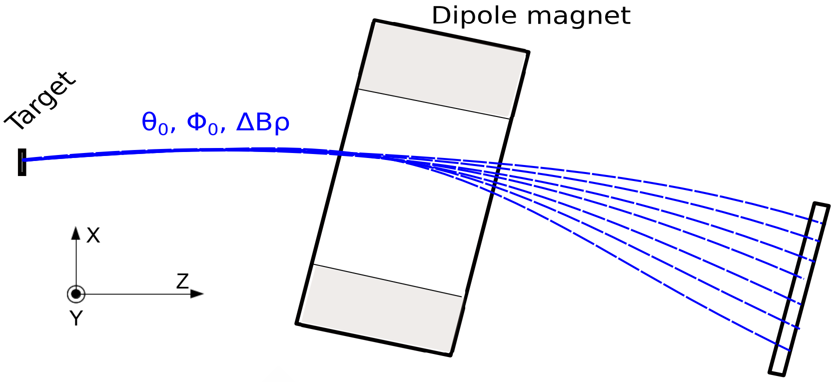

(a) Picture in the plane X-Z of our method applied to reconstruct trajectories inside the magnet. Different trajectories are simulated for the measured polar (θ_0) and azimuthal (Φ_0) angles at the entrance of the magnet.

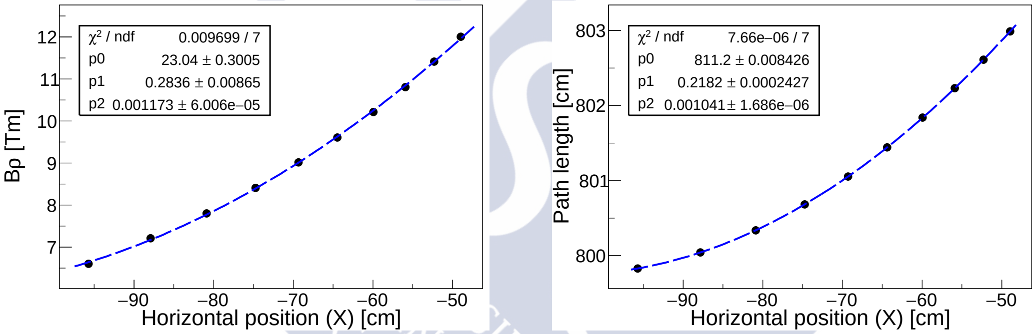

(b) Correlation between the Bρ and the horizontal position on the detectors placed behind the magnet.

(c) Correlation between the flight path length and the horizontal position on the detectors placed behind the magnet.

Figure 2.14: *(Color online) Bρ and flight path length correlations found with the reconstruction method.*

Consequently, the mass number (A) is obtained for each fission fragment from its magnetic rigidity, velocity and atomic number, according to the equation:

$$A = \frac{eZ}{u}\frac{B\rho}{\beta\gamma c} \tag{2.1}$$

where Z is the atomic number provided by the Twin MUSIC detector (see Fig. 2.11(a)), B is the magnetic field inside the magnet, ρ is the radius of the trajectory, u is the atomic mass unit, e is the electron charge, $\gamma = 1/\sqrt{1-v^2/c^2}$, v is the velocity of the ion and c is the velocity of light.

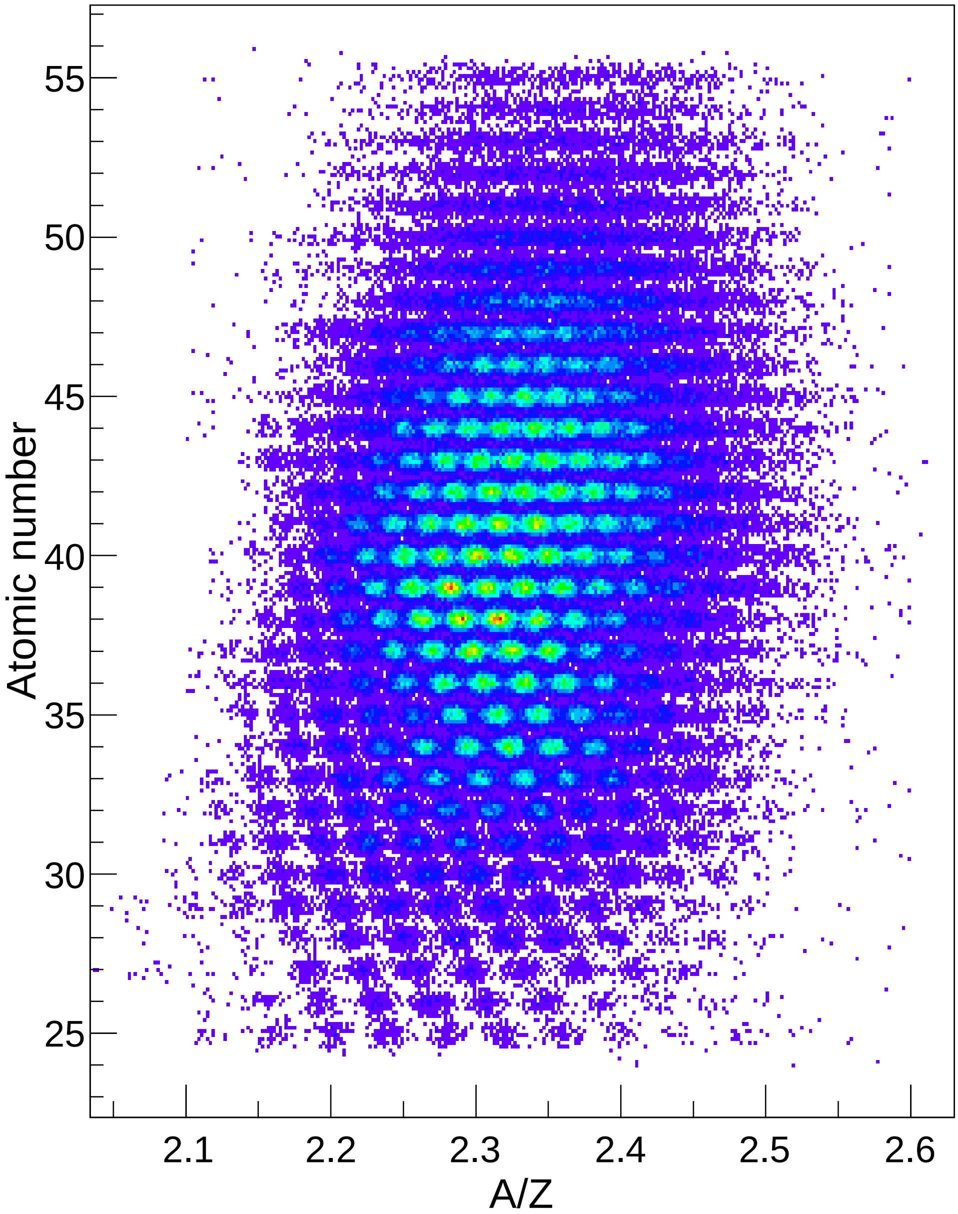

Figure 2.15: *(Color online) Cluster plot of the detected fission fragments displaying the correlations between the atomic number, obtained from energy-loss measurements in the Twin MUSIC detector, and the mass-over-charge ratio (A/Z) determined from magnetic rigidity and time-of-flight measurements. This plot provides a full and unambiguous identification in mass and atomic number of all fission fragments produced in the reaction* $^{208}Pb(500A\ MeV) + p$.

Using this procedure, the mass number of each fission fragment is obtained. The absolute calibration in mass number was obtained using previous measurements [187] as reference. Figure 2.15 shows a scatter plot of the atomic number as a function of the mass-over-charge ratio (A/Z) obtained in this experiment. As can be seen in the figure, a clear identification of fission fragments is achieved with an average resolution of $\Delta A/A \sim 0.63\%$ (FWHM).


USC
UNIVERSIDADE
DE SANTIAGO
DE COMPOSTELA

Chapter 3

Presaddle fission dynamics

As discussed in section 1.2, different experimental observables have been proposed in previous works to investigate the dynamics of the fission process at small deformations, such as the total and partial fission cross sections, width of the charge distribution of the fission fragments and emission of particles. However, all these observables were measured separately using different techniques. Therefore, in this chapter we investigate the ground-to-saddle dynamics of the fission process revisiting many of these observables but using a experimental setup that allowed us to measure all of them in the same experiment.

Moreover, we use optimal experimental conditions for the investigation of the fission dynamics by investigating the fission of almost spherical nuclei at high excitation energies and low angular momentum produced in collisions of ^{208}Pb projectiles accelerated at relativistic energies. Fortunately, these conditions also represent a good approach to study the effect of the level densities on the experimental observables, such as the fission cross sections, partial fission cross sections and width of the atomic-number distribution of the fission fragments, because the effect of the rotational and vibrational excitations on the level densities washes out at excitation energies around 40 MeV [108, 147].

In this work the reactions ^{208}Pb(370A, 500A, and 650A MeV) + p and ^{208}Pb(500A MeV) + ^{27}Al were selected to investigate the evolution with the energy and entrance channel of different observables characterized to be sensitive to the presaddle fission dynamics, such as the total and partial fission cross sections [27, 28, 135, 194], the width of the charge distribution of the fission fragments (investigated by Jurado et al. [27], Ayyad et al. [28], and Schmitt et al. [137]), and the emission of light-charged particles [6]. In sections 3.1, 3.2, and 3.3 we will analyse and discuss these observables. Finally, in section 3.4 the total fission cross sections, width of the charge distribution of the fission fragments and emission of light-charged particles will be compared with different model calculations to extract information on dissipative effects at small deformation in fission. Moreover, the total and partial fission cross sections and the width of the charge distribution will be used to investigate the level densities, in particular the level-density parameter.

3.1 Total fission cross sections

The complete inventory of residual fragments produced in spallation reactions induced by protons on lead at 500 and 1000 A MeV has been already determined [21, 187]. These measurements were performed in inverse kinematics by employing a high-resolving power magnetic spectrometer. Despite the accuracy of the spectrometer, which was sufficient to identify the reaction products in terms of their mass and atomic number, the measurement of fission residues was affected by the limited angular and momentum acceptance [19]. This could explain the unexpected high fission cross section obtained at 500A MeV (232 mb) [187]. Indeed, a later measurement of this cross section performed by Schmidt and collaborators [195], based also on the inverse kinematics technique but detecting both fission fragments in coincidence, provided a lower fission cross section (146 mb).

Proton induced fission cross sections on lead have also been measured in direct kinematics experiments covering a large range in energy [12]. In this case limitations associated with the absorption of the fragments in the target and the techniques used for the identification of the fission channel, could also explain the discrepancies, up to 50%, observed in these measurements. Therefore, the systematic of the proton on lead fission cross section established by Prokofiev some time ago [12] could be questioned.

To clarify these discrepancies, in this work the total fission cross sections of the reactions ^{208}Pb+ p at 370A, 500A, and 650A MeV and ^{208}Pb + ^{27}Al 500A MeV were measured with high precision. The SIS18 synchrotron was used to accelerate ions of ^{208}Pb up to kinematic energies of 650A MeV with an intensity around 10^5 ions/s. The primary beam was then guided to the experimental setup where fission reactions were induced in different targets. A cylindrical target filled with liquid-hydrogen ($\sim$ 85 mg/cm^2) was used to investigate spallation-induced fission, while fragmentation-induced fission was investigated using an aluminium target ($\sim$ 1080 mg/cm^2).

The use of the inverse kinematics technique allowed us to separate fission from other reaction channels and also facilitates the identification of both fission fragments (see section 2.2). Fission events were identified using energy-loss measurements performed with a double multisampling ionization chamber (Twin MUSIC). In addition, the tracking capabilities of this detector permitted us to select fissions produced at the target position (see section 2.2).

The number of projectiles (N_p) was determined by using a multisampling ionization chamber (MUSIC) (see section 2.2) while the number of fission events (N_f) was obtained from a double multisampling ionization chamber (Twin MUSIC) whose tracking capabilities permitted us to count fissions produced at the target position (see Fig. 2.9). Their statistical uncertainties are given by Poisson statistics according to the observed number of counts, and for the three measurements they were below 1%.

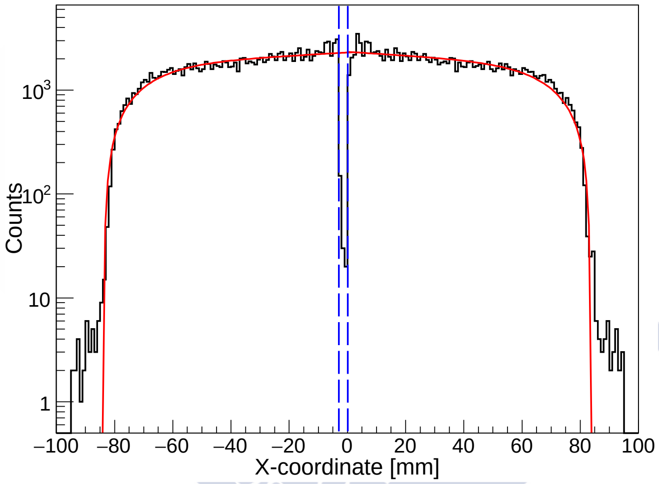

Figure 3.1: *(Color online) Horizontal (x-coordinate) position of the fission fragments recorded by the MWPC chamber for the reaction ^{208}Pb (500A MeV) + p. The two dashed vertical lines indicate the shadow due to the cathode in the center of the Twin MUSIC chamber. The full line is the result of a fit to the histogram.*

An important factor to obtain an accurate value of the cross sections is to determine the efficiency of the experimental setup. The main contributions to the detection efficiency are the finite transversal size of the primary beam and its alignment with respect to the cathode placed in the middle of the Twin MUSIC chamber. Fission fragments emitted close to the vertical plane may hit the cathode or pass through the same part of the Twin MUSIC chamber and without being registered as fission events. Moreover, fission fragments with a very large angular aperture could hit the aluminium pipe placed in front of the Twin MUSIC chamber reducing thereby the fission detection efficiency. To evaluate the losses on the cathode of the Twin MUSIC we use the MWPC chamber, which allows us to evaluate the shadow induced by the cathode plane. Fig. 3.1 shows the horizontal position of the fission fragments recorded by the MWPC chamber. This spectrum is collected under the condition defined by the window in Fig. 2.9, i.e., fission events induced by the hydrogen target. In the figure, the shadow due to the cathode is indicated with two vertical lines. The full line shows the result of fitting the distribution with a function defined as the sum of a fourth-order polynomial and a Gaussian. The loss of fission events is estimated based on the difference between the fit and the measured spectrum, obtaining a value around 4.5% for the reaction ^{208}Pb (500A MeV) + p.

Fission events lost because both fragments passed through the same part of the Twin MUSIC chamber, are estimated by using a simulation. In this simulation, based on the GEANT4 code [191, 192, 193], fission events were generated with the reaction models INCL4.6 [159] and ABLA07 [160] and then propagated through the experimental setup taking electromagnetic and nuclear interactions in all layers of matter into account. Fission fragments originating from fissions in the target were simulated based on the target thickness (11.24 mm) and the beam profile (4 mm FWHM).

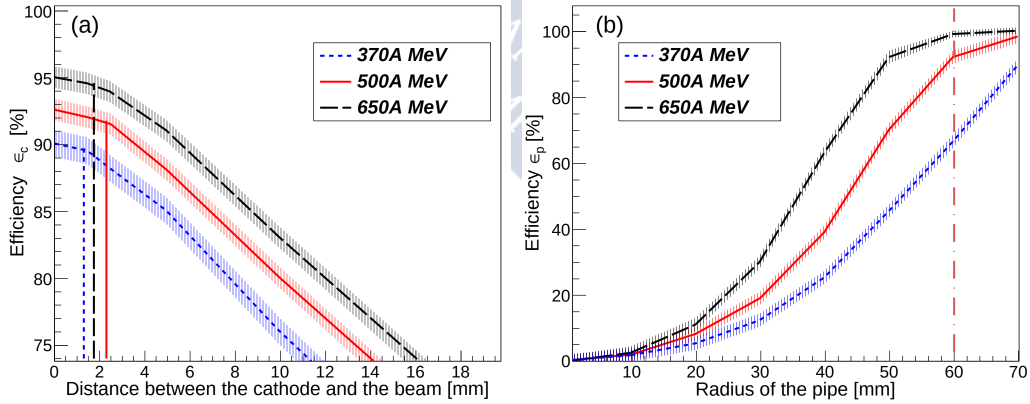

Figure 3.2: *(Color online) (a) Simulated efficiency for the detection of both fission fragments in the same section of the Twin MUSIC detector as a function of the misalignment distance between the beam and the central cathode of the detector for the three energies investigated in this work. The vertical lines represent the mean value of the measured misalignment for each energy. (b) Simulated geometrical efficiency due to the finite size of the helium pipe located between the target and the Twin MUSIC detector. The vertical line represents the pipe radius.*

Table 3.1: *Fission reaction with its corresponding corrections due to Twin MUSIC efficiency, fission events lost on the helium pipe, beam attenuation in the target and secondary reactions of the beam.*

Reaction	Twin MUSIC efficiency $\varepsilon_{TwinMUSIC}$ [%]	Pipe correction ε_p [%]	Beam attenuation f_{beam} [%]	Secondary reactions f_{sr} [%]
^{208}Pb(370A MeV) + p	86 ± 2	66 ± 2	3.6 ± 2	2.0 ± 1
^{208}Pb(500A MeV) + p	88 ± 2	94 ± 2	3.8 ± 2	2.1 ± 1
^{208}Pb(650A MeV) + p	87 ± 2	99 ± 1	4.0 ± 2	2.2 ± 1
^{208}Pb(500A MeV) + ^{27}Al	88 ± 2	100 ± 1	4.0 ± 2	2.2 ± 1

This simulation provides the probability that both fission fragments pass through the same part of the Twin MUSIC chamber, which depends on the misalignment between the cathode and the horizontal position of the beam ions. The results of the simulation are shown in Fig. 3.2(a). This figure represents the average efficiency (lines) with its associated uncertainty (dashed area) as a function of the distance between the beam and the cathode of the Twin MUSIC for the three energies used in the experiment. The vertical lines represent the mean position of the beam ions for each energy obtained with the MWPC detector placed behind of the Twin MUSIC. One can see that, as expected, the efficiency decreases with the misalignment between the beam ions and the cathode of the Twin MUSIC detector and increases with the energy of the beam.

The simulation is also used to obtain the efficiency loss due to the limited size of the aluminium pipe placed in front of the Twin MUSIC chamber. In this case, the efficiency depends on the radius of the pipe and the energy of the beam. The results of the simulation are shown in Fig. 3.2(b) with their associated uncertainty.

As can be seen in Table 3.1, all applied corrections are rather small, the largest being those corresponding to the attenuation of the beam intensity in the target, the lost fission events in the helium pipe and the detection efficiency of the Twin MUSIC chamber. The correction of the beam attenuation in the target is obtained from the reaction probability of the incoming projectiles in half of the target thickness calculated with the code INCL4.6 [159]. The obtained corrections for the three energies, 370A, 500A, and 650A MeV, were 3.6%, 3.8% and 4.0%, respectively. This correction for the reaction ^{208}Pb(500A MeV) + ^{27}Al was obtained using the reaction probability calculated with the code Karol [196], obtaining a correction factor of 4.0%. Secondary reactions of the beam ions in the target are also evaluated based on the nuclear reaction rate in half of the target thickness. The obtained corrections are below 2.2% for all the cases. Moreover, the fission fragments could also undergo secondary reactions between the target and the Twin MUSIC chamber and not be counted as fission events. The corresponding probability for the different layers of matter is below 0.4% for the three experimental energies. The systematic uncertainties associated to these corrections are also listed in Table 3.1. A background correction (f_{br}) from the reconstruction of the fission reaction vertex along the Z coordinate (see Fig. 2.9) was also taken into account. This correction was estimated to be below $(2.1 \pm 1)\%$ for all the investigated reactions.

Table 3.2: *Measured fission yields ($n_f = N_f/N_p$) for each reaction. The total fission yield n_f^{tot} represents corrected fission yield, n_f^{tot} = $[n_f \cdot (1\text{-}f_{sr}) \cdot (1\text{-}f_{br})]/[\varepsilon_{TwinMUSIC} \cdot \varepsilon_p \cdot (1\text{-}f_{beam})]$. The fission cross section is given by $\sigma = -ln(1\text{-}n_f^{tot})/N_t$, where N_t represents the number of nuclei in the target per unit area.*

Reaction	Fission yield n_f	Total fission yield n_f^{tot}	Total fission cross section [mb]
^{208}Pb(370A MeV) + p	0.00359	0.00629 ± 0.00031	123 ± 7
^{208}Pb(500A MeV) + p	0.00630	0.00762 ± 0.00031	149 ± 8
^{208}Pb(650A MeV) + p	0.00716	0.00838 ± 0.00030	164 ± 8
^{208}Pb(500A MeV) + ^{27}Al	0.00493	0.00558 ± 0.00031	233 ± 15

The results obtained for the total fission cross section are listed in Table 3.2 and displayed in Fig. 3.3 (solid circles) as function of the kinetic energy of the proton and compared to previous measurements reported in literature for the reactions p + ^{nat}Pb and ^{208}Pb + p. Fission cross sections of ^{nat}Pb(p,f) are expected to be above the ones of ^{208}Pb(p,f) because of the lower fission barriers of the naturally abundant lead, with more proton-rich isotopes. The expected difference between the fission cross sections of ^{208}Pb(p,f) and ^{nat}Pb(p,f) is less than 10% [197].

As can be seen in the figure, our data have in general better accuracy than any of the previous ones. Moreover, our measurement at 500 MeV is in perfect agreement with the recent measurement of Schmidt and collaborators (solid triangle up) [195] using a similar experimental technique. However, the cross section obtained by Fernández and collaborators (solid square) [187] using the magnetic spectrometer FRS at GSI exhibits an important deviation with respect to our results and the general systematics. This deviation could be due to the limited acceptance of the spectrometer used in that work [19].

The present results are consistent with the measurements using proton induced fission on ^{208}Pb between 50 and 200 MeV obtained by Flerov (diagonal crosses) [198], Shigaev (crosses) [199] and Duijvestijn (open star) [200]. The same occurs when one compares our data with the measurements of ^{nat}Pb between 50 and 200 MeV, which were performed by Shigaev (open triangles up) [199], Duijvestijn (open triangle down) [200] and Bychenkov (open squares) [201], as well as with the values reported by Konshin (stars) [202] between 150 and 400 MeV. Moreover, the results obtained by Enqvist and collaborators (open circle) [21] with ^{208}Pb at 1000 MeV using the magnetic spectrometer FRS, also seems consistent with the extrapolation of our data. One can observe that the cross section obtained by Gloris (open diamond) [203] with ^{nat}Pb at 1000 MeV is consistent with the previous measurement of Enqvist and collaborators (open circle) because, as already mentioned, the measurements performed with ^{nat}Pb must be above those with ^{208}Pb.

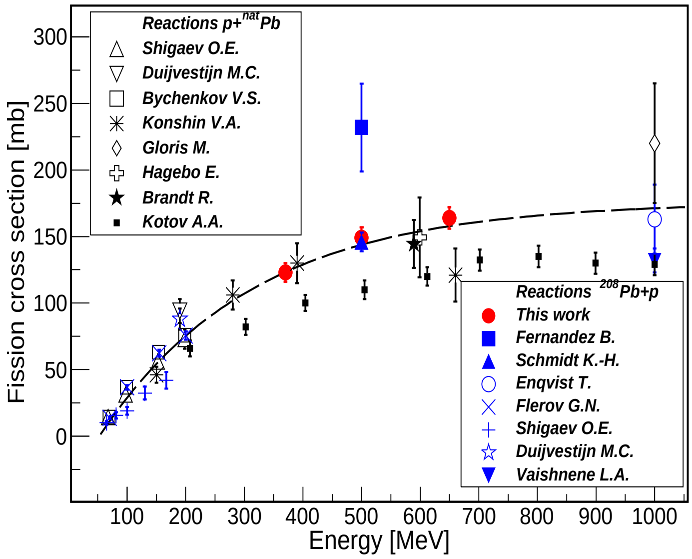

Figure 3.3: *(Color online) Total fission cross sections measured in the present work (solid circles) as a function of the proton energy in comparison to previously measured data for the reactions p +* ^{nat}*Pb and* ^{208}*Pb + p. The dashed line is a guide to the eye.*

Our measurements are also in agreement with the values reported by Hagebø (open cross) [204] and Brandt (solid star) [205], who measured in direct kinematics the reaction $p + {}^{nat}$Pb at 600 and 590 MeV, respectively. Finally, the results reported by Kotov (small solid squares) [206] measuring proton-induced fission on ^{nat}Pb covering a large range of kinetic energies show a systematic underestimation of the cross sections compared to the other measurements. However, the relative evolution of Kotov's data with the proton energy confirms the tendency shown by our data between 300 and 700 MeV and the extrapolation up to 1000 MeV. One can also observe that the measurement reported by Vaishnene (solid triangle down) [207] at 1000 MeV presents the same underestimation.

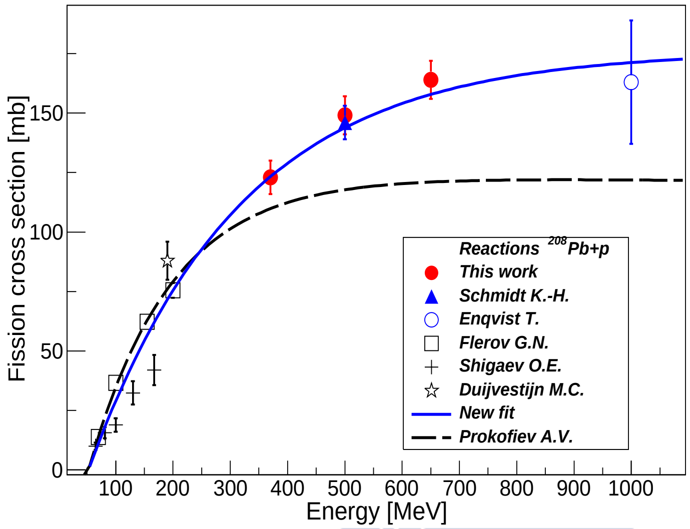

Figure 3.4: *(Color online) Comparison between Prokofiev's systematics for proton-induced fission on* ^{208}*Pb (dashed line) and different measurements (symbols). The solid line represents a fit of the new data using Prokofiev's equation.*

The new measurements together with the validated data for other energies were used to benchmark the parametrization of total fission cross sections for proton-induced reactions on ^{208}Pb performed by Prokofiev [12]. The parametrization shown in Eq. 3.1, was first proposed by Fukahori and Pearlstein [208] and later modified by Prokofiev to take into account the reduction of the fission cross sections at energies above 1000 MeV.

$$\sigma_f(E) = P_1(1 - e^{-P_3(E-P_2)})(1 - P_4 ln(E)) \tag{3.1}$$

Fig. 3.4 shows the measurements obtained in this work (solid circles) together with the data reported by Schmidt (solid triangle up) [195], Enqvist (open circle) [21], Flerov (open squares) [198], Shigaev (crosses) [199] and Duijvestijn (open star) [200] in comparison to the systematics proposed by Prokofiev [12] for ^{208}Pb(p,f) reactions (dashed line). Clearly the systematics of Prokofiev underestimates the data for energies larger than 300 MeV while at low energies the systematic seems to reproduce the data fairly well. This is an expected result because the systematics were obtained by fitting the low-energy measurements and the one at 1000 MeV reported by Vaishnene and collaborators [207]. However, we have only taken into account the measurement of Enqvist and collaborators [21] because it is in better agreement with the tendency of our data.

In order to obtain a better parametrization of the proton on lead total fission cross sections, we have repeated the fit using the data shown in Fig. 3.4. In this fit we have fixed the parameter P_4 to the same value given by Prokofiev to avoid divergences because of the limited number of measurements above 700 MeV. The new values of the parameters are shown in Table 3.3 and are compared with the previous ones obtained by Prokofiev. The result of this new fit is also shown in Fig. 3.4 as solid line.

Table 3.3: *Parameters of the parametrization of the total fission cross sections for the reaction p +* ^{208}*Pb obtained in this work and the ones previously proposed by Prokofiev.*

P_1	P_2	P_3	P_4	χ^2/ν	Reference
179	52.8	0.00378	0.00203	6.76	This work
142	52.7	0.00665	0.00203	1.26	Prokofiev [12]

3.2 Partial fission cross sections and width of the charge distribution

Several works have shown that the investigation of other observables, such as partial fission cross sections and widths of the atomic-number distributions of the final fission fragments, as a function of the sum of the atomic number of the two fission fragments also provide relevant information on the evolution of the fission process, in particular, on the ground-to-saddle dynamics [27, 28, 134, 137]. In this section, we investigate how these two observables evolve with the violence of the reaction changing the target mass and the bombarding energy of the projectile.

The partial fission cross sections were obtained normalizing the yields of the fissioning system, calculated according to the sum of the atomic numbers of the two fission fragments measured with the double multisampling ionization chamber Twin MUSIC (see section 2.2), to the total fission cross section measured in the present work (see Table 3.2). The sum of the atomic numbers of the two fission fragments ($Z_1 + Z_2$) corresponds to the atomic number of the fissioning system, assuming no proton evaporation beyond the saddle point. This assumption is justified because the fission fragments are neutron-rich [187] and they mainly deexcite by neutron emission. This observable shows a strong correlation with the impact parameter and then with the excitation energy gained by the fissioning system at saddle [27, 28]. Therefore, it is considered a good tool to constrain model calculations for fissioning systems with different fissilities and excitation energies.

On the other hand, the width of the atomic-number distribution of the fission fragments is strongly correlated with the excitation energy of the compound nuclei along the fission path, and from a statistical interpretation this observable should be proportional to the temperature at the saddle point [27, 134, 137] (see section 1.2.3). The investigation of this observable as a function of the atomic number of the fissioning system ($Z_1 + Z_2$) allowed to study its evolution with the excitation energy, because fissions of the heavier fissioning systems close to the projectile are produced in peripheral reactions with low excitation energies, while the lighter fissioning systems are attributed to central collisions where the compound nuclei are produced with high excitation energies. According to the statistical model [145], the width of the atomic-number distribution of the fission fragments can be parametrized as a function of the temperature at the saddle point T_{sd} (see equation 1.4). T_{sd} is related to the excitation energy at saddle (E^*_{sd}) as $T_{sd} = \sqrt{E^*_{sd}/a_{sd}}$, where a_{sd} is the level-density parameter at the saddle point. Therefore, the width of the atomic-number distribution represents a good tool to investigate dissipative effects in fission and the description of the level-density parameter at the saddle-point deformation, providing an important constraint for model calculations.

In Fig. 3.5 we compare the partial fission cross sections of the reactions measured in this work: ^{208}Pb + p at 370A (open crosses), 500A (open circles), and 650A MeV (open diamond), and ^{208}Pb + ^{27}Al at 500A MeV (open triangles). Our measurements are also compared to previous ones performed by Ayyad and collaborators for the reaction ^{208}Pb + d at 500A MeV (open squares) [28].

The maximum value for the partial fission cross sections is always found close to the projectile atomic number ($Z_1 + Z_2 = 82$). The cross sections decrease with decreasing $Z_1 + Z_2$ because for the lighter fissioning systems the fission barriers become higher and also because smaller impact parameters are less likely [209]. The partial fission cross sections of the lightest fissioning systems are expected to increase with the violence of the reaction (either projectile kinetic energy or mass number of the target nuclei) because more nucleons are removed from the projectile. This fact is clearly observed in Fig. 3.5.

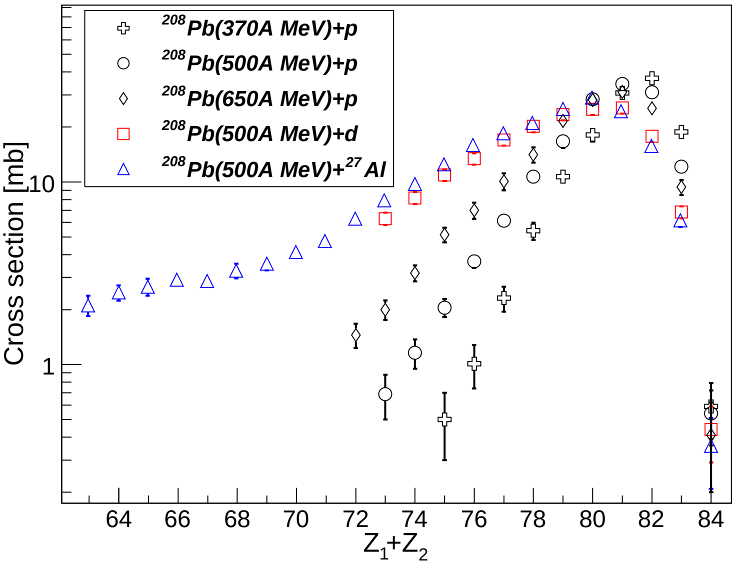

__Figure 3.5:__ (Color online) Partial fission cross sections as a function of the atomic number of the fissioning system ($Z_1 + Z_2$) for the reactions measured in this work. The measurement of ^{208}Pb + d at 500A MeV performed by Ayyad et al. [28] is also displayed.

In the same figure, one can see that fission from single and double charge-exchange reactions $Z_1 + Z_2 = 83$ and $Z_1 + Z_2 = 84$, respectively, were also measured in the present experiment. These charge-exchange reactions are expected to be peripheral reactions that can occur by the exchange of a virtual pion between the colliding nucleons (quasielastic charge exchange) or the excitation of a nucleon resonance decaying by pion emission (inelastic charge exchange). Therefore, the probability of these channels depends on the absorption of the pion and on the probability of proton emission, either in the intranuclear cascade or in the deexcitation stage. As can be seen in the figure, the probabilities of these channels seem to decrease with the energy of the reaction. These results are consistent with charge-pickup reactions investigated with a beam of ^{208}Pb impinging on proton and deuterium targets at 1A GeV [188]. On the other hand, for the reactions ^{208}Pb + d at 500A MeV (open squares) and ^{208}Pb + ^{27}Al at 500A MeV (open triangles) the partial fission cross sections seem to be very similar for fissioning systems below $Z_1 + Z_2 = 81$. However, one can see that the reaction ^{208}Pb + ^{27}Al at 500A MeV covers a larger range in fissioning systems, indicating that the abrasion process is more violent.

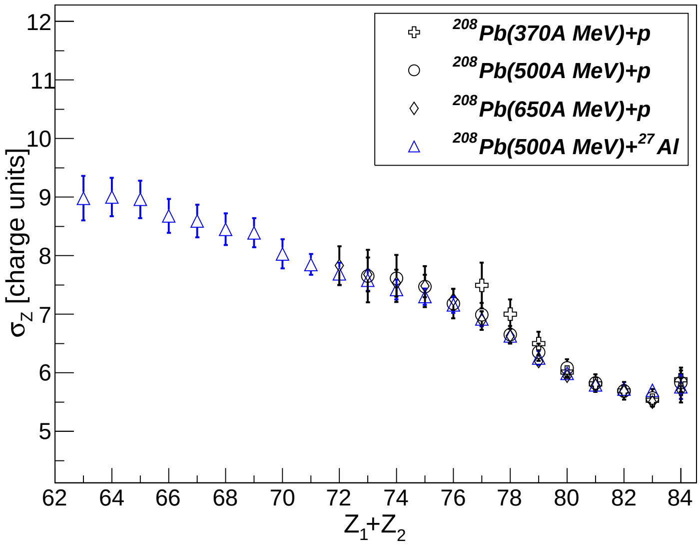

Figure 3.6: *(Color online) Width of the atomic-number distribution of the final fission fragments measured in spallation and fragmentation reactions of* ^{208}*Pb as a function of the atomic number of the fissioning nuclei for different entrance channels and projectile energies.*

In Fig. 3.6 we display the width of the atomic-number distribution of the fission fragments as a function of the atomic number of the fissioning system (Z_1+Z_2) for the different reactions measured in this work: ^{208}Pb + p at 370A (open crosses), 500A (open circles), and 650A MeV (open diamond), and ^{208}Pb + ^{27}Al at 500A MeV (open triangles). As can be seen, the width of the atomic-number distributions increases when decreasing $Z_1 + Z_2$ as expected from Eq. 1.4 if one considers that lighter fissioning systems reach the saddle point with higher temperatures. Moreover, for all the reactions very similar values of the width for each $Z_1 + Z_2$ are obtained. This result indicates that the width of the atomic-number distribution of the fission fragments depends on neither the entrance channel nor on the bombarding energy of the projectile, supporting then its statistical interpretation and its corelation with the temperature of the fissioning systems at saddle [27, 134, 137] (see section 1.2.3). We can then conclude that this observable characterizes the compound fissioning nuclei despite of the used reaction.

On the other hand, the range in $Z_1 + Z_2$ covered in each reaction is different because it reflects the initial violence of the reaction, and consequently the evaporation effects due to the increase of excitation energy. The same conclusions were also pointed out in a recent work performed by Ayyad and collaborators [28] using proton- and deuteron-induced fission of ^{208}Pb. Therefore, this observable clearly provides an important constraint for model calculations describing the evolution of the fissioning system from the ground-state to the saddle-point configuration.

3.3 Light-charged particles

The investigation of the light-charged particles ($Z = 1$, 2 and 3) emitted in fission events is also a good tool to study the ground-to-saddle dynamics of the fission process. In the reactions investigated in this work, spallation and fragmentation induced fission, the light-charged particles can be emitted from the first stage of the reaction or through the deexcitation of the compound nucleus. The measurement of these particles in coincide with fission is a difficult task in direct kinematics due to the usual problems to detect the fragments (see chapter 2). For this reason, our novel setup together with the inverse kinematics technique represent an ideal scenario because all the particles leave the target with high kinetic energies in the forward direction facilitating their detection with high efficiency and precision.

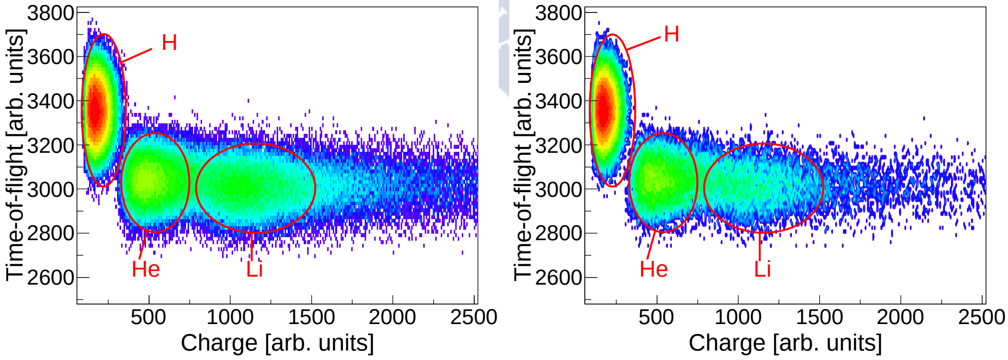

Figure 3.7: *(Color online) Identification of particles in the scintillators of the ToF wall for light-charged particles. The solid elipses indicate the selection of particles. (a) No fission. (b) Fission.*

Because of the reaction kinematics, while most of the fission fragments go through the Twin MUSIC, large fractions of the light-charged particles escape the target to reach the plastic scintillators of the ToF Wall (see chapter 2). The time and charge of the scintillator signals were registered using a TDC and a QDC, respectively. Figs. 3.7(a) and 3.7(b) show a scatter plot of the time-of-flight of the detected light-charged particles as a function of their energy loss deposited in the plastic scintillators, for trigger no fission and fission respectively. These figures show the identified particles from $Z = 1$ to $Z = 3$.

Figure 3.8 shows the light-charged particles detection efficiency factor as a function of the multiplicity of light-charged particles with $Z = 1$ together with its associated uncertainties (dashed area). These correction factors were estimated with GEANT4 simulations [191, 192, 193] by using INCL4.6 [159]+ABLA07 [160] as event generator. Using these models, we estimated that the major part of the particles emitted come from the cascade process ($\sim$ 75%) being detected with a geometrical efficiency around 30%, while the particles emitted in the deexcitation process could be detected with a geometrical efficiency around 80%.

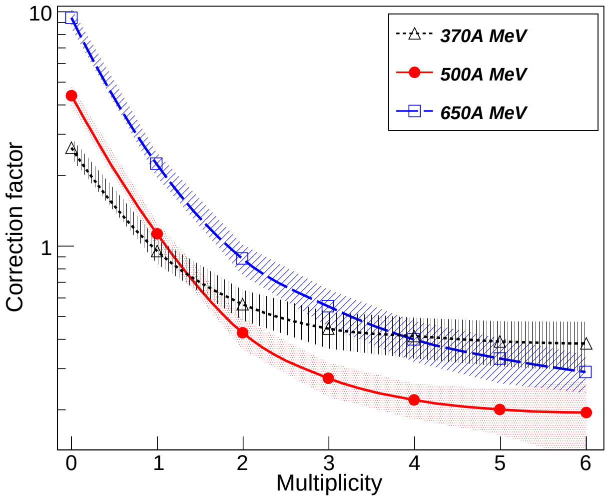

Figure 3.8: *(Color online) Total efficiency correction factor for light-charged particles with $Z = 1$ as a function of the multiplicity. These correction factors are calculated for the three kinetic energies investigated in this work.*

In the GEANT4 simulations [192], we took into account the dimensions and positions of the ToF Wall as well as the intrinsic efficiency for each particle. For light-charged particles with $Z > 1$ the intrinsic efficiency was assumed to be around 100% and for particles with $Z = 1$ the intrinsic efficiency was estimated to be: 85%, 80%, and 75% for the projectile kinetic energies of 370A, 500A and 650A MeV, respectively. For the latter case the intrinsic efficiency was determined using the total efficiency ϵ_{total} and the geometrical efficiency ϵ_{geo} as $\epsilon_{int} = \epsilon_{total}/\epsilon_{geo}$. The total efficiency was obtained by counting the detected particles with respect to the emitted ones from the fissioning system under the condition $Z_1 + Z_2 = 81$, where one light-charged particle with $Z = 1$ is always emitted in the forward direction, while the geometrical efficiency was calculated with the simulation under the same conditions. This intrinsic efficiency was then included in the GEANT4 simulations [192] to obtain realistic total efficiency factors for larger multiplicities of light-charged particles with $Z = 1$. This is required because the larger multiplicities contaminate the lower ones.

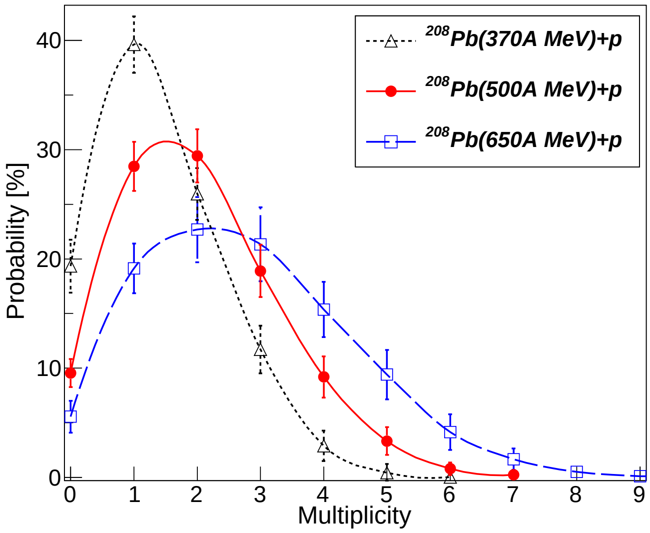

Figure 3.9: *(Color online) Probability of emission of particles with $Z = 1$ as a function of the multiplicity for the reaction $^{208}Pb + p$ at different kinetic energies.*

Figure 3.9 shows the probability of emission of particles with $Z = 1$ in fission events as function of the total multiplicity of light-charged particles per event for the reaction ^{208}Pb + p at 370A (open triangles), 500A (solid dots), and 650A (open squares) MeV. These distributions were obtained after appling the correction factors shown in Fig. 3.8 to the measured multiplicity distributions. Due to fact that the maximum multiplicity detected by the ToF wall is six (maximum number of paddles), the tails of the distributions were extrapolated, as shown in Fig. 3.10. In this figure, the measured yields (solid triangles) were divided by the total efficiency factors of Fig. 3.8, leading to the corrected yields (open squares). The tails of these corrected yields were then extrapolated with a gaussian fit (solid line) to determine the contribution of the multiplicities larger than six. Finally the distribution of multiplicities was normalized to 100, leading to the results shown in Fig. 3.9.

In Fig. 3.9, the maximum of these distributions is close to lower multiplicities, as expected because most of the fissioning systems are produced in peripheral collisions near the projectile. Then the tails observed towards larger multiplicities can be attributed to the production of lighter fissioning nuclei or higher excitation energies. As can also be seen in the figure, the probability of larger multiplicities, as well as the maximum of the distribution, increase when increasing the bombarding energy. This tendency can be attributed to the increase of the violence of the reaction (more particles removed or emitted from the fissioning system).

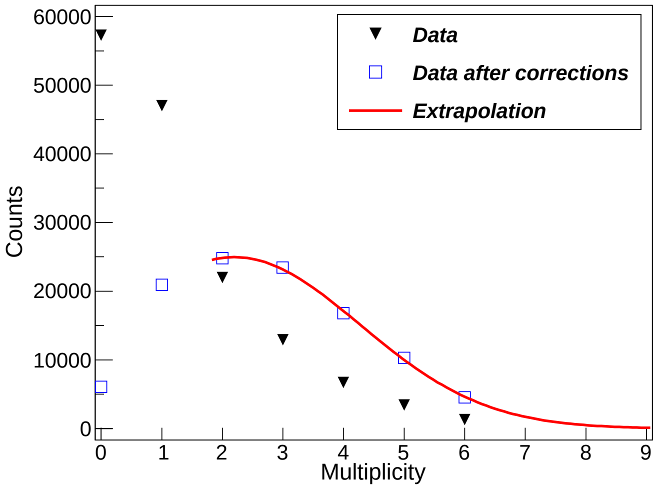

Figure 3.10: *(Color online) The measured distribution of particles with* $Z = 1$ *for the reaction* $^{208}Pb + p$ *at 650A MeV is shown in comparison to the one after the corrections. The solid line represents the gaussian extrapolation.*

The emission of particles in fission can also be studied with respect to other deexcitation mechanims that end in evaporation residues. For this purpose, the total number of particles detected in fission for each charge $Z = 1, 2, 3, ...$ was normalized to the one obtained with no fission selection. These ratios as a function of the charge of the emitted particles are shown in Fig. 3.11(a) for the reactions measured in this work: ^{208}Pb + p at 370A

(open triangles), 500A (solid dots), and 650A (open squares) MeV, and ^{208}Pb + ^{27}Al 500A MeV (solid triangles). The ratios seem to be very similar for charge $Z = 1$ and $Z = 2$ and slightly decrease for charge $Z = 3$. The ratios also increase with the energy of the reaction, which indicates an increase of the fission probability with respect to evaporation one.

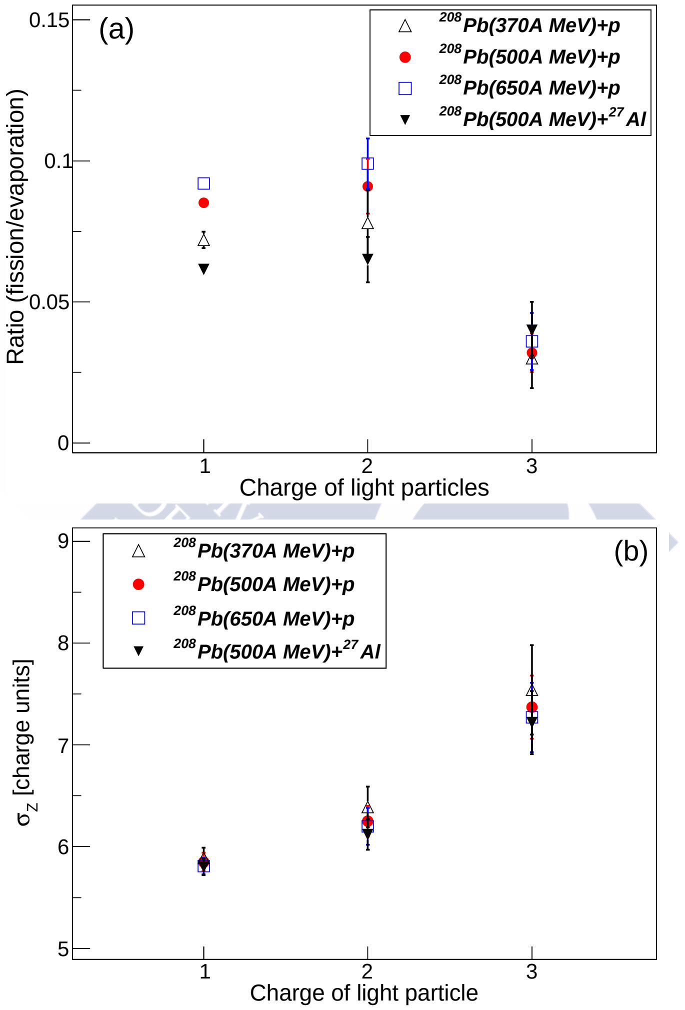

Figure 3.11: *(Color online) (a) Ratio of particles emitted in fission with respect to other deexcitation mechanims that mainly end in evaporation residues as a function of the atomic number of the removed light-charged particle from the projectile. (b) As (a) but for the width of the atomic-number distribution of the final fission fragments.*

The measurement of the light-charged particles allowed to investigate the evolution of the width of the atomic-number distribution of the fission fragments as a function of the charge of the emitted light particle, as shown in Fig. 3.11(b). Restrictions in the atomic number of the fissioning system (Z_1+Z_2) were also considered to avoid contaminations of higher multiplicities: $Z_1 + Z_2 > 80$ for $Z = 1$, $Z_1 + Z_2 > 79$ for $Z = 2$, and $Z_1 + Z_2 > 78$ for $Z = 3$. It is observed that the width of the charge distribution increases when increasing the charge of the emitted light particles. This increase of the width could indicate an increase of excitation energy at saddle [134] from a statistical point of view.

3.4 Discussion and comparison to model calculations

3.4.1 Dissipative effects

Different experimental observables such as the prescission particle emission [3, 6, 142] or the fission cross sections [8, 134, 135, 138, 210] indicate that fission at excitation energies above 100 MeV cannot be explained by purely statistical approaches like the transition-state method [2]. However, a description according to a diffusion process across the fission barrier seems more appropriate [8, 135]. In this picture, a dissipation coefficient couples the intrinsic and collective degrees of freedom determining how fast excitation energy is transformed into deformation. This coupling between excitation energy and deformation together with the stochastic nature of the process introduces an average time, or transient time, the system needs to reach a stationary fission flux across the barrier. The natural framework to describe these processes are transport equations such as the Fokker-Planck [146, 211] or Langevin [127, 141, 212] equations including the nuclear potential against deformation, a dissipative and a stochastic term.

Grangé and collaborators [146] established that the optimal conditions for investigating low-deformation dissipative and transient effects in fission were the use of spherical fissioning systems with low-angular momentum and excitation energies well above the fission barrier. Several works have tried to fulfill these conditions at least partially. A first example are alpha-induced fusion-fission reactions on tungsten targets at energies up to 140 MeV [7]. This experiment demonstrated that the measured excitation functions for the fission cross sections were compatible with a value of the transient time smaller than $\tau_{trans} = 1.2 \times 10^{-21}$ s [28]. Spallation reactions have also been used to induce fission in gold [134], uranium [161] and tantalum [138] targets. In these cases excitation energies up to several hundreds of MeV were reached and relatively low angular momentum was induced, but for the tantalum and uranium cases the fissioning systems were deformed. To describe the measured cross sections, calculations taking into account the initial deformation required dissipative and transient effects. The value of the reduced dissipation parameter used to describe the data was around (4.5 ± 0.5) × 10^{21} s^{-1}. Similar results were obtained in peripheral fragmentation reactions induced by different pre-actinides on a lead target by Schmitt and collaborators [137].

For the reaction investigated in this work, fission induced by relativistic protons on a lead target fulfills all the optimum requirements for the investigation of dissipative and transient effects in fission. Moreover, the combination of our measurements with validated previous ones, as discussed in section 3.1, will help one to provide a complete excitation function for the fission cross section of this reaction that will be used to investigate the onset of transient effects. For the present study, the code ABLA07 was modified in order to calculate fission rates using the Bohr-Wheeler statistical approach [2] or Kramers approach [79] (see also section 1.3.3).

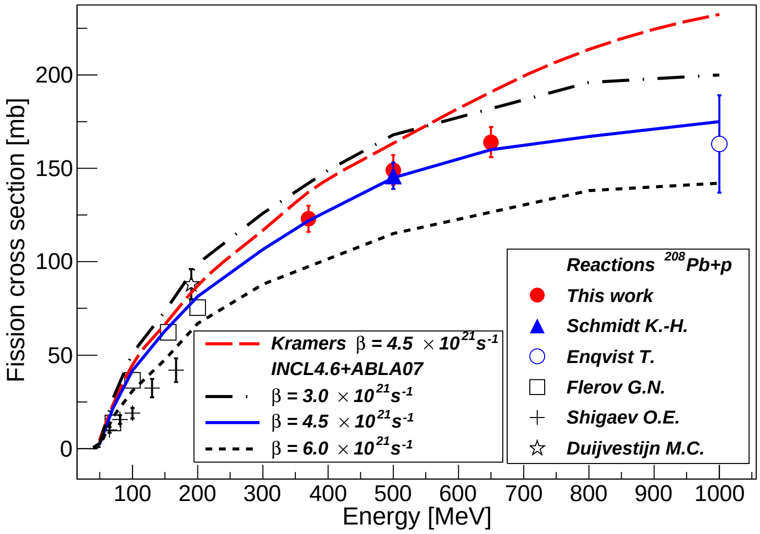

Figure 3.12: *(Color online) Total fission cross sections measured in this work (solid circles) and other experiments in comparison with a the dynamical description of fission based on a time-independent fission width given by Kramers (long-dashed line) and to calculations using INCL4.6+ABLA07 for different values of the reduced dissipation parameter.*

In Fig. 3.12 we show different calculations compared with the cross sections obtained in this work and other data validated in section 3.1. In this figure, the dashed line represents the result of a calculation taking dissipative effects with a value of the reduced dissipation parameter $\beta = 4.5 \times 10^{21}$ s^{-1} into account, but not considering transient effects. These calculations correspond to the description of the fission process proposed by Kramers (see section 1.3) [79]. As can be seen, this calculation clearly overestimate the fission cross sections at high proton energies. However, the calculations describe rather well the cross sections for proton energies below 200 MeV. This result is in agreement with other works [8, 146, 138, 210], where the authors did not observe transient time effects for excitation energies below 100-150 MeV.

In the same figure, the solid line corresponds to calculations considering a time-dependent fission width using the same value for the reduced dissipation parameter, $\beta = 4.5 \times 10^{21}$ s^{-1}, according to the prescription proposed in [167]. As can be seen, this calculation nicely describes the complete excitation function of fission cross sections. The comparison with the calculations without transient effects would indicate that these effects appear at excitation energies above 110 MeV. This onset of transient effects at relatively high excitation energies can be understood if one takes into account that the average fission delay induced by a reduced dissipation parameter $\beta = 4.5 \times 10^{21}$ s^{-1} corresponds to $\tau_{trans} = 1.2 \times 10^{-21}$ s. Therefore, such a short time delay can only be significant when the statistical time is of the same order.

The dotted-dashed and dotted lines in Fig. 3.12 represent similar calculations but with different values of the reduced dissipation parameter, $\beta = 3 \times 10^{21}$ s^{-1} and $\beta = 6 \times 10^{21}$ s^{-1} respectively. These additional calculations were used to illustrate that all cross sections can be described with the same value of the reduced dissipation parameter and consequently, no evidence for a temperature dependence is observed. These conclusions, the onset of transient effects at excitation energies above 110 MeV and the temperature independence of the reduced dissipation parameter coincide with the ones obtained in other works [8, 137, 146, 138].

To validate these conclusions on dissipation, these calculations are also confronted with the data obtained for the light-charged particles emitted in fission events. First, in Fig. 3.13(a) the average values of the multiplicity distributions of Fig. 3.9 are displayed as a function of the projectile bombarding energy. The comparison to model calculations based on the Bohr-Wheeler transition approach [2] (short-dashed line), Kramers approach [79] (long-dashed line), and ABLA07 [160] (solid line) reveals that this observable is very sensitive to transient time effects. The same result is observed

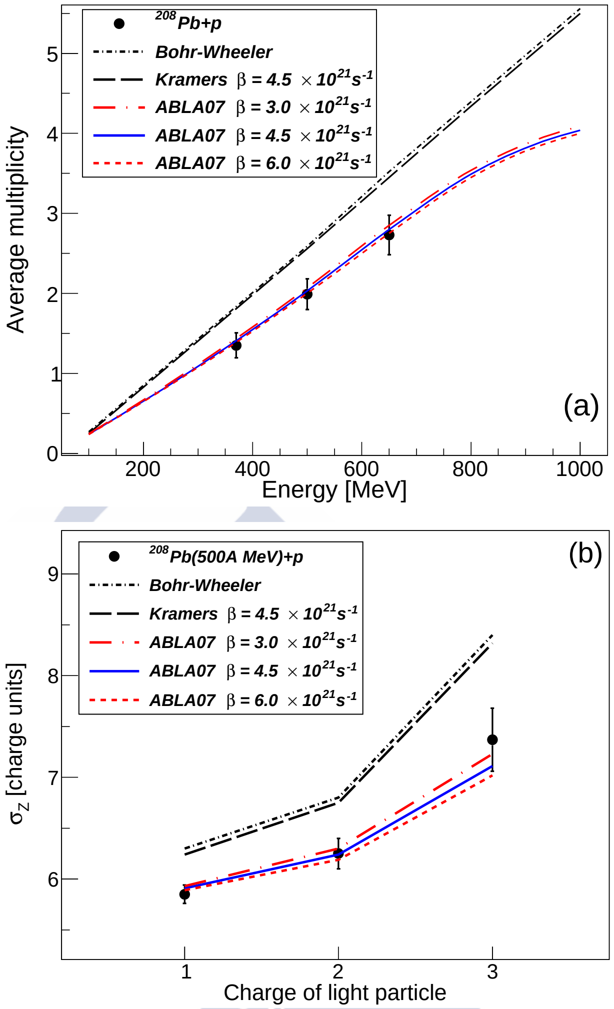

Figure 3.13: *(Color online) (a) Average multiplicity of particles with* $Z = 1$ *as a function of the projectile bombarding energy for the reaction* $^{208}Pb + p$*. (b) Width of the atomic-number distribution of the final fission fragments measured in the reaction* $^{208}Pb(500A\ MeV) + p$ *as a function of the atomic number of the removed light particle from the projectile. In both figures the data are compared with different model calculations (lines).*

for the widths of the charge distributions of the reaction ^{208}Pb(500A MeV) + p displayed in Fig. 3.13(b). As can be observed in both figures, statistical calculations clearly overestimate the data for both observables. This same result is obtained for dissipative calculations based on the Kramers approach. On the other hand, ABLA07 calculations considering dissipative and transient time effects provide a good description. The same comparison is performed in Fig. 3.14 for the ratios of particles emitted in the reaction ^{208}Pb(500A MeV) + p displayed in Fig. 3.11(a). As can be observed, dissipative and transient time effects are also needed to describe this observable. However, these observables do not seem to be sensitive to the value of the reduced dissipation parameter β.

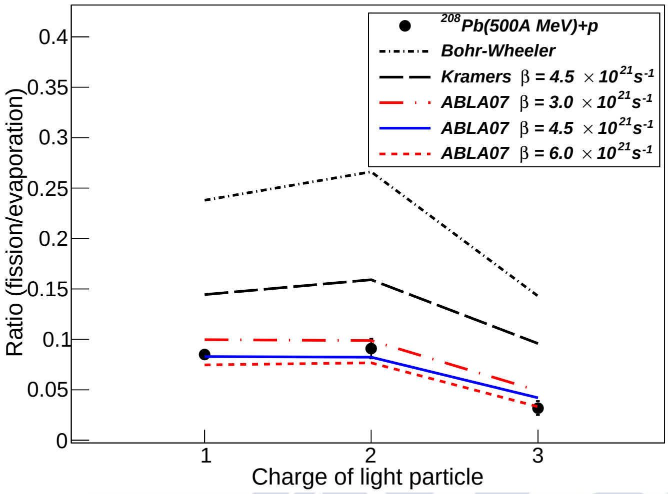

Figure 3.14: *(Color online) Ratio of particles emitted in fission with respect to other deexcitation mechanims that mainly end in evaporation residues. The lines represent different model calculations. The data are compared with different model calculations (lines).*

The investigation of the partial fission cross sections and the width of the atomic-number distribution of the fission fragments are not shown because we obtain the same results found in other works [27, 28, 137, 136]. Using fission reactions induced by ^{238}U projectiles impinging on a CH$_2$ target, Jurado and collaborators [27] found that the partial fission cross sections are sensitive to the dissipation parameter because that observable is strongly correlated with the total fission cross sections, which depend on dissipative and transient effects as shown in Fig. 3.12. On the other hand, they found that the width of the atomic-number distribution of the fission fragments is more sensitive to transient time effects than the value of the dissipation parameter. The same observables were also studied by Schmitt and co-workers [137, 136, 213] using spherical radioactive heavy nuclei, obtaining the same results. Both conclusions were also confirmed by Ayyad and collaborators [28] for the reactions ^{208}Pb(500A MeV) + p and ^{208}Pb(500A MeV) + d. Therefore, total and partial fission cross sections seem to be more sensitive to the value of the dissipation parameter while other observables, such as the width of the atomic-number distributions of the fission fragments and the light-charged particle multiplicities, are more sensitive to transient time effects.

3.4.2 Constraining the level-density parameter

Several recent works have proposed empirical modifications of this parameter in order to describe fission rates [214, 215]. These authors claim that fission rates can be described, even at high excitation energies, without considering any transient time for fission. This conclusion contradicts the well-established role of dissipative effects in the ground-to-saddle fission dynamics to explain pre- and postscission neutron multiplicities [3], γ-ray emission [5], multiplicities of charged particles [6], as well as fission and evaporation residue cross sections [8, 135, 138, 194].

The origin for such contradictory conclusions could be that an effective reduction of the level-density parameter at the saddle point with respect to the ground-state value could mimic the fission hindrance induced by dissipative effects. Therefore many authors claim that conclusions based only on the use of fission rates to constrain the different parameters contributing to the description of this process may lead to ambiguous results [7, 9, 134, 137, 143, 194].

For the investigation of the dependence on the level density, the fission cross sections depicted in Fig. 3.12 are also contrasted with model calculations using several assumptions to describe the level-density parameter. The results of the different calculations are shown in Fig. 3.15(a). The dot-short-dashed and double-dot-dashed lines represent statistical calculations for two different constant values of the level-density parameters, $A/8$ and $A/12$, respectively. These calculations provide a reasonable description of the measured cross sections at low energy but clearly underestimate the data for proton energies above 300 MeV. In any case, these parametrizations of the level density parameter are not too realistic because they do not consider the deformation correlations at the ground state (a_{gs}) and at the saddle point (a_{sd}).

The same statistical calculation using Ignatyuk's parametrization (see section 1.1.3) for the level-density parameter (solid line) shows an overestimation of the data that increases with the proton energy. Finally, the dotted line corresponds to another statistical calculation where the level-density parameter at ground-state deformation was obtained using Ignyatyuk's parametrization while the same parameter at saddle deformation was obtained as $a_{sd}/a_{gs} = 1.034$ following Ref. [214]. One can observe that this calculation describes rather well the data for proton energies above 400

MeV, but it overestimates the data at lower energies. This fact could indicate that the factor between the level-density parameters at the ground state and saddle is not constant with the energy due to the difference in the fissioning system with the proton energy.

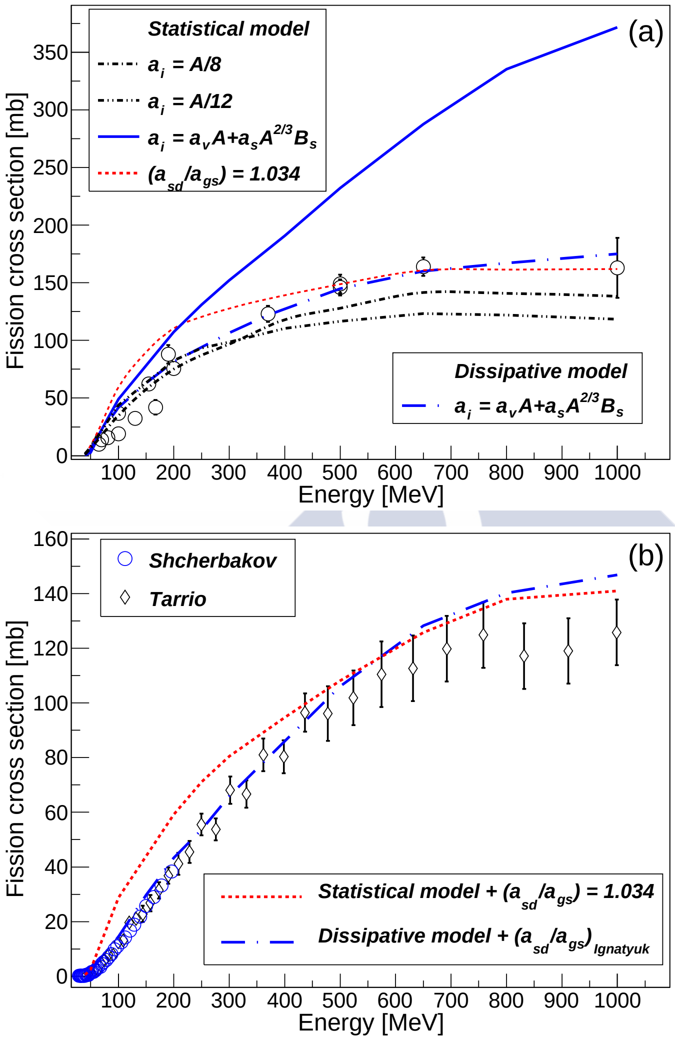

Figure 3.15: *(Color online) (a) Comparison of the fission cross sections for the reaction ^{208}Pb + p as a function of the bombarding energy with different model calculations (lines). (b) As (a) but for the the reaction ^{nat}Pb + n. The data are taken from Refs. [216, 217].*

In the same figure, the dot-long-dashed line represents a calculation considering dissipative and transient time effects with a reduced dissipation parameter $\beta = 4.5 \times 10^{21}$ s^{-1}, according to the previous conclusion. In these calculations the level-density parameter at the ground-state and the saddle-point deformations was obtained from Ignatyuk's parametrization. These calculations provide a satisfactory description of the total fission cross sections for the complete range in proton energy covered by Fig. 3.15(a). Same results were also found by Ye and Wang for fusion-fission cross sections of pre-actinides using the Langevin approach [9] together with different descriptions of the level-density parameter. From the comparison of the calculations with the data Ye and Wang found that Ignatyuk's parametrization provides a better description of the evolution of the fusion-fission cross sections with the excitation energy, using a value of $(4.0-4.5) \times 10^{21}$ s^{-1} for the reduced dissipation parameter.

Same conclusions are found when the calculations are compared to the total fission cross sections induced by neutrons on ^{nat}Pb over the same range of energy covered by our data, but investigated in direct kinematics, as shown in Fig. 3.15(b). The open circles represent a rather complete set of data up to 200 MeV obtained by Shcherbakov and collaborators [216]. The open diamonds correspond to the only existing set of data for energies above 200 MeV measured by Tarrio and collaborators [217]. The cross sections above 200 MeV were measured relative to ^{235}U. Absolute values were obtained using evaluated total fission cross sections of ^{235}U taken from JENDL/HE-2007 evaluation [218, 219]. Here we only depict the results of two of the calculations previously discussed, the statistical calculation with a constant value of the ratio of the level-density parameter at ground-state and at saddle deformations $a_{sd}/a_{gs} = 1.034$ (dotted line), and the calculation based on the description of the fission dynamics as a dissipative process using the parametrization of lgnatyuk to calculate the value of the level-density parameter at ground-state and saddle deformations (dot-long-dashed line). As observed for proton-induced reactions the statistical calculations with a fixed ratio for the level-density parameter at ground and at saddle deformation overestimate the measured cross sections for neutron energies below 400 MeV. The dynamical calculation with a deformation-dependent level-density parameter provides a satisfactory description of the data in this energy range. At higher energies both calculations yield similar results.

The ABLA07 model calculations shown in Fig. 3.15(b) reproduce the data very well up to 550 MeV and within the error bars up to 750 MeV. Above that energy value the calculations overestimate the data. Proton-induced fission reactions have been intensively investigated at GSI at energies around 1000A MeV with tantalum [138], gold [134], lead [21] and uranium targets [161]. Total fission cross sections obtained in these measurements were reasonably well reproduced by the same model calculations and parameters [138, 159] we use to describe the neutron-induced fission cross sections of Fig. 3.15(b). This validation of ABLA07 model calculations with reactions induced by protons around 1000 MeV and the good description of the neutron data at energies below 750 MeV could indicate some problem with the data shown in Fig. 3.15(b) above 750 MeV, that would be also supported by the unexpected reduction in the measured cross sections above that energy value.

The overall good description of the neutron-induced fission cross sections with the same model calculations that also reproduce the proton-induced fission allows us to validate two independent sets of data, at least up to 650 MeV, and represents an additional support to the conclusions obtained with respect to the magnitude and temperature independence of the reduced dissipation parameter.

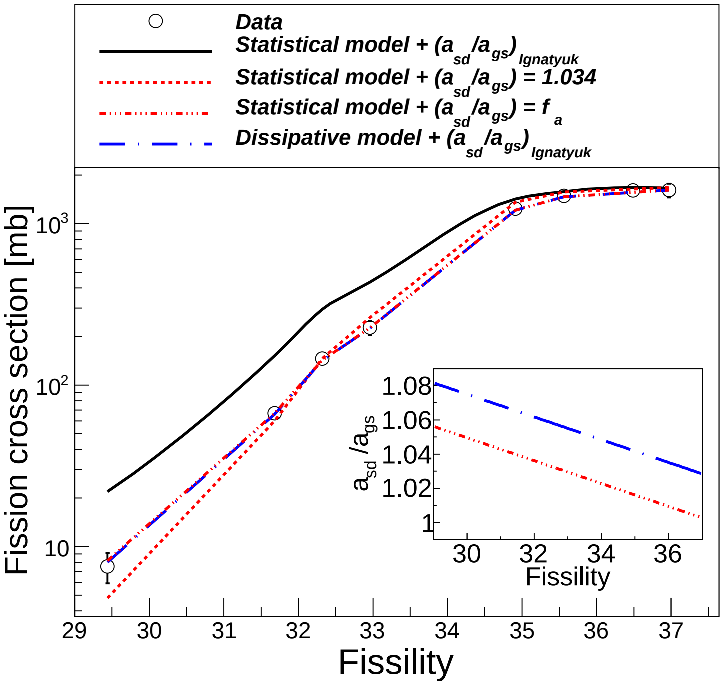

Figure 3.16: *(Color online) Fission cross sections at 500 MeV of different nuclei obtained from Refs. [138, 206] as a function of the fissility. The lines indicate different model calculations. In the inset we show the ratio a_{sd}/a_{gs} obtained by our model calculations as a function of the fissility.*

To investigate a possible dependence of the ratio of the level-density parameter at the ground-state and at the saddle-point deformations with the fissility, in Fig. 3.16 we compare our model calculations with proton-induced fission cross sections obtained for several actinides and pre-actinides between ^{181}Ta and ^{237}Np at 500 MeV, taken from Refs. [138, 206]. These data allow us to cover a large range in fissility. In the figure one can observe that a statistical model calculation with a deformation-dependent description of the level-density parameter based on the parametrization of Ignatyuk (solid line) overestimates the data, while a statistical calculation with a constant value for the ratio of the level-density parameter at the ground-state and at the saddle-point deformations $a_{sd}/a_{gs} = 1.034$ (dotted line) underestimates the fission cross sections for nuclei below ^{208}Pb. However, the fission cross sections can be described using the same calculation with a fissility-dependent ratio $a_{sd}/a_{gs} = f_a$ (triple-dot-dashed line). On the other hand, one can also describe the data using a dynamical calculation with a reduced dissipation parameter $\beta = 4.5 \times 10^{21}$ s^{-1} (dot-long-dashed line). In the inset of the same figure we represent the ratio a_{sd}/a_{gs} calculated according to Ignatyuk's parametrization (dot-long-dashed line) and the variable ratio (f$_a$) used in the statistical model calculation (triple-dot-dashed line) as a function of the fissility. The observed offset between the displayed ratios could be attributed to the reduction induced in the stationary fission decay width by dissipation.

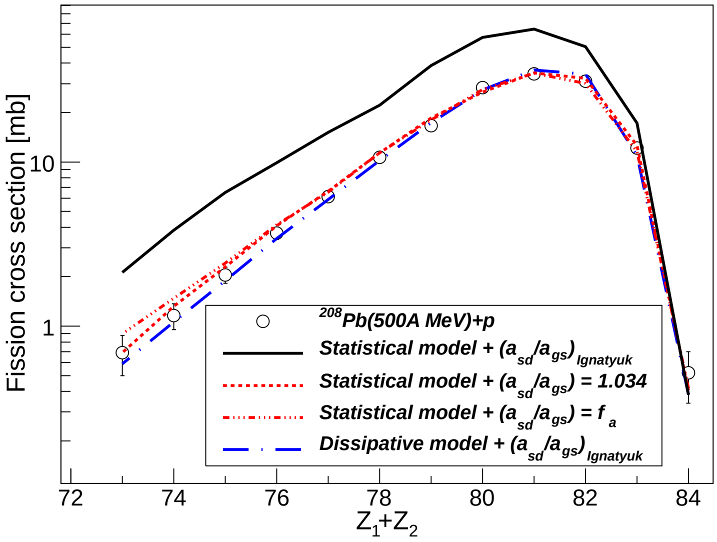

Figure 3.17: *(Color online) Fission cross sections of the reaction* $^{208}Pb + p$ *at* $500A$ *MeV as a function of the atomic number of the fissioning nuclei (open circles). The lines represent different model calculations.*

In Fig. 3.17 the partial fission cross sections of the reaction ^{208}Pb(500A MeV) + p (open circles) obtained in section 3.2 are compared with different calculations. Calculations based on a statistical description of the fission width and using the deformation-dependent parametrization of the level-density parameter proposed by Ignyatuk et al. [105] overestimate the fission cross sections except for the heaviest fissioning nuclei with the lowest excitation energies (solid line). All other calculations previously discussed provide a reasonable description of the data. This benchmark using dynamical and statistical approaches to describe the fission decay width as well as different prescriptions for the level-density parameter indicates that this observable does not show then a clear sensitivity to different descriptions of the level-density parameter.

From these calculations, we could conclude that the total fission cross sections can be described by two approaches, a statistical model with a modified ratio a_{sd}/a_{gs} and a dissipation model with a deformation-dependent ratio a_{sd}/a_{gs} calculated within Ignatyuk's parametrization. Therefore, total and partial fission cross sections alone cannot be used to disentangle between these two approaches and additional observables are needed.

In order to overcome this situation we propose to use the width of the charge distribution of the fission fragments that was used previously to investigate ground-to-saddle dissipative effects [27, 28, 137]. According to equation 1.4, this observable depends on the temperature at the saddle point (T_{sd}) which is related to the excitation energy at saddle (E^*_{sd}) as $T_{sd} = \sqrt{E^*_{sd}/a_{sd}}$. Therefore, the width of the atomic-number distribution could also represent a useful probe to investigate the description of the level-density parameter at the saddle point, providing another important constraint for model calculations.

In Fig. 3.18 we confront the data shown in Fig. 3.6 to the different model calculations discussed previously. The calculations for the reaction ^{208}Pb(500A MeV) + ^{27}Al were performed with the code ABRABLA07 that consists of the coupling of the abrasion model developed by Gaimard and Schmidt [156] to the deexcitation code ABLA07 [160].

The first conclusion is that for the heaviest fissioning nuclei with the lowest excitation energies there is no sensitivity to the parameters used in the different calculations. The same conclusion was obtained when this observable was used to constrain ground-to-saddle disipative effects [28]. The reason is that at low excitation energies, close to the projectile, dissipative effects are negligible. For fissioning systems lighter than $Z_1 + Z_2 < 76$ we observe a sensitivity to the different descriptions of the level-density parameter and the fission decay width. Statistical descriptions of the fission decay width (dot-dashed line for the reaction ^{208}Pb(500A MeV) + p and dotted line for the reaction ^{208}Pb(500A MeV) + ^{27}Al) clearly overestimate the width of the charge distributions even when using the phenomenological description of the level-density parameter that reproduces fission cross sections (triple-dot-dashed line). Only calculations considering dissipative effects in the fission decay width and a deformation-dependent level-density parameter following Ignyatuk's parametrization provide a satisfactory description of the width of the charge distributions of the fission fragments (solid line for the reaction ^{208}Pb(500A MeV) + p and dot-long-dashed line for the reaction ^{208}Pb(500A MeV) + ^{27}Al), but also of the fission cross sections.

The same results and conclusions were obtained in other works [28, 137, 167], where the authors compared the widths of the charge distributions of the fission fragments with statistical and dissipative model calculations using a dynamical description of the level-density ratio based on the parametrization of Ignatyuk. Moreover, those works indicated the need of a dissipative calculation with transient time effects to achieve a complete description of the data, which is in good agreement with our results.

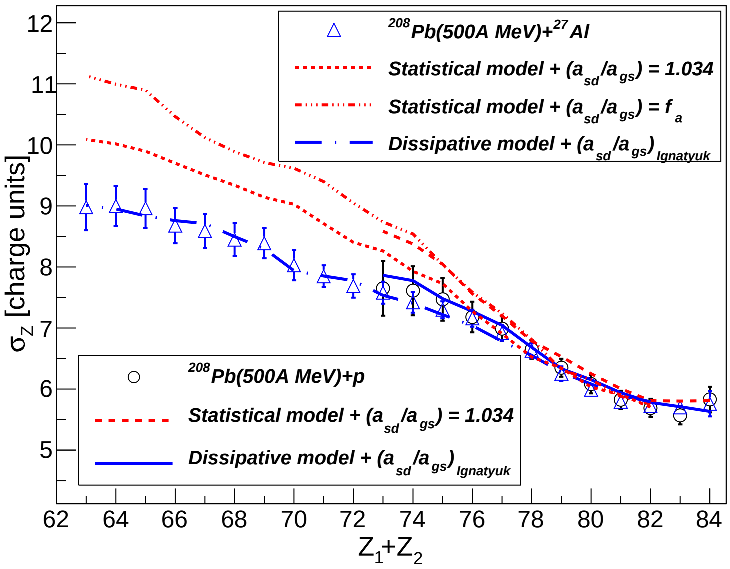

Figure 3.18: *(Color online) Width of the atomic-number distribution of the final fission fragments for the data of the reaction* $^{208}Pb(500A\ MeV) + {}^{27}Al$ *(open triangles) and* $^{208}Pb(500A\ MeV) + p$ *(open circles) as a function of the atomic number of the fissioning nuclei. The lines represent different model calculations.*

3.5 Conclusions

In the present chapter, we have investigated spallation- and fragmentation-induced fission of ^{208}Pb in inverse kinematics at different bombarding energies using a highly efficient detection setup that permitted us to measure the atomic number of the two fission fragments in coincidence with good resolution. With these measurements we were able to determine with high accuracy the total fission cross section, the partial fission cross sections and the width of the charge distribution of the fission fragments as a function of the sum of the charges of the two fission fragments as well as the light-charged particles multiplicities.

The total fission cross sections allowed us to clarify the existing discrepancies in previous measurements of proton-induced fission of ^{208}Pb at intermediate and high energies. These data also helped us to revisit the previously established systematics by Prokofiev [12] and propose a new parametrization for proton-induced fission cross sections of ^{208}Pb. Moreover, we have used these data to benchmark different model calculations to describe the fission decay width and the level density at ground-state and at saddle-point deformations. In particular, we have used a purely statistical description of the fission decay width based on the transition-state method and a dynamical description of the process in terms of a time-dependent fission decay width produced by the coupling between the heat bath describing the excited fissioning nucleus and its collective degrees of freedom through a dissipation parameter. As for the level densities we have used a back-shifted Fermi gas with different descriptions of the level-density parameter; values proportional to the mass number of the nucleus with a constant ratio between the level-density parameters at ground-state and at saddle-point deformations as well as a complete description of this parameter at the saddle and scission configurations using Ignyatuk's prescription [105].

The analysis of the reactions proton- and neutron-induced total fission cross sections of ^{208}Pb and ^{nat}Pb, respectively, as well as partial fission cross sections as a function of the sum of the charges of both fission fragments show that it is possible to combine different models that describe the fission decay width and parametrizations of the level-density parameter to describe the data. This can be understood because we try to describe a multi-parametric problem with a single boundary condition. It is then clear that an unambiguous benchmarking of fission models requires several independent observables.

The width of the charge distribution of the fission fragments was used as additional constraint for model calculations. Using this observable we show that fission of ^{208}Pb at high excitation energies can only be described properly using dissipative and transient effects together with a realistic description of the level-density parameter taking into account the deformations of the ground-state and saddle-point configurations.

The overall good description of the proton- and neutron-induced fission cross sections, partial fission cross sections, widths of the charge distributions and light-charged particles multiplicities with the same dissipative model calculations allowed us to validate the conclusions obtained with respect to the magnitude and temperature independence of the reduced dissipation parameter at small deformations, leading to a constant value of $\beta = 4.5 \times 10^{21}$ s^{-1}.

Finally, it is worthwhile to mention that all the work of this chapter to study the dynamics of the fission process at small deformations, between the ground-state and the saddle-point configurations, will make it possible to investigate fission at large deformations. In particular, we will be able to study the saddle-to-scission dynamics and the scission point properties, as will be illustrated in chapter 4.


USC
UNIVERSIDADE
DE SANTIAGO
DE COMPOSTELA

Chapter 4

Postsaddle fission dynamics

In chapter 3 we have investigated the dissipative effects at small deformations. We have found that a constant value of the reduced dissipation parameter can describe all the observables sensitive to dissipation in the deformation regime from the ground-state to the saddle-point configuration. Moreover, the same value of the reduced dissipation parameter also reproduces the measurements obtained in other reactions covering a large range in excitation energy, leading to an independence of this parameter on temperature. The good description of these observables also provides us an accurate characterization of the fissioning nucleus at saddle as the starting point to investigate the saddle-to-scission dynamics.

Concerning to the observables sensitive to the fission dynamics at large deformations, different works based on heavy-ion induced fusion-fission reactions have used the analysis of prescission particle [3, 6] and γ-ray [142] multiplicities to extract information on dissipation. However, the large angular momentum induced in these reactions could affect the conclusions because elaborated dynamical codes are required to describe the initial conditions of the compound nucleus. On the other hand, as shown in chapter 3 one needs several observables for an unambiguous constraining of the reduced dissipation parameter. To improve this situation, new independent observables sensitive to dissipation at large deformation should be introduced and combined with the previous ones to investigate the saddle-to-scission dynamics, which could help us to study the dependence of the reduced dissipation parameter on deformation.

In this chapter we use the complete kinematic measurement of the two fission fragments produced in the reaction ^{208}Pb(500A MeV) + p to investigate the dissipative effects at large deformation. As discussed in the pioneering work of Grangé and collaborators [146], the optimal conditions for investigating small-deformation dissipative and transient effects in fission are the use of spherical fissioning systems with low angular momentum and high excitation energies ($E^* > 100$ MeV). Fortunately, these conditions also represent a good approach to study dissipation at large deformation because high excitation energies favor the evaporation of neutrons beyond the saddle point, while the low angular momentum induced in the compound nucleus and its spherical configuration favor the comparison of the data with model calculations.

Section 4.1 of this chapter is dedicated to the determination of the cross sections of the charge distributions of the fission fragments produced in the reactions ^{208}Pb(370A, 500A, and 650A MeV) + p and ^{208}Pb(500A MeV) + ^{27}Al and the isotopic cross sections of the reaction ^{208}Pb(500A MeV) + p. Section 4.2 is devoted to the analysis of the properties of the fission fragments, such as the neutron excess, widths of the isotopic distributions, and velocities of the fission fragments. These observables are compared with different model calculations to provide an interpretation of them and to extract information on the fission process beyond the saddle-point configuration. In particular, the correlations between the two fragments will be used to assess the role of charge polarization and the excitation energy gained by the nascent fragments using the neutron excess of the final fragments. Moreover, the analysis of the average velocities of the fission fragments is used to parameterize the distance between the two fission fragments at scission as a function of the size of the fissioning system. Section 4.3 is dedicated to reconstruct the total and pre- and postscission neutron multiplicities by using the velocities and the isotopic composition of the two fission fragments. Finally, section 4.4 is devoted to investigate dissipative effects between the saddle-point and the scission configurations using the neutron multiplicities. Moreover, the average neutron excess of the final fission fragments as a function of the size of the fissioning system is presented as a new observable sensitive to dissipation at large deformations, which could provide new constraints for model calculations.

4.1 Isotopic distribution of the final fission fragments

The isotopic distributions of the fission fragments are one of the key observables for the understanding of the fission process and could provide valuable information about the excitation energy gained by the fissioning nucleus in the reaction as well as some of its properties at scission, such as polarization and shell effects [20, 35, 64, 118, 141, 177, 220, 221, 222, 223]. These data are also used to validate a previous controversial measurement of the isotopic distributions of the fission fragments produced in the reaction ^{208}Pb(500A MeV) + p, performed at the FRS spectrometer at GSI [187].

4.1.1 Yields

The SOFIA setup (see chapter 2), used in the present work, allowed us an unambiguous identification in mass and atomic number of the two fission fragments. The atomic number of the two fission fragments was determined from energy-loss measurements using a double ionization chamber Twin MUSIC with atomic-number resolutions around 0.43 charge units (FWHM), while the mass numbers were obtained by using magnetic rigidity and time-of-flight measurements with resolutions around $\Delta A/A \sim 0.63\%$ (FWHM). Both measurements allowed us to determine the fission yields with high precision. The efficiency of the detectors under fission condition was always above 98% with an uncertainty around 2%.

4.1.2 Corrections

In this section we will describe the corrections applied to the measured isotopic yields in order to account for the limited detection and geometrical efficiency of the experimental setup. The most important corrections are due to secondary reactions, atomic charge states, and transmission of the fission fragments along the detection setup.

Secondary reactions in the experimental setup can be produced by two mechanisms: fission of an evaporation residue produced by a first spallation reaction or spallation of a fission fragment. In the first case, the probability to produce a fission event was estimated to be around 2.1% (see Ref. [197]) and its effect on the identification is negligible, however, the second mechanism is more important for an accurate identification. In order to describe the contribution to the measured yields due to spallation reactions of fission fragments, the INCL4.6 [159]+ABLA07 [160] code was used. This code describes rather well the total reaction cross sections and the isotopic distributions of the residual fragments close in atomic and mass number to the projectile produced in spallation reactions [159].

Figure 4.1 shows this correction factor (f_{sc}) with its associated uncertainty (dashed area) for several elements as a function of the mass number of the fission fragments. As can be seen in the figure, the global effect of secondary reactions is to reduce the yields of neutron-rich fragments in favor of neutron-deficient ones. The main uncertainty of this correction factor comes from the total reaction cross sections calculated with the INCL4.6 model with an uncertainty around 5%.

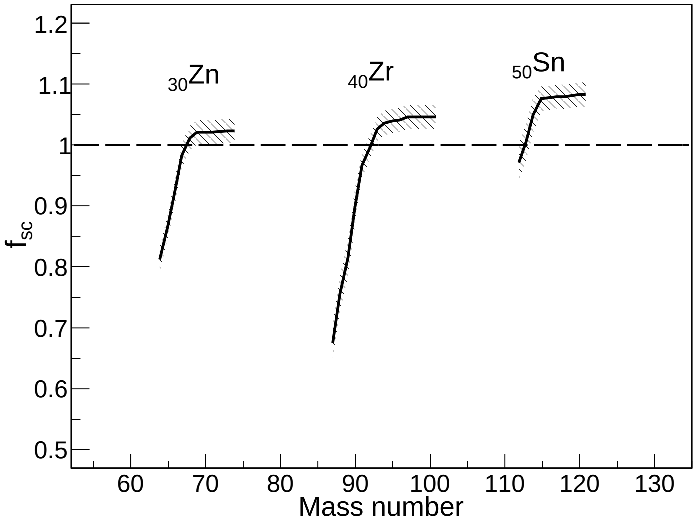

Figure 4.1: *Correction factor of secondary reactions (f_{sc}) is displayed for three elements ($_{30}Zn$, $_{40}Zr$, and $_{50}Sn$) as a function of the mass number.*

The correction factor from atomic charge states (f_q) is needed for an accurate identification in the mass-over-charge ratio and was calculated along the setup by using the code GLOBAL [224]. This correction is negligible for nuclei with atomic numbers below 40 and increases exponentially up to 15% for $Z = 55$. The uncertainty of this correction varies from 4% to 1% for the atomic numbers $Z = 55$ and $Z = 40$, respectively.

The experimental setup used to measure the fission fragments has also some geometrical constraints affecting the measured yields. These correction factors are obtained using GEANT4 simulations [191, 192, 193]. The transmission corrections are calculated by counting the number of simulated fission fragments traversing the experimental setup with respect to the total number of simulated ones. In these calculations, only simulated fission events where both fission fragments are transmitted along the experimental setup were counted as fission events.

In Fig. 4.2 we show the different contributions with their associated uncertainties (dashed areas) to the correction accounting for the transmission of the fission fragments through the experimental setup. The solid line corresponds to the transmission correction factor due to the dead zone produced by the central vertical cathode of the Twin MUSIC chamber and to the probability that both fission fragments pass through the same part of this detector. The long-dashed line includes the previous correction but also the one due to the limited size of the helium pipe situated in front of the Twin MUSIC. Finally, the short-dashed line represents the transmission taking into account all geometric constraints along the setup, including the losses in the ToF Wall. As can be seen in the figure, the transmission corrections are more important for lighter and heavier fragments because of the angular aperture of the lighter fragments.

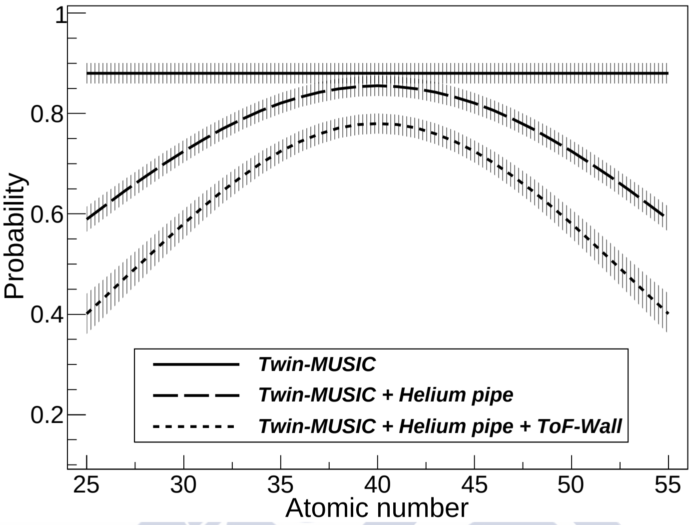

Figure 4.2: *Transmission as a function of the atomic number of the fission fragments. The lines represent the transmission corrections taking into account the geometrical constraints indicated in the figure.*

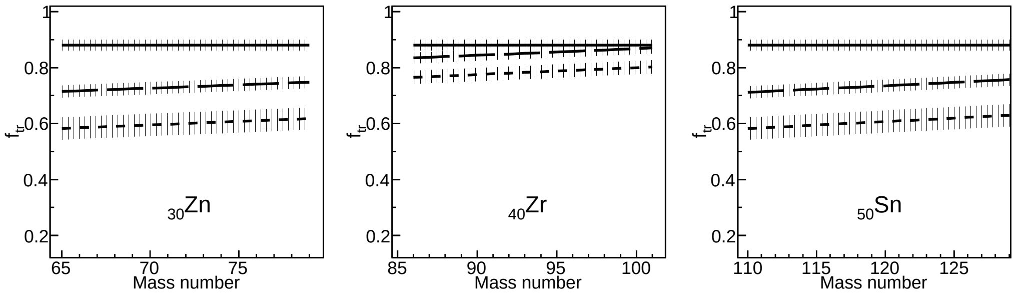

Figure 4.3: *Transmission coefficient (f_{tr}) as a function of the mass number for three elements: $_{30}$Zn (left), $_{40}$Zr (center), and $_{50}$Sn (right). The lines represent the transmission corrections taking into account the geometrical constraints indicated in Fig. 4.2.*

Figure 4.3 shows the same corrections but in form of isotopic distributions for three elements: ${}_{30}Zn$, ${}_{40}Zr$, and ${}_{50}Sn$. As can be seen in the figure, the evolution of the correction with the neutron excess is similar for the three elements although, it is more important for the light fragments because of their larger angular apertures. The uncertainty of this correction is smaller than 5%.

4.1.3 Cross sections

In order to determine the production cross sections of the fission fragments, the measured isotopic yields were extracted from Fig. 2.15. The real production yields *Y(Z,A)* were then obtained by correcting the measured yields *N(Z,A)* by the factors accounting for the limitations of the experimental setup according to:

$$Y(Z, A) = N(Z, A) f_{sc} f_q / f_{tr} \tag{4.1}$$

where f_{sc} is the correction factor due to secondary reactions of the fission fragments, f_q is the correction of the atomic charge states, and f_{tr} is the detection efficiency of the setup (see section 4.1.2). Finally, the isotopic cross sections are obtained normalizing the isotopic yields to twice the total fission cross section measured in the present experiment [197].

In Fig. 4.4 we show the measured isotopic cross section distributions of fission products (solid circles) for elements between cobalt ($Z = 27$) and tellurium ($Z = 52$). The values of the isotopic cross sections are also listed in the appendix. There was still some production by fission of fragments below cobalt and above tellurium, but these isotopic cross sections are not listed because the geometrical efficiency or mass resolution do not allow us to extract them with sufficient accuracy. The displayed measurement covers all the isotopes for each element with a statistical uncertainty below 10%. The complete isotopic production is compared with INCL4.6 [159]+ABLA07 [160] calculations (dashed lines). This comparison shows a very good agreement between our measurement and the calculations.

The distributions in atomic and mass number of the fission fragments are shown in Figs. 4.5(a) and 4.5(b), respectively. Figure 4.5(a) shows the atomic-number distribution of the fission fragments measured in this work (solid circles) by adding the yields of the fragments with the same atomic number. These data are compared with the previous measurement by Fernández-Domínguez and collaborators (open circles) [187] performed with the FRS spectrometer at GSI. In Ref. [197], it was shown that the total fission cross section obtained at the FRS spectrometer (232 ± 33 mb) presents a significant deviation from recent measurements by Schmidt and collaborators (146 ± 7 mb) [195] and the one determined in the present experiment (149 ± 8 mb) [197] for the same reaction and energy, and also from the systematic at different energies (see section 3.1). Therefore, for the comparison of the isotopic distributions the measurement of Fernández-Domínguez and collaborators was normalized to twice the total fission cross section measured in the present experiment.

This normalization was also applied in Fig. 4.5(b), where we compare the mass distribution of the fission fragments. As can be seen in both figures, our new measurements are in excellent agreement with the ones reported by Fernández-Domínguez (open circles) after normalization. Therefore, we can conclude that the problem with the previous measurement was only in the value of the total fission cross section. The reason for this discrepancy is not fully clear although the good agreement in the mass and charge distributions between the normalized FRS data and the present ones help us to exclude a problem with correction applied to the FRS data because of the limited angular acceptance. The discrepancy should then be caused by a wrong absolute normalization of the yields measured at the FRS.

In Fig. 4.6 our atomic-number distribution of ^{208}Pb + p at 500A MeV (solid circles) is compared with the other ones also studied in this work: 370A (open circles) and 650A MeV (open squares), and with the measurement performed by Enqvist and collaborators (solid triangles) [21] at 1000A MeV. The measurement of the reaction ^{208}Pb + ^{27}Al at 500A MeV is also displayed (open triangles). All the measurements seem to be in good agreement although an increase in the production of light fission fragments is observed when increasing the bombarding energy or size of target nuclei. This fact can be explained by the production of lighter fissioning nuclei and the larger excitation energies.

In order to investigate the energy dependence of the atomic- and mass-number distributions of the fission fragments, we compare our results with others obtained at different energies for similar systems. This is done in Tables 4.1 and 4.2, where the mean values and integral widths of the atomic- and mass-number distributions are listed respectively. The normalized values reported by Fernández-Domínguez and collaborators [187] are in excellent agreement with our results. The measurement of ^{208}Pb + p reported by Ayyad and collaborators [28] is also in agreement with our value taking its uncertainty bar into account. Our results are also in excellent agreement with the values reported by Hagebø and Lund [204], measuring the fragments produced in the fission of natural lead with protons at 600 MeV.

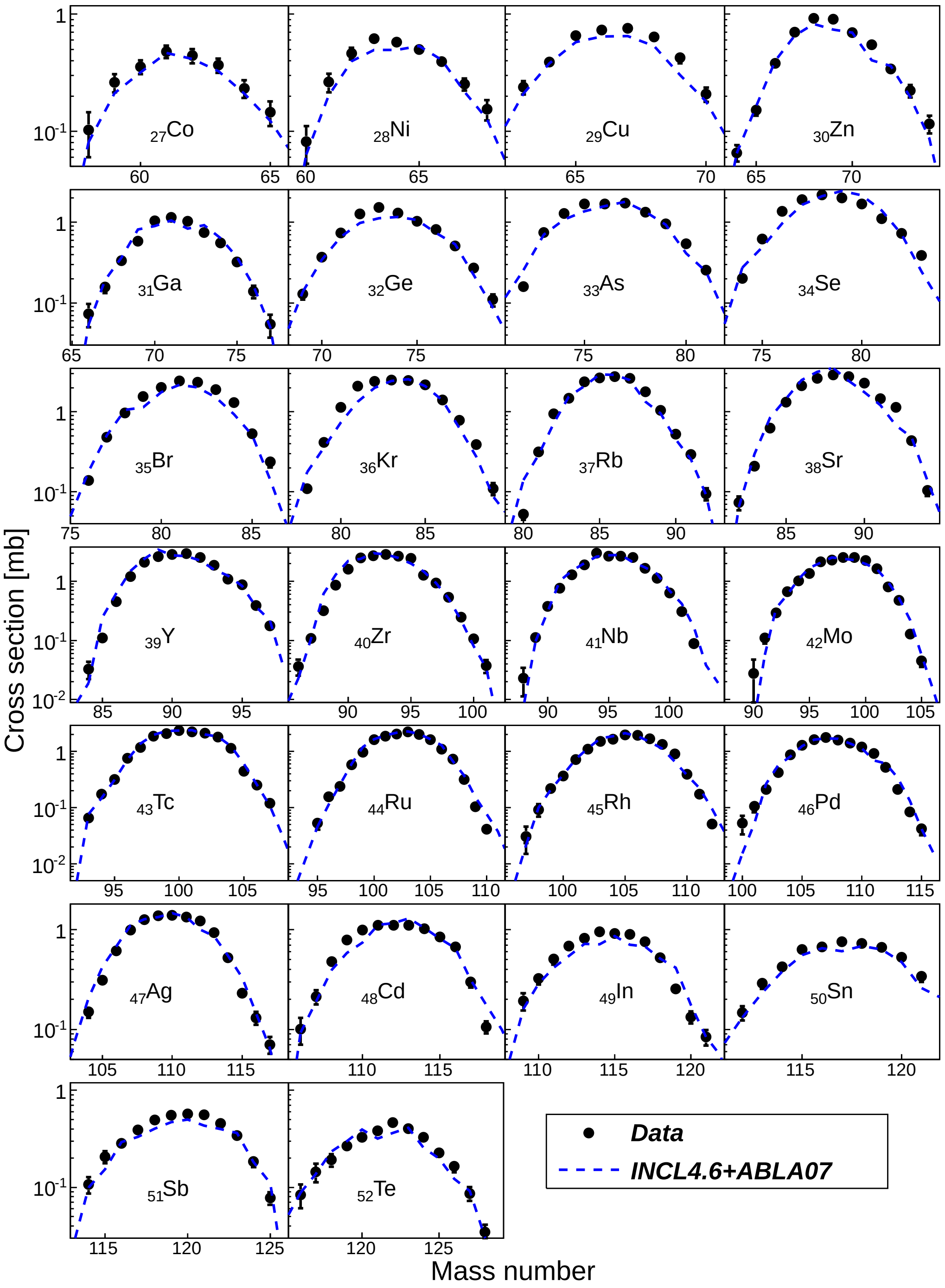

Figure 4.4: *(Color online) Isotopic cross sections measured in the reaction* ^{208}*Pb(500A MeV) + p corresponding to elements from cobalt to tellurium. Statistical uncertainty bars are shown if they exceed the size of the symbols. The dashed lines correspond to calculations.*

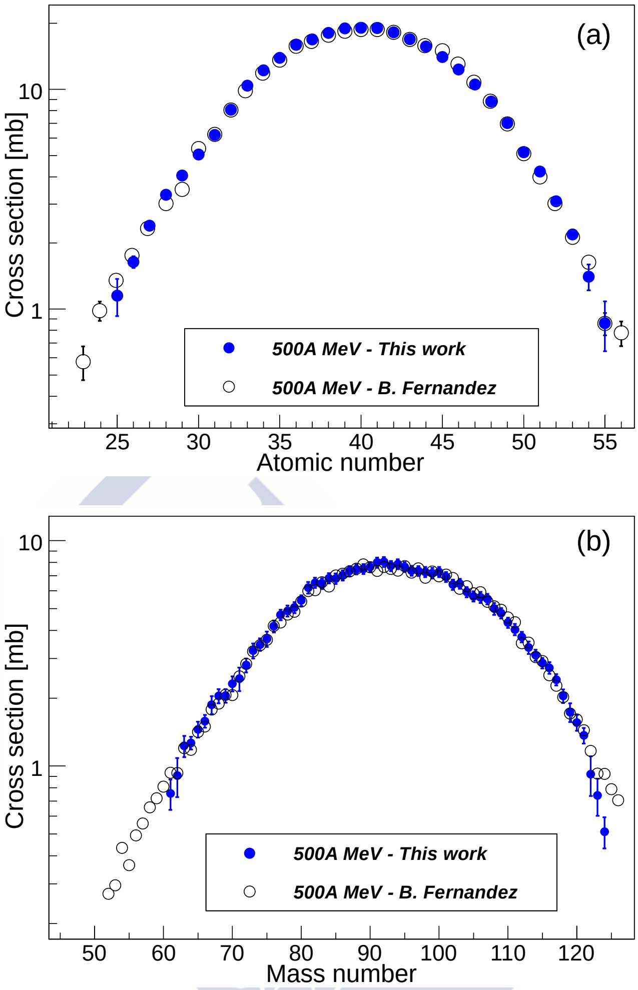

Figure 4.5: *(Color online) Cross sections of the final fission fragments. The solid circles and the open circles correspond to our new measurement and the data of Ref. [187] for the reaction* $^{208}Pb(500A\ MeV) + p$*, respectively. The uncertainties are shown if they exceed the size of the symbols. (a) As a function of the atomic number. (b) As a function of the mass number.*

The reactions ^{208}Pb + d at 500A MeV [28] and 1A GeV [225], and ^{208}Pb + p at 1A GeV [21] have also been considered in order to complete the investigation of the energy dependency. As can be observed in the tables, the mean values of the mass- and atomic-number distributions decrease when increasing the bombarding energy. This is expected because the reactions are more violent and the number of removed nucleons increases, leading to lighter fissioning nuclei. Conversely, the integral widths increase because of the larger excitation energy.

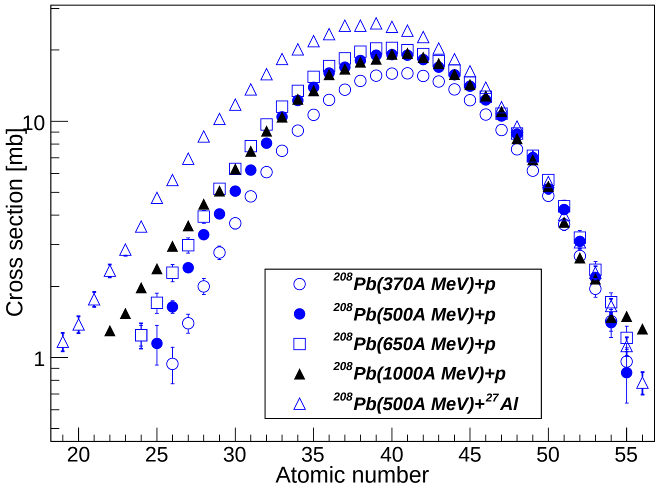

Figure 4.6: *(Color online) Cross sections of the final fission fragments for different reactions as a function of the atomic number. The uncertainties are shown if they exceed the size of the symbols.*

Table 4.1: *Mean values and integral widths of the atomic-number distributions of the final fission fragments produced in the reactions $^{208}Pb + p$, $^{nat}Pb + p$ and $^{208}Pb + d$ at different energies.*

Reaction	<Z>	σ_Z
^{208}Pb(370A MeV) + p	40.51 ± 0.30	6.11 ± 0.40
^{208}Pb(500A MeV) + p	40.05 ± 0.20	6.27 ± 0.30
^{208}Pb(650A MeV) + p	39.68 ± 0.20	6.48 ± 0.30
^{208}Pb(500A MeV) + p [187]	40.0 ± 0.1	6.3 ± 0.2
^{208}Pb(500A MeV) + p [28]	40.0 ± 0.5	6.6 ± 0.7
^{208}Pb(500A MeV) + d [28]	39.1 ± 0.5	7.0 ± 0.5
^{nat}Pb + p(600 MeV) [204]	40.0 ± 0.1	6.34 ± 0.1
^{208}Pb(1A GeV) + p [21]	39.6 ± 0.5	6.6 ± 0.3
^{208}Pb(1A GeV) + d [225]	39.0 ± 0.7	7.3 ± 0.5
^{208}Pb(500A MeV) + ^{27}Al	38.5 ± 0.20	7.05 ± 0.30

This last feature can be explained in the framework of the statistical model [145] (see section 1.2.3), where the integral width of the distributions increases with the excitation energy or temperature of the fissioning system at the saddle point, which is consistent with the evolution shown in the measurements. Therefore, we can conclude that the integral widths of the atomic- and mass-number distributions are dominated by the excitation energy of the fissioning system at saddle because the average mass and atomic-numbers of the produced fissioning systems decrease with increasing the violence of the reaction as discussed above. However, as it will be illustrated, the width of the mass distributions are strongly affected by the postscission neutron evaporation.

Table 4.2: *As Table 4.1, but for the mass-number distributions.*

Reaction	<A>	σ_A
^{208}Pb(500A MeV) + p	93.1 ± 0.5	15 ± 0.6
^{208}Pb(500A MeV) + p [187]	93.0 ± 0.4	15.1 ± 0.6
^{nat}Pb + p(600 MeV) [204]	93.2 ± 0.4	14.9 ± 0.1
^{208}Pb(1A GeV) + p [21]	90.7 ± 0.4	16.1 ± 0.8
^{208}Pb(1A GeV) + d [225]	89.6 ± 1.1	17.4 ± 1.0

4.2 Complete characterization of the final fission fragments

In this section, we will take advantage of the complete characterization of the two fission fragments achieved in this work to obtain additional information about the dynamical evolution of the fission process from correlations between the fragments and the fissioning systems. The neutron excess and width of the isotopic distribution of the final fission fragments as well as their velocities are compared to state-of-the-art model calculations that reproduce the measured observables. Correlations between the two fragments are used to assess the role of charge polarization and the excitation energy gained by the nascent fragments using the average neutron excess of the final fragments. The analysis of the average velocities of the fission fragments allows us to parametrize the distance between the two fission fragments at scission as a function of the size of the fissioning system.

4.2.1 Neutron excess

The first observable we propose to use for the characterization of the properties of the fission fragments is the neutron excess of the final fragments, defined as the average neutron number $< N >$ of a given isotopic distribution divided by its corresponding atomic number Z.

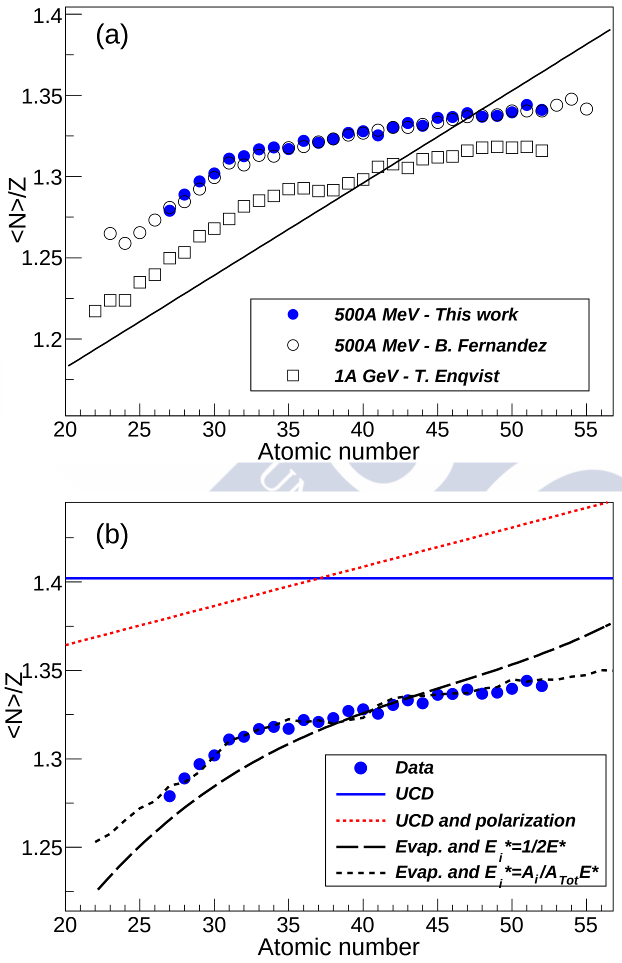

Figure 4.7: *(Color online) (a) Average neutron number over atomic number of the final fission fragments as a function of their atomic number. The solid circles and the open circles represent our new measurement and the data of Ref. [187] for the reaction* $^{208}Pb(500A\ MeV) + p$*, respectively. The open squares correspond to the reaction* $^{208}Pb(1A\ GeV) + p$ *[21]. The uncertainties are shown if they exceed the size of the symbols. The solid line indicates the valley of stability (see Ref. [21]). (b) Comparison of our measurement with different model calculations.*

The measured neutron excess of the final fission fragments (solid circles) is displayed as a function of the atomic number in Fig. 4.7(a), and also compared to previous measurements of the reaction ^{208}Pb + p at 500A MeV (open circles) [187] and at 1A GeV (open squares) [21] performed at the FRS. As can be seen in the figure, our new measurement is in excellent agreement with the previous one at 500A MeV. The comparison with the measurement at 1A GeV (open squares) [21] clearly indicates that the neutron excess of the final fission fragments decreases with the reaction energy. This fact can be understood in terms of excitation energy enhancing the evaporation of neutrons and reducing the neutron excess.

The neutron excess of the fission fragments produced in both reactions (500A MeV and 1A GeV) clearly depends on their atomic number. This dependence is attributed to the modification of the average neutron-excess of the fragments at scission with respect to the one of the fissioning system, referred to as charge polarization, but also to the excitation energy sharing between the two fragments at scission. The polarization effect is explained by the exchange of protons and neutrons between the nascent fission fragments during the descent from the saddle point to scission. The neutron excess of the fragments at scission corresponds to the one giving a maximum of the saddle-to-scission released energy. In a quasistatic approximation the charge polarization can be obtained as the neutron excess of the fragments at the scission point which minimizes the forces between the nascent fragments. According to Ref. [171], such a calculation can be done from the intrinsic binding energies and mutual Coulomb repulsion for the two nascent fragments represented by two-touching spheroids.

The partition of energy between the two fission fragments and the consequent postscission neutron evaporation also have a significant impact in the neutron excess of the final fission fragments, as can be seen in Fig. 4.7(b). For a better understanding, we compare the measured neutron excess (solid circles) with different model calculations using the code ABLA07 [160]. The solid line represents the average neutron excess of the fission fragments at the scission point calculated according to the UCD hypothesis. This estimation of the average neutron excess of the fission fragments is compared with a calculation taking into account the polarization effect (dotted line). The long- and short-dashed lines represent calculations considering the postscission neutron evaporation after a symmetric partition of excitation energy ($E_i^* = 1/2E^*$) and a partition as a function of the masses of the fission fragments at scission ($E_i^* = A_i/A_{Tot}E^*$), respectively. The difference observed between the dotted and the two dashed lines can be attributed to the postscission evaporation of neutrons. As can be seen, a symmetric partition of excitation energy describes the neutron excess for symmetric fission fragments $Z \sim 40$

(long-dashed line), but presents a deviation for the lighter and heavier fragments. On the other hand, the energy partition as a function of the mass partition describes rather well the data (short-dashed line). Therefore, we can conclude that this observable is sensitive to the charge polarization effect and to the partition of excitation energy between the two fission fragments. Indeed, the best description of the data is obtained with a statistical picture, in which the fission fragments share the available excitation energy at scission according to their masses.

Our new measurement allows us to investigate the evolution of this observable as a function of the atomic number of the fissioning system (Z_1+Z_2), which presents a strong correlation with the excitation energy gained by the fissioning system at saddle [27, 28, 137]. As can be seen in Fig. 4.8 (solid circles), the neutron excess of the final fission fragments decreases with the decrease of the atomic number of the fissioning system. This feature is expected because, according to the calculations shown in the inset of the figure, lighter fissioning nuclei are produced in more violent collisions [28] where the highly excited fission fragments evaporate more neutrons. Therefore, this observable is also sensitive to the excitation energy gained by the fissioning system.

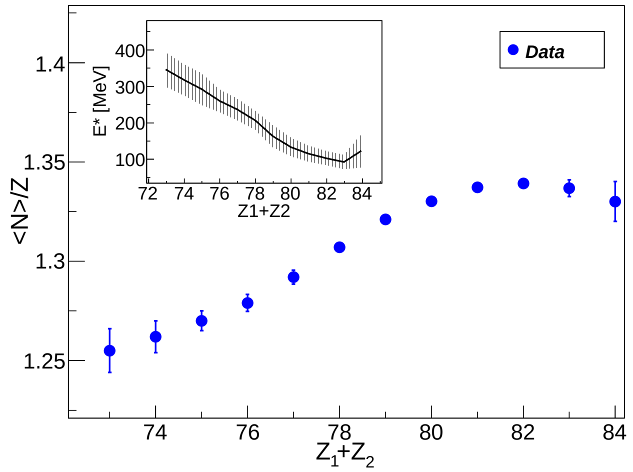

Figure 4.8: *(Color online) Final average neutron excess of the fission fragments as a function of the atomic number of the fissioning system for the reaction* $^{208}Pb(500A\ MeV)+p$. *The uncertainty bars are shown if they exceed the size of the symbols. The inset shows the excitation energy gained by the fissioning systems at the ground state as a function of their atomic number.*

4.2.2 Width of the isotopic distribution

Another interesting observable is the standard deviation of the isotopic distributions of the fission fragments. In Fig. 4.9(a) we depict the evolution of this observable as a function of the atomic number of the fission fragments (solid circles). In the figure we also compare our data with the previous measurement performed at the FRS (open circles) [187]. One can see that both measurements are in good agreement. As expected from a statistical picture [145], the widths of the isotopic distributions of the fission fragments increase with the atomic number (solid line). In the inset of Fig. 4.9(a) we represent the standard deviation of the isotopic distributions for the fission fragment Z_1 (solid circles) and Z_2 (open triangles) as a function of the atomic number of the first fragment Z_1. The widths of the second fission fragment (Z_2) are conditioned by the total atomic number of the fissioning system at saddle $Z_1 + Z_2 = 82$, assuming no-evaporation of protons beyond the scission point. From the data, we can conclude that the evolution of the widths of the isotopic distributions is symmetric as expected by atomic and mass number conservation.

In Fig. 4.9(b) the data are also compared with two model calculations using different prescriptions for the energy sharing between the two fission fragments. Again, the long- and short-dashed lines represent calculations using a symmetric partition of excitation energy and a partition as a function of the masses of the fission fragments at scission, respectively. Both calculations yield similar results and are in good agreement with the experimental data. We can then conclude that this observable is not sensitive to the partition of the excitation energy between the fission fragments at the scission point.

The difference between the measured widths and the ones calculated at the scission point (solid line) could be due to structural effects affecting the last steps of the postscission neutron evaporation. Indeed, the slope change observed between $Z = 35$ and $Z = 43$ could be attributed to the neutron shell $N = 50$. These isotopic chains cross the $N = 50$ shell. Isotopes close to this shell present larger binding energies, preventing neutron evaporation. The inset in Fig. 4.9(b) illustrates this effect displaying the difference between the maximum and minimum binding energy in the isotopic chains of the fission fragments measured in this work as a function of their atomic number. This effect reduces the widths of the isotopic distribution of the fission fragments with respect to the calculated ones at scission (solid line). To validate this interpretation, we also calculated the widths of the isotopic distribution considering a constant value of the neutron separation energy of $S_n = 12$ MeV for all the fission fragments (dotted line). One can observe that this calculation does not present large deviations with respect to the one at scission. Therefore, the slope changes observed in the widths of the isotopic distribution can only be attributed to the larger neutron separation energies for the fission fragments crossing the neutron shell $N = 50$.

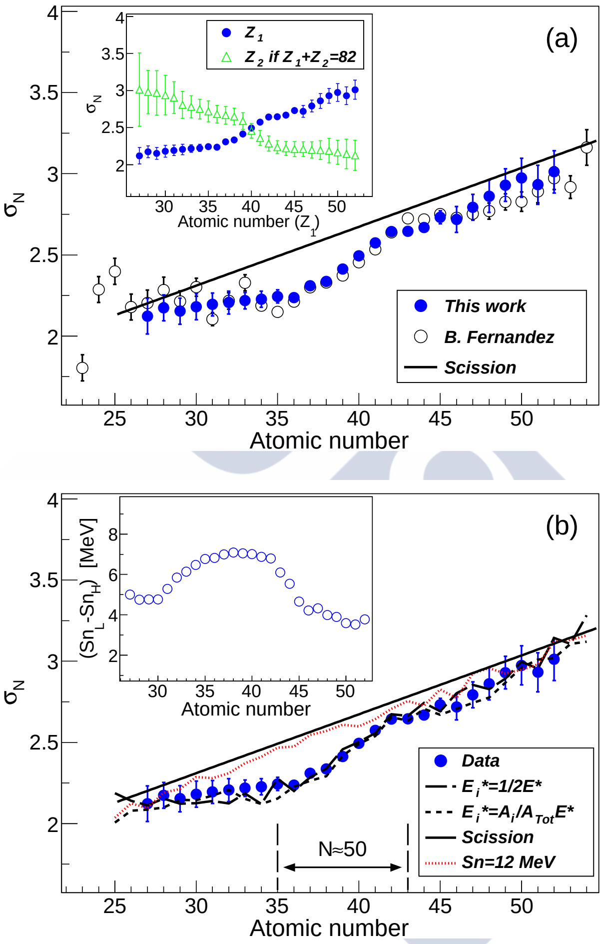

Figure 4.9: (Color online) Standard deviation of the isotopic distributions as a function of the atomic number for the reaction ^{208}*Pb(*$500A$ *MeV) + p. The error bars are given by the uncertainty of the fit and are shown if they exceed the size of the symbols. (a) The solid and open circles represent our new measurement and the data of Ref. [187], respectively. The solid line represents standard deviation of the isotopic distributions at scission. The inset shows the standard deviation of both fission fragments (*Z_1 *and* Z_2*) measured in coincidence as a function of the atomic number of the first fission fragment (*Z_1*). (b) Our data are compared with different calculations (lines). (Inset) Difference between the neutron separation energy of the lightest and the heaviest fission fragment for a given element as a function of its atomic number.*

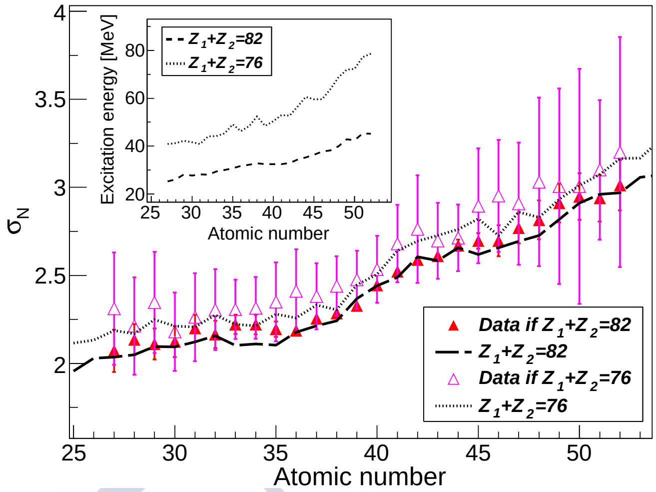

Figure 4.10: *(Color online) Standard deviation of the isotopic distributions as a function of the atomic number of the fission fragments for two fissioning systems:* $Z_1 + Z_2 = 82$ *(solid triangles) and* $Z_1 + Z_2 = 76$ *(open triangles). The lines represent ABLA07 [160] calculations for the same fissioning systems:* $Z_1+Z_2 = 82$ *(long-dashed line) and* $Z_1 + Z_2 = 76$ *(dotted line). The inset shows the calculated excitation energy of the fission fragments at scission as a function of the atomic number of the final fission fragments for the fissioning systems* $Z_1 + Z_2 = 82$ *(long-dashed line) and* $Z_1 + Z_2 = 76$ *(dotted line).*

In Fig. 4.10 we display again the evolution of the widths of the isotopic distributions as a function of the atomic number of the fission fragments, but this time for two different fissioning systems: $Z_1 + Z_2 = 82$ (solid triangles) and $Z_1+Z_2 = 76$ (open triangles). As can be seen in the figure, the widths of the isotopic distributions of the fissioning system $Z_1+Z_2 = 76$ are larger than the ones measured for the fissioning system $Z_1 + Z_2 = 82$. The data are also compared with ABLA07 [160] calculations. The calculations show similar evolutions under the same conditions. This tendency would be explained by the fact that the fissioning systems with smaller atomic number gain more excitation energy than the ones with larger values of atomic number. To validate this hypothesis, in the inset of the figure we represent the calculated mean excitation energy of the fission fragments as a function of their atomic number. One can observe that the mean excitation energy of the fissioning systems $Z_1 + Z_2 = 76$ is always larger for all atomic numbers of the fission fragments. In both cases we observe, however, similar slope changes in the evolution of the widths of the isotopic distributions as function of the corresponding atomic number. Therefore, we can conclude that this observable is sensitive to the total excitation energy gained by the fissioning system and to structural effects in the fission fragments, but not to the share of the excitation energy between the two fragments.

4.2.3 Velocities

Fission velocities provide information on the Coulomb repulsion experienced by the fission fragments at the scission point. Therefore, one could use these velocities to assess the distance between the two fission fragments formed at the scission point.

The reconstructed path length of the nuclei traversing the experimental setup together with the ToF measurements were used to obtain the velocity of the fission fragments in the laboratory frame. These velocities can then be transformed into the reference frame defined by the velocity of the incoming projectiles in the middle of the target using the corresponding Lorentz's transformation. The experimental setup allows for a precise reconstruction of the laboratory angles of the fission fragments (better than 0.4 mrad), and therefore the measurement of the velocity is performed with a good accuracy (better than 5 %) in the reference frame of the incoming projectiles.

Following the semi-statistical model of Wilkins and collaborators [172] (see Eq. 1.8), the velocity of the fission fragments can be written as:

$$V_{fiss} = \left[\frac{2e^2 Z_1 Z_2}{A_1^* \left(1 + \frac{A_1^*}{A_2^*}\right) D} \right]^{1/2} \qquad (4.2)$$

Equation 4.2 is included in the fission model of ABLA07 [160] to calculate the fission velocities of the fission fragments.

It is well known that one of parameters affecting the velocity gained by the fission fragments is the tip distance d. In the pioneering work of Wilkins and collaborators [172] it was proposed a standard tip distance $d = 2$ fm. Recent works [177] based on measurements of the total kinetic energy, using constant values for the quadrupole deformation at the scission point ($\beta_1 = \beta_2 = 0.625$), have also found a similar value for the tip distance. In other works, the authors have found that the tip distance has an upper limit around 3 fm [226, 227], where larger values are considered as invalid configurations. This upper limit is consistent with the values recently found by the authors of Ref. [228], where a dependence of the tip distance d with the Coulomb-repulsion term of the LDM was observed.

Figure 4.11 shows the velocity of the fission fragments measured for the isotopes produced in the reaction ^{208}Pb(500A MeV) + p of the present work (open circles). As can be seen in the figure, the fission velocities decrease with the atomic number of the fission fragments from 1.5 to 0.9 cm/ns, which is a natural consequence of the momentum conservation between the light and heavy fission fragment. This is clearly observed when looking at the mean velocity averaged over the isotopic yield as a function of the corresponding atomic number of the fragments, as displayed in Fig. 4.12 (open circles). In both figures, the velocities are compared to ABLA07 [160] calculations assuming a tip distance of $d = 2$ fm (solid lines). Clearly the calculations are in good agreement with the data.

In Fig. 4.12 our measurement is also compared with different calculations assuming for the tip distance the found upper limit $d = 3$ fm [226, 227] (dotted line) and $d = 1$ fm (dashed line). One can observe that these calculations provide similar results with a difference smaller than 7%. Therefore, one can conclude that the mean fission velocities of the fission fragments as a function of their atomic numbers present a limited sensitivity to the tip distance between the two fission fragments at scission. This result confirms the need of additional observables to further investigate this issue.

Equation 4.2 indicates a clear dependence of the fission velocity with the total charge of the fissioning system at scission. Therefore, in Fig. 4.13(a) we display the average fission velocities of the fission fragments as a function of the atomic number of the fissioning nucleus (solid circles). Surprisingly, the velocities do not depend very much on the size of the fissioning system. To understand this result, we compare our data with different model calculations, in particular with one using a tip distance between the fission fragments at scission of $d = 2$ fm (dotted line). As can be seen in the figure, this calculation cannot describe the evolution of the data, and shows a clear deviation for the lighter fissioning nuclei ($Z_1 + Z_2 < 78$).

To understand this discrepancy, we also compare our measurement with different calculations changing the mass and atomic numbers of the fission fragments. The calculations performed with $A - 1$ (dot-dashed line) and $A + 1$ (dot-long-dashed line) do not show any sizable difference with respect to standard ones, while the calculations supposing $Z - 1$ (double-dot-dashed line) and $Z + 1$ (long-dashed line) present offsets that can be explained with the decrease and increase of the Coulomb repulsion, respectively, but none of them provides a satisfactory description of the data. From these calculations we conclude that the discrepancy observed between the standard calculations and our data cannot be explained with simple variations of the atomic or mass number of the fission fragments at scission.

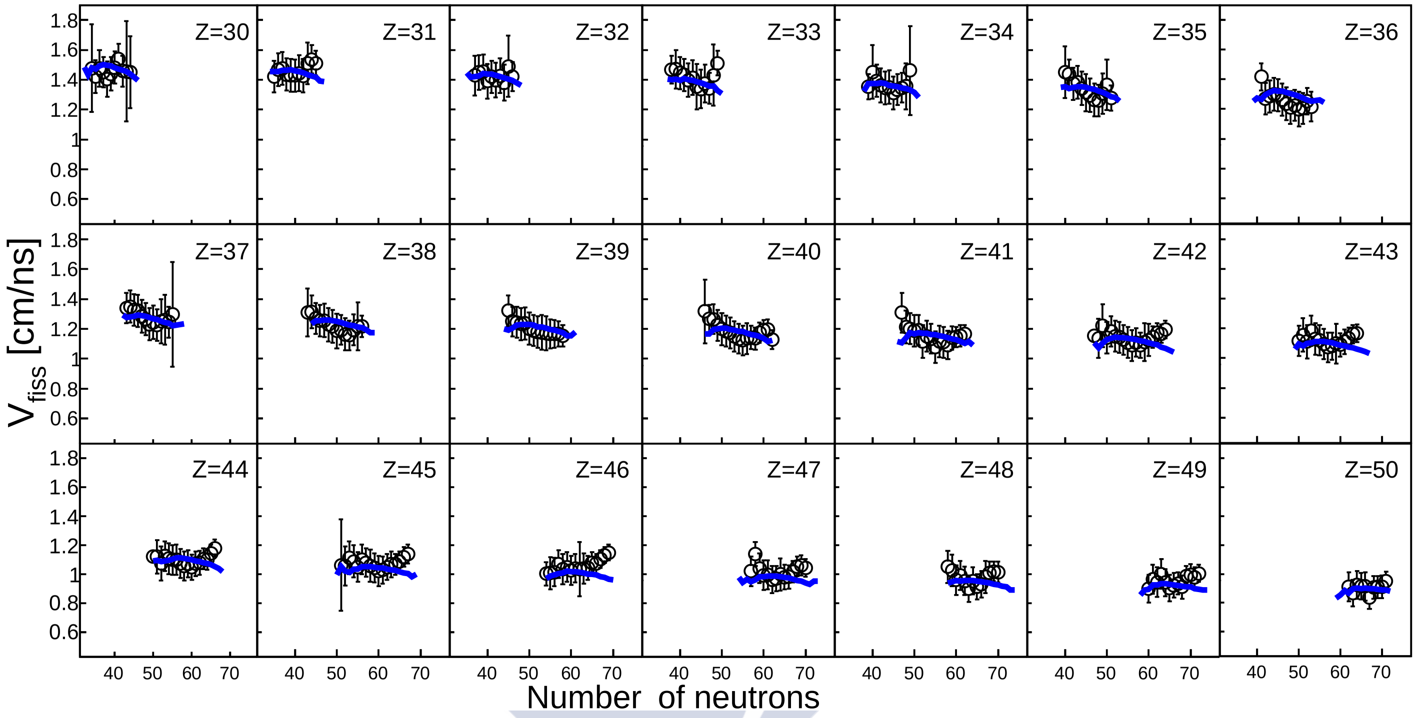

Figure 4.11: *(Color online) Mean velocity of the fission fragments as a function of the neutron number of the fission fragments for the reaction* $^{208}Pb(500A\ MeV) + p$. *The solid lines represent ABLA07 calculations.*

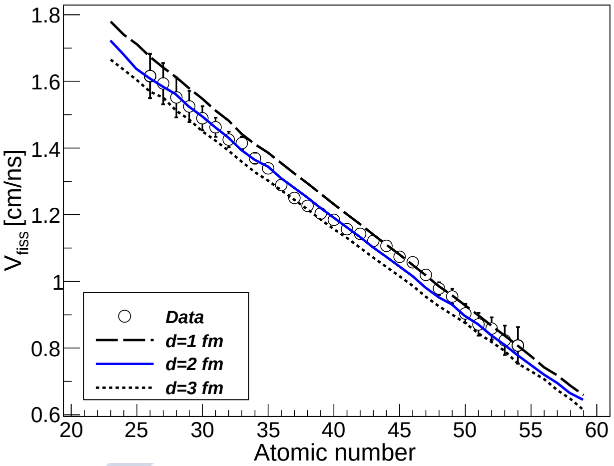

Figure 4.12: *(Color online) Mean fission velocity of the fission fragments as a function of the atomic number of the fission fragments for the reaction* $^{208}Pb(500A$ *MeV) + p. The lines represent different calculations.*

Following Ref. [228], the tip distance between the two fission fragments increases with the repulsion term $Z^2/A^{1/3}$ and then with the atomic number of the fissioning system. This fact indicates that the tip distance could increase with the atomic number of the fissioning nuclei. Based on this idea, we performed calculations using a tip distance of 1 fm to try to describe the mean fission velocities of the lower fissioning system, taking into account that calculations with $d = 2$ fm can reproduce the velocities of the heavier fissioning nuclei ($Z_1 + Z_2 \sim 82$). As can be seen in the figure, this calculation overestimates our measurement for the heaviest fissioning nuclei, but seems to be in agreement with the mean fission velocities obtained for the lightest ones. These calculations seem to point out a dependence of the tip distance with the size of the fissioning system and, thus, we implemented such a dependence in our calculations. Equation 4.3 represents the used parametrization, where d is the tip distance and Z_{fiss}^{sci} the atomic number of the fissioning system at the scission point.

$$d = -8.125 + 0.125 Z_{fiss}^{sci} \tag{4.3}$$

The result of the calculation using this parametrization is also represented in Fig. 4.13(a) (solid line), describing rather well the data.

However, the distance between the two fission fragments also depends on their quadrupole deformations (see Eq. 1.9). This issue is investigated in Fig. 4.13(b), where the data are compared with different calculations. The solid line represents a calculation using a constant quadrupole deformation of $\beta = 0.625$ for both fission fragments, while the dashed line represents the same calculation but for a constant quadrupole deformation of $\beta = 0.4$. This reduction of the deformation could also explain the increase of the average fission velocities. However, the fission fragments produced for the different fissioning systems are rather similar in size and therefore in deformation. This result is displayed in the inset of the figure, where the evolution of

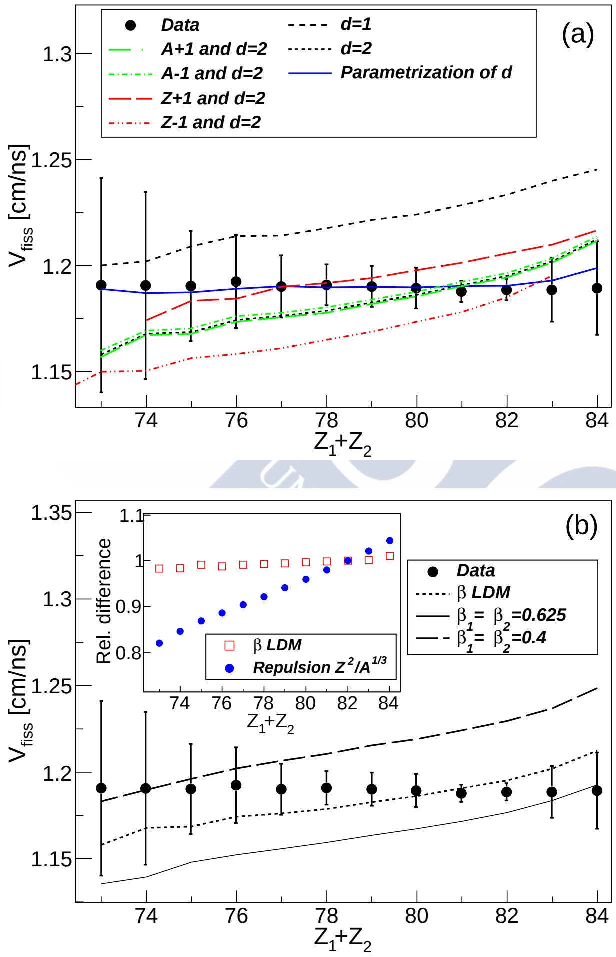

Figure 4.13: *(Color online) Mean velocity of the fission fragments in the reference frame of the fissioning system for the reaction ^{208}Pb(500A MeV) + p as a function of the atomic number of the fissioning system. (a) The lines represent different calculations changing some variables such as the atomic number, mass number, and the tip distance d. (b) The lines indicate calculations for different values of the deformation at scission point. The inset shows how the quadrupole deformation of the fission fragments and Coulomb repulsion evolve with the atomic number of the fissioning system.*

the average quadrupole deformation as predicted by the LDM for the fission fragments at scission [172] is represented relative to the value obtained for the fissioning systems $Z_1+Z_2 = 82$ and as a function of the atomic number of the fissioning system (open squares). As can be seen, the difference in per cent between the mean deformations as function of $Z_1 + Z_2$ is below 2%. In the same inset, we also display the evolution of the average Coulomb-repulsion term $Z^2/A^{1/3}$ of the fissioning systems (solid circles), which changes a factor around 20% between $Z_1 + Z_2 = 82$ and $Z_1 + Z_2 = 73$. This fact, together with the negligible change on quadrupole deformation, favors the idea of a variation of the tip distance with the atomic number of the fissioning system. Therefore, we can conclude that a change of the distance between the two fission fragments is needed to explain the evolution of the average fission velocities as a function of the size of the fissioning system.

4.3 Pre- and postscission neutron multiplicities

In order to study postsaddle fission dynamics, first one needs to differentiate between the neutrons emitted by the two fission fragments and the neutrons emitted by the fissioning system before scission, the so-called post- and prescission neutron multiplicities (see section 1.2.2). In this experiment the separation of these two contributions was possible by correlating the measured velocities and atomic numbers of the two fission fragments according to the Wilkins model [172] (see Eqs. 1.8 and 4.2). Taking into account momentum conservation of the fission fragments at scission:

$$A_2^* = \frac{A_1^* V_1}{V_2} \tag{4.4}$$

where A_1^* and A_2^* represent the masses of the two fission fragments at scission, equation 4.2 can be rewritten as:

$$A_1^* \left(r_o A_1^{*1/3} \left[1 + \frac{2}{3}\beta_1 + \frac{V_1^{1/3}}{V_2^{1/3}} \left(1 + \frac{2}{3}\beta_2 \right) \right] + d \right) - \frac{2 Z_1 Z_2}{V_1^2 (1 + V_2/V_1)} = 0 \tag{4.5}$$

where V_1 and V_2 are the velocities of the fission fragments in the reference frame of the incoming projectiles. Knowing the atomic number of the two fission fragments and their final velocities, this equation can be used to reconstruct the mass of the fission fragment at scission, although it is necessary to assume that the velocities of the fission fragments are not affected by the postscission neutron evaporation and that the quadrupole deformations at scission can be estimated with the LDM. For a given atomic and mass number of the final fission fragments it is assumed that $\beta_i(A_i^*, Z_i^*) \sim \beta_i(A_i, Z_i)$. However, equation 4.5 has no analytical solution, and therefore, for determining the mass number at scission (A_1^*) equation 4.5 is evaluated for all the possible values of A_1^* and its minimum is assumed to be the solution. Finally, the mass number of the second fission fragment at scission can be obtained by momentum conservation (see Eq. 4.4).

Thus, the number of neutrons evaporated after scission for each fission fragment (ν_{post}) can be deduced as:

$$\nu_{post,1} = A_1^* - A_1^{Final} \quad and \quad \nu_{post,2} = A_2^* - A_2^{Final} \tag{4.6}$$

where $A_{1,2}^{Final}$ are the measured masses.

In addition, the total number of emitted neutrons (ν_{Tot}) can be calculated as:

$$\nu_{Tot} = A_{proj} - Z_{proj} - (A_1^{Final} + A_2^{Final} - Z_1^{Final} - Z_2^{Final}) \tag{4.7}$$

with A_{proj} and Z_{proj} as the mass and the atomic number of the projectile. Note that the total number of emitted neutrons includes the neutrons emitted in the intranuclear cascade stage. However the results from this equation are only valid if the emission of other particles like d, t, ... is negligible.

Finally, the prescission neutron multiplicities (ν_{pre}) can be deduced using the difference between the previous neutron multiplicities as:

$$\nu_{pre} = \nu_{Tot} - \nu_{post,1} - \nu_{post,2} \tag{4.8}$$

The resulting neutron multiplicities are displayed in Fig. 4.14 as a function of the atomic number of the fissioning system. The postscission neutron multiplicities (open squares) were reconstructed for the full range of fissioning systems while the total and the prescission neutron multiplicities (open triangles and solid circles respectively) were only obtained for fissioning systems with $Z_1 + Z_2 > 77$ due to the fact that emission of other particles such as d, t, ... is not negligible for lighter fissioning systems.

As can be seen in Fig. 4.14, the neutron multiplicities increase for decreasing atomic numbers of the fissioning nuclei. This tendency is expected because the neutron emission increases with the excitation energy. The uncertainties of the total number of neutron are attributed to the uncertainty of the mass numbers of the fission fragments and the emission of other particles like deuterium and tritium during the cascade stage which could lead to a decrease of the neutron multiplicities. The latter was evaluated with the code INCL4.6 [159]. The uncertainties associated with the post- and prescission multiplicities are attributed to the velocity uncertainties of the fission fragments and to the uncertainties of the total number of emitted neutrons.

In the same figure, we compare the data with the systematics proposed by Hilscher and Rossner [3]. This systematics was found by investigating measured neutron multiplicities from fusion-fission reactions of different nuclei at excitation energies from 6 to 200 MeV. According to this work the pre- and postscission neutron multiplicities, dotted and dashed lines respectively, can be parameterized as a function of the total number of evaporated neutrons as:

$$\nu_{pre} = 0.8(\nu_{Tot} - \nu_o) \quad and \quad \nu_{post} = \nu_o + 0.2(\nu_{Tot} - \nu_o) \tag{4.9}$$

where ν_o is an offset that depends on the atomic number of the fissioning system. In the present work this parameter was set to 2.5, according to Ref. [3]. As can be observed, the systematics is in excellent agreement with the data.

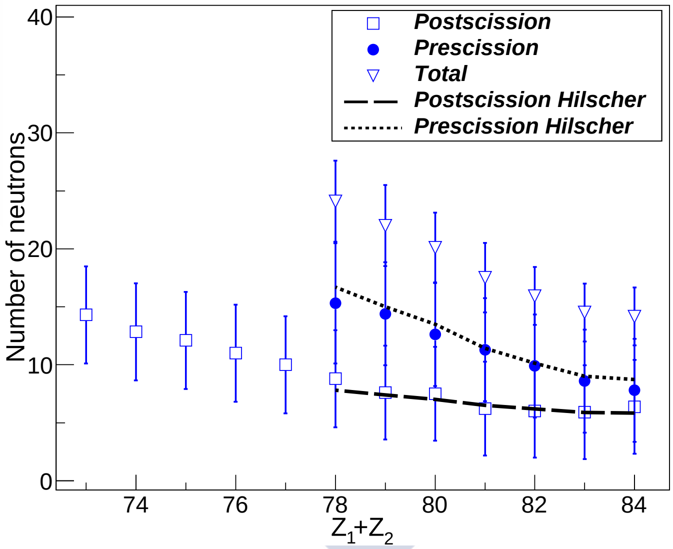

Figure 4.14: *(Color online) Average total and pre- and postscission neutron multiplicities (open triangles, solid circles and open squares respectively) as a function of the atomic number of the fissioning system. The data are compared with the predictions of Hilscher's systematics (lines).*

4.4 Postsaddle dissipation effects

In chapter 3 we have studied the dissipative effects in fission at small deformations between the ground-state and saddle-point configurations. However, dissipation also affects the descend time from the saddle to the scission point.

For this reason one of the fundamental questions about the dissipation parameter is its dependence on deformation, which has been investigated in other works using pre- and postscission neutron multiplicities obtained from fusion-fission reactions [3, 132, 229]. However, in this kind of reaction the compound nuclei are produced with large angular momentum values that could complicate the interpretation of the data.

In this section we investigate the pre- and postscission neutron multiplicities using spallation reactions, where the compound nuclei are produced with low angular momentum as discussed in previous sections. Moreover, the present data allow us to define a new observable, the neutron excess of the final fission fragments as a function of the size of the fissioning system, which is sensitive to dissipation at large deformations. This new observable is used to constrain the value of the dissipation parameter beyond the saddle-point configuration.

4.4.1 Model calculations

In order to include the fission dynamics beyond the saddle point in our calculations, the saddle-to-scission time, needed by the fissioning system to descend from the saddle to the scission point, can be compared with the statistical evaporation time obtained from the neutron decay width. If the saddle-to-scission time of the fissioning system is longer than the statistical evaporation time, the fissioning system could emit neutrons during that phase, increasing the prescission neutron multiplicities. With the aim of introducing these dynamical effects in our calculations, we have used the pioneering model proposed by Hofmann and Nix [121], who found an analytical solution of the average saddle-to-scission time based on the dynamical picture of Kramers [79]. Following this formalism, the average saddle-to-scission dissipative time (τ_{ssc}) can be calculated according to:

$$\tau_{ssc} = \left(\left[1 + \left(\frac{\beta}{2\omega_0} \right)^2 \right]^{1/2} + \frac{\beta}{2\omega_0} \right) \tau_{ssc}^0 \tag{4.10}$$

where ω_0 is the frecuency of the inverted oscillator potencial at the saddle point, β is the reduced dissipation parameter, and τ_{ssc}^0 is the saddle-to-scission statistical time.

This average saddle-to-scission statistical time (τ_{ssc}^0) can be described as:

$$\tau_{ssc}^0 = \frac{2}{\omega_0} R \left(\left[\frac{\Delta V}{T_{sd}} \right]^{1/2} \right) \tag{4.11}$$

where T_{sd} is the temperature of the fissioning system at the saddle point, and $R(z)$ is a function introduced by Rosser [230]:

$$R(z) = \int_0^z e^{y^2} dy \int_y^\infty e^{-x^2} dx = 0.49 + \frac{1}{2} ln(z) + \frac{1}{8z^2} + O^4 \tag{4.12}$$

The potential energy difference (ΔV) between the saddle and scission points can be obtained by approximating the potential shape around the saddle point by an inverted oscillator of frecuency ω_0:

$$\Delta V = \frac{1}{2} M \omega_o^2 X'^2 \tag{4.13}$$

where M is the mass inertia of the fissioning system and X' represents the deformation of the fissioning system at the scission point with respect to that at the saddle point.

The mass inertia can be calculated by assuming an irrotational and incompressible flow for the fissioning system as suggest by Lestone [231]:

$$M = \frac{A_{fiss}}{4} \left(1 + \frac{17}{15} exp \left[-\frac{128}{51} \left(\frac{r}{R_o} - \frac{3}{4} \right) \right] \right) \tag{4.14}$$

where A_{fiss} is the mass of the fissioning system and r/R_o represents the deformation of the fissioning nucleus according to the LDM in terms of its quadrupole deformation at the saddle point β_{sd}^{fiss}:

$$\frac{r}{R_o} = 1 + \frac{2}{3} \beta_{sd}^{fiss} \tag{4.15}$$

The difference between the deformation of the fissioning system at the saddle point and at the scission point can be determined according to the difference of the scission-point (X_{sc}) and saddle-point (X_{sd}) deformations as:

$$X' = X_{sc} - X_{sd} \tag{4.16}$$

where X_{sc} can be calculated as the distance between the two uniformly-charged spheroids representing the fission fragments at scission, parametrized according to equation 1.9.

The deformation of the fissioning system at the saddle point (X_{sd}) can be determined as a function of its quadrupole deformation by assuming again a uniformly-charged spheroid according to:

$$X_{sd} = r_o A^{1/3} \left(1 + \frac{2}{3} \beta_{sd}^{fiss}\right) \tag{4.17}$$

The results of the comparison of the evaporation statistical time with the saddle-to-scission time are presented in Fig. 4.15. The dot-short-dashed line represents the evaporation statistical time with its width (shaded area) as a function of the atomic number of the fissioning system. This time was calculated as the inverse of the neutron evaporation decay width. We can observe that the saddle-to-scission statistical times (long-dashed line), calculated according to equation 4.11, are below the evaporation statistical times, except for the lightest fissioning systems where both calculations show a small overlap. This overlap increases with the value of the dissipation parameter, as shown by the solid line ($\beta = 6.5 \times 10^{21}$ s^{-1}) and the dot-long-dashed line ($\beta = 18 \times 10^{21}$ s^{-1}). Therefore, these longer saddle-to-scission times increase the probability of evaporating neutrons, leading then to larger prescission neutron multiplicities.

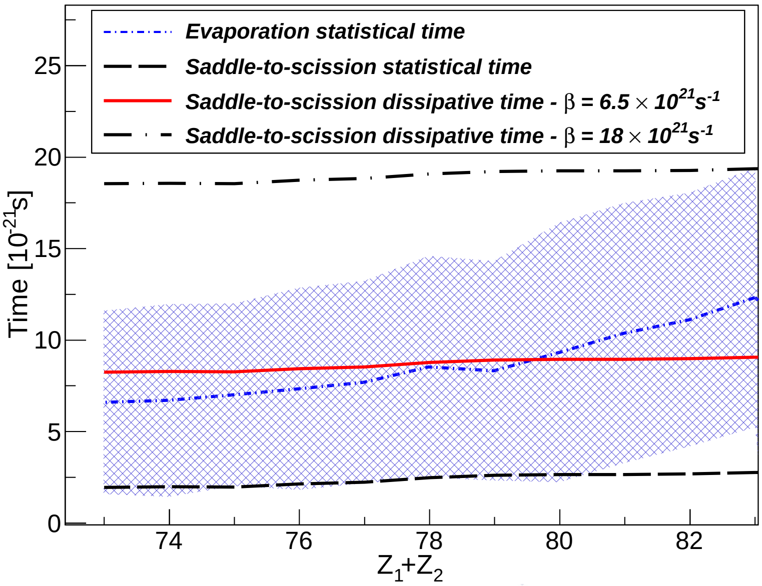

Figure 4.15: (Color online) The evaporation statistical time (dot-short-dashed line) and the saddle-to-scission statistical (long-dashed line) and dissipative times, for different values of the dissipation parameter $\beta = 6.5 \times 10^{21}$ s^{-1} (solid line) and $\beta = 18 \times 10^{21}$ s^{-1} (dot-long-dashed line), are displayed as a function of the atomic number of the fissioning system.

4.4.2 Results and discussion

For investigating the dissipative effects between the saddle-point and the scission-point configurations, the pre- and postscission neutron multiplicities as a function of the atomic number of the fissioning system (see section 4.3) are compared with several different calculations assuming no evaporation of particles between the saddle and scission points (dotted lines), calculations based on the saddle-to-scission statistical time τ^0_{ssc}, deduced according to equation 4.11 (long-dashed line), and assuming dissipation according to equation 4.10 with a dissipation parameter $\beta = 18 \times 10^{21}$ s^{-1} (dot-long-dashed line), as shown in Fig. 4.16. The latter calculation is displayed to show the sensitivity of these observables to dissipative effects.

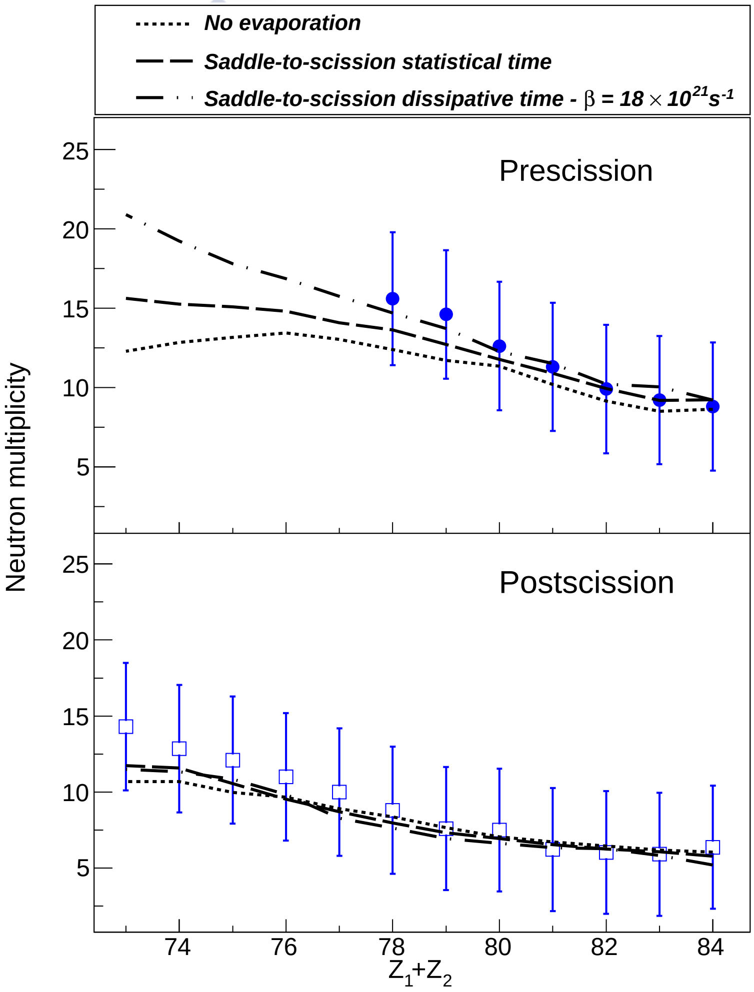

Figure 4.16: (Color online) The data of Fig. 4.14 are compared with different model calculations (lines). The upper and lower panels correspond to the prescission and postscission neutron multiplicities, respectively.

From comparison of the neutron multiplicities with our calculations, one can see that as expected the saddle-to-scission dissipative effects affect only the prescission neutron multiplicities while the calculations for the postscission neutron multiplicities seem to be very similar for all the fissioning systems. The latter result indicates that the separation between pre- and postscission neutron multiplicities presented in section 4.3 is correct. However, the uncertainties in the prescission multiplicities prevent us an accurate determination of the value for the saddle-to-scission dissipation parameter. On another hand, the neutron excess of the two final fission fragments could be as sensitive to dissipation at large deformation as the prescission neutron multiplicities. Moreover, in our experiment the measurement of the neutron excess of the final fission fragments is more accurate than the prescission neutron multiplicities because is a direct measurement, which should result in an accurate constraint of the dissipation parameter. Therefore, in this work, we propose using this observable as a function of the atomic number of the fissioning system. As shown in section 4.2.1, the neutron excess as a function of the atomic number of the fission fragments provides important information on the partition of the excitation energy between the two fission fragments at scission, however, as a function of the atomic number of the fissioning system, this observable should help us to obtain information on the saddle-to-scission dynamics.

The average neutron excess of the fission fragments is displayed as a function of the atomic number of the fissioning nuclei in Fig. 4.17 for the reaction ^{208}Pb + p at 500A MeV. In the figure, we also compare the neutron excess with our previous model calculations. First, the average neutron excess is compared with a calculation assuming the saddle-to-scission statistical time according to equation 4.11 (long-dashed line). As can be observed, this calculation clearly overestimates the neutron excess for the lightest fissioning systems. This overestimation indicates the need for dissipation at high excitation energies where the statistical evaporation time is comparable to the time needed by the fissioning nucleus to descend from the saddle point to scission. Therefore, we also compare the data with dissipative calculations based on equation 4.10, assuming a reduced dissipation parameter $\beta_{saddle-scission}$ of 4.5×10^{21} s^{-1} (short-dashed line), 6.5×10^{21} s^{-1} (solid line), and 18×10^{21} (dot-long-dashed line) s^{-1}. As can be seen in the figure, the calculation considering a reduced dissipation parameter of 4.5×10^{21} s^{-1} (short-dashed line) or 6.5×10^{21} s^{-1} (solid line) can describe the average neutron excess for all the fissioning systems. These results could indicate that the dissipation parameter does not depend on deformation because we determined a dissipation parameter of $(4.5 \pm 1.0) \times 10^{21}$ s^{-1} at small deformations (see chapter 3).

Our results seem to be in agreement with the values recently found by Nadotchy and co-workers [232]. They compared neutron and light-charged particle multiplicities of excited compound nuclei from ytterbium to rutherfordium, produced in fusion-fission reactions, with four-dimensional Langevin calculations by assuming the one-body dissipation mechanism and the chaos-weighted wall formula. From their calculations they estimated a value for the reduced dissipation parameter $\beta_{saddle-scission}$ to be between 4 and 8 $\times$ 10^{21} s^{-1}, which seems to be in excellent agreement with our results.

On the other hand, our results seem to contradict most of the works performed with fusion-fission reactions [131, 132, 133, 142, 233, 234], where a deformation-dependent dissipation parameter was claimed to describe the prescission particle multiplicities. Although, as already mentioned, that conclusion could be affected by the initial conditions of the fusion-fission reactions and by the fact that several independent observables are needed for constraining the dissipation parameter accurately.

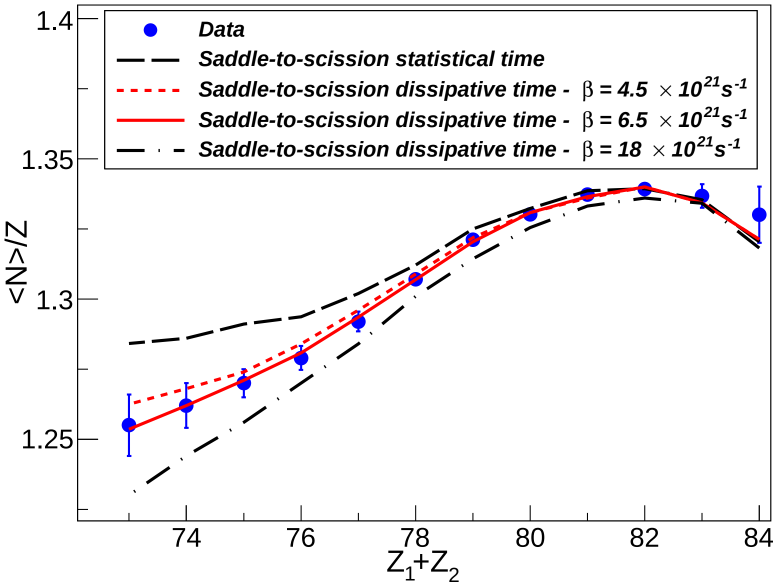

Figure 4.17: *(Color online) The average neutron excess of the final fission fragments produced in the reaction* $^{208}Pb + p$ *at 500A MeV (solid circles) is compared to different model calculations (lines).*

4.5 Conclusions

In the present chapter, we have investigated the reactions ^{208}Pb(370A, 500A, and 650A MeV) + p and ^{208}Pb(500A MeV) + ^{27}Al measured in inverse kinematics using a highly efficient detection setup. Further, this setup allowed us for the first time a complete isotopic and kinematic identification of the two fission fragments produced in proton-induced fission of ^{208}Pb at 500A MeV.

The atomic-number distributions of the fission fragments were obtained from energy loss measurements in a double multisampling ionization chamber (Twin MUSIC) with a resolution below 0.43 charge units (FWHM), while the mass numbers were obtained from the mass-over-charge ratio (A/Z) determined from magnetic rigidity and time-of-flight measurements with a resolution of 40 ps (FWHM). These measurements provided a complete isotopic distribution of fission fragments from cobalt to tellurium with an average mass-number resolution of $\Delta A \sim 0.6$ mass units (FWHM).

The isotopic distribution of the fission fragments produced in the reaction ^{208}Pb(500A MeV) + p was used to validate previous controversial measurements of the same isotopic distribution and to study its properties, such as the mean neutron excess and the widths of the distributions, but also the velocities of the final fission fragments.

Moreover, our measurement allowed us to investigate the mass and charge correlations between the two fission fragments. We investigated the average neutron excess and the width of the isotopic distributions of the fission fragments as a function of their atomic number. Different model calculations of the neutron excess indicate that this observable is sensitive to the polarization effect, the postscission neutron evaporation, and the partition of the excitation energy between the two fission fragments at scission. Our calculations helped us to conclude that a partition of the excitation energy as a function of the masses of the fission fragments provides a better description of the data. We also observe that the neutron excess of the fission fragments decreases with decreasing the atomic number of the fissioning system. This fact can be explained by an increase of the excitation energy for the lighter fissioning systems at the saddle point [27, 28, 137].

On the other hand, we show that the widths of the isotopic distributions are sensitive to the total excitation energy gained by the fissioning system and to structural effects in the deexcitation of fission fragments crossing the neutron shell at $N = 50$. The slope changes observed in the widths of the isotopic distribution can only be explained by the larger neutron separation energies for the fission fragments crossing the neutron shell $N = 50$.

In addition, our data are used to investigate the velocities of the fission fragments at the scission point as a function of the atomic number of the fissioning system. The comparison with different model calculations for the fissioning nuclei investigated in this work allows us to conclude that the velocities of the fragments as a function of the size of the fissioning nuclei are more sensitive to the tip distance between the fission fragments than to their quadrupole deformations. Finally, we have parametrized the value of the tip distance as a function of the size of the fissioning nuclei.

Finally, the complete kinematics measurement of the fission fragments produced in the reaction ^{208}Pb(500A MeV) + p was used to reconstruct the average prescission and postscission neutron multiplicities. These observables, together with the average neutron excess of the final fission fragments, were displayed as a function of the atomic number of the fissioning nucleus to investigate dissipative effects at large deformations. The comparison of several model calculations with these two independent observables shows that both observables are sensitive to dissipation, although the neutron excess has a higher accuracy, allowing us to determine the value of the dissipation parameter at large deformations. From our calculations, we deduce a value of the reduced dissipation parameter $\beta_{saddle-scission}$ of $(6.5 \pm 2.5) \times 10^{21}$ s^{-1}. Taking its uncertainty into account, this value is in agreement with the value of the reduced dissipation parameter obtained at small deformations $(4.5 \pm 1.0) \times 10^{21}$ s^{-1} (see chapter 3) and therefore we conclude that no dependence on deformation is observed.


USC
UNIVERSIDADE
DE SANTIAGO
DE COMPOSTELA

Conclusions and future perspectives

In the present work, the reactions proton-induced fission of ^{208}Pb at 370A, 500A, and 650A MeV and ^{208}Pb + ^{27}Al at 500A MeV have been investigated in inverse kinematics using a highly efficient detection setup that permitted us to measure and identify the two fission fragments in terms of their mass and atomic numbers. We have obtained the fission cross sections, partial fission cross sections, the width of the charge distributions of the fission fragments as well as multiplicities of the light-charged particles from H to Li for all the reactions with high efficiency and precision. Moreover, the isotopic distributions and the velocities of the two fission fragments were measured for the reaction proton-induced fission of ^{208}Pb at 500A MeV.

The atomic-number distributions of the fission fragments were obtained from energy-loss measurements by using a double multisampling ionization chamber (Twin MUSIC) with a resolution below 0.43 charge units (FWHM), while the mass numbers were obtained from the mass-over-charge ratio (A/Z) determined from magnetic rigidity and time-of-flight measurements with a resolution of 40 ps (FWHM). These measurements provided the complete isotopic distribution of fission fragments from cobalt to tellurium with an average mass-number resolution of $\Delta A \sim 0.6$ mass units (FWHM).

The total fission cross sections allowed us to clarify the existing discrepancies in previous measurements at intermediate and high energies. This set of data also allows us to revisit the previously-established systematics by Prokofiev [12] and to propose new values for the parameterization of proton-induced fission cross sections of ^{208}Pb. Moreover, these data were used to benchmark model calculations, performed with the intranuclear cascade code, INCL4.6 [159], coupled to the deexcitation code ABLA07 [160]. The large range covered by these data in terms of excitation energy allowed to investigate dissipative and transient effects in fission. Calculations including dissipative but not transient effects are able to describe the measured cross sections up to a proton energy around 200 MeV. At higher excitation energies, only calculations that include a time-dependent description of the fission decay width describe the data correctly. These results confirm previous works, pointing to a unique value of the reduced dissipation parameter around $\beta = 4.5 \times 10^{21}$ s^{-1}, as well as to a temperature independence of this parameter. In addition, one can confirm that the onset of transient effects occurs at excitation energies around 110 MeV [8, 135, 137, 138, 146].

The measurement of the light-charged particles in coincide with the fission fragments has also been used to investigate dissipative and transient time effects. The comparison of the data with different model calculations shows that the average multiplicity of the emitted particles with $Z = 1$, and the ratio (fission/evaporation) of the particle yields, are also sensitive to dissipative effects. Moreover, these data also permitted us to study the evolution of the width of the charge distribution of the fission fragments as a function of the particle removed from the projectile for different entrance channels and bombarding energies. This comparison shows that the width of the charge distribution depends on the removed particle. However, the width depends on neither the entrance channel nor on the bombarding energy. In addition, the comparison with different model calculations indicates that this observable is also sensitive to dissipative effects.

The total fission cross sections, partial fission cross sections, and the width of the charge distribution of the fission fragments were also used to investigate the role of the level-density parameter in fission. The comparison of these observables with calculations based on different descriptions for this parameter demonstrate that the parameterization proposed by Ignatyuk et al. [105] together with a dissipative model provide a better description of the data, although statistical model calculations based on the Bohr and Wheeler approach, together with a modified level-density parameter, are also able to describe the observables separately.

In addition, the isotopic distribution of the fission fragments was used to validate previous controversial measurements of the same isotopic distribution and to study its properties, such as the mean neutron excess and the widths of the distributions. We investigated the evolution of the average neutron excess and the width of the isotopic distributions of the final fission fragments as a function of the atomic number of the fissioning nuclei. Different model calculations of the neutron excess indicate that this observable is sensitive to the polarization effect, the postscission neutron evaporation, and the sharing of the excitation energy between the two fission fragments at scission. Our calculations helped us to conclude that a sharing of excitation energy as a function of the masses of the fission fragments provides a better description of the data. We also observe that the neutron excess of the fission fragments decreases with decreasing the atomic number of the fissioning system. This fact can be explained by an increase of the excitation energy for the lighter fissioning systems at the saddle point [27, 28, 137].

On the other hand, we show that the widths of the isotopic distributions are sensitive to the total excitation energy gained by the fissioning system and to structural effects in the deexcitation of fission fragments crossing the neutron shell at $N = 50$. The slope changes observed in the widths of the isotopic distribution can only be explained by the larger neutron separation energies for the fission fragments crossing this shell.

Our data were also used to investigate the velocities of the fission fragments at the scission point as a function of the atomic number of the fissioning system. The comparison with different model calculations for the fissioning nuclei investigated in this work, allowed us to conclude that the velocities of the fragments as a function of the size of the fissioning nuclei are more sensitive to the tip distance between the fission fragments than to their quadrupole deformations. Finally, the value of the tip distance was parametrized as a function of the size of the fissioning nuclei.

The velocities and atomic numbers of the two fission fragments were used to reconstruct the postscission neutron multiplicities using an indirect method based on the Wilkins model [172]. The total neutron multiplicities were also deduced by using the difference between the neutron number of the projectile and the neutron numbers of the two final fission fragments, while the prescision neutron multiplicities were deduced using the total and the postscission neutron multiplicities. These data were compared with different calculations based on the formalism proposed by Hofmann and Nix [121] to describe the dynamics of the evolution from the saddle point to the scission configuration. The comparison shows that the neutron multiplicities are more sensitive to dissipative effects at high excitation energies, where the statistical evaporation time is comparable to the time needed by the fissioning nucleus to descend from the saddle to the scission point. Moreover, our calculations indicate that the postscission neutron multiplicities are less sensitive to the saddle-to-scission dynamics, which allows us to define the neutron excess of the final fission fragments as a new observable directly related to the evaporation of neutrons between the saddle and the scission points. This fact permitted us to study dissipative effects at large deformations as a function of the size of the fissioning nuclei by using their atomic numbers. From the comparison of the data with calculations we have constrained the value of the dissipation parameter at large deformations, obtaining a value of $(6.5 \pm 2.5) \times 10^{21}$ s^{-1}. Taking the uncertainty into account, this result is consistent with the value obtained at small deformations, suggesting a deformation independence of this parameter.

Our understanding of fission could be further improved by better constraining the initial stage of the reaction. Therefore, in these conclusions we also propose to investigate the fission process by using $(p, 2p)$ reactions. This type of measurements have also been proposed by Henning at RIKEN [235]. The key feature of such studies is that $(p, 2p)$ reactions allow one for the determination of the excitation energy gained by the compound nucleus from the kinematics of the two protons, providing a better control of a key parameter of the fission process. This fact could be used to constrain model calculations and to study how fission yields depend on temperature, because these reactions allow us to cover a large range in level densities and excitation energies, ranging from the fission barriers up to ∼60 MeV, for a given fissioning system.

With the aim of investigating fission using $(p, 2p)$ reactions, the detector CALIFA (CALorimeter for In-Flight emitted pArticles) [236, 237, 238], currently being built by the R3B collaboration [239], could be coupled to the current SOFIA setup as shown in Fig 5.1. Furthermore, the NeuLand detector [240, 241] could be used to measure the neutron multiplicities, which should help us to investigate the sharing of excitation energy between the two fission fragments. Because of the low fission cross sections in $(p, 2p)$ reactions (1-10 mb) only the charge distributions of the fission fragments could be measured with good statistics. However, this would be sufficient to investigate the interesting structural effects in fission [20, 220, 221].

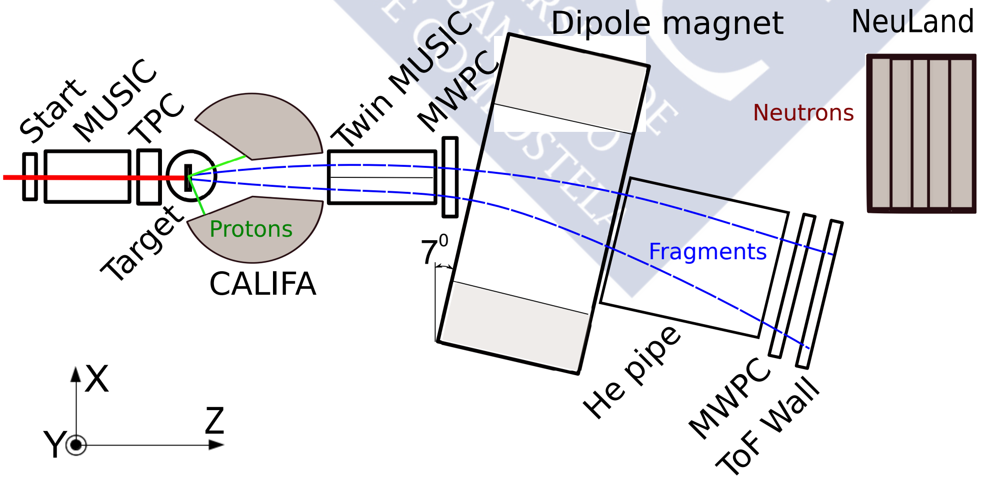

__Figure 5.1:__ (Color online) An example of the possible setup to measure fission induced by (p,2p) reactions. The two protons are detected with the CALIFA detector while the fission fragments are measured with the SOFIA setup. The detector NeuLand could be also included to measure neutron multiplicities. Sizes are not to scale.

CALIFA has two major parts as shown in Fig. 5.2 (left pad): the Barrel covering an angle between 43°and 140°and the forward EndCap covering an angle between 7°and 43°, which allows for a small angular aperture of 7°to transmit the fission fragments. The large angular acceptance together with a high granularity (∼ 3400 individual crystals) allow to measure the two protons emerging from a $(p, 2p)$ reaction with a high geometrical efficiency. The intrinsic efficiency depends on the length of the crystal: 23 cm for crystals in the Barrel and 40 cm for those in the EndCap.

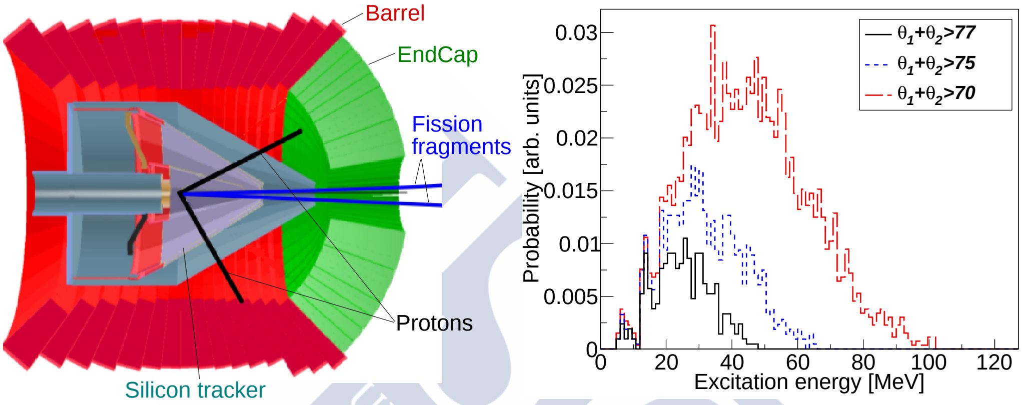

Figure 5.2: *(Color online) Left pad: Display of a reaction (p,2p) measured with the CALIFA detector. Right pad: Excitation energy of the compound nuclei reconstructed from the kinematics of the two protons measured with CALIFA. The distributions are shown for different selections of the sum of the polar angles ($\theta_1+\theta_2$).*

Several experimental tests and simulations with protons and ions at 500A MeV demonstrated that prompt protons emitted in the forward direction with large kinetic energies (∼ 420 MeV) can be detected by the EndCap with an intrinsic efficiency around 50% [238], while slow protons (∼ 80 MeV) could be detected by the Barrel with an efficiency of about 75% [243, 244]. The angles of the two protons can be determined by using a combination of the positions measured with a silicon tracker [245] and CALIFA. Both measurements of kinetic energy and position allow to reconstruct the excitation energy with a resolution of 5-8 MeV (FWHM) [238], using the invariant mass of the reaction. An example of this excitation energy reconstruction is shown in Fig. 5.2 (right pad), where we display the excitation energy distribution for different selections of the sum of the polar angles ($\theta_1+\theta_2$). These calculations were done with INCL4.6+ABLA07 [159, 160] for proton-induced fission of ^{238}U at 500A MeV, assuming that the atomic number of the fissioning nuclei is $(Z_1 + Z_2) = 91$, which ensures that no proton was emitted during the deexcitation stage. This reaction was chosen because it represents a good compromise among fission cross section, detection efficiency, and excitation energies that we want to investigate.

Resumen en castellano

Introducción

Desde que Hahn, Strassmann y Meitner descubrieron la fisión en 1939 [1] un gran esfuerzo ha sido hecho para entender este mecanismo. Una de las primeras interpretaciones teóricas fue dada por Bohr y Wheeler [2] basandose en un modelo puramente estatístico, donde la probabilidad de los canales de desexcitación esta dada por la densidad de niveles de energía en el espacio de fases. Años más tarde el análisis de diferentes observables experimentales, tales como la emision de partículas cargadas, neutrones, rayos γ y secciones eficaces de fisión y de residuos de evaporación, mostró que esa interpretación estatística no era suficiente. Las discrepancias encontradas entre el modelo estadístico y los datos experimentales fueron atribuidas al hecho de que el proceso de desexcitación no ocurre espontáneamente como se asume en el modelo puramente estadístico, sino que necesita un tiempo extra para encontrar el equilibrio termodinámico. Es decir, el proceso necesita una descripción dinámica. En este sentido existen algunas teorías microscópicas, sin embargo, el gran número de grados de libertad que intervienen en el proceso hace que estos modelos sean muy complejos requiriendo largos períodos de cálculo. Por este motivo los modelos más usados en la actualidad consisten en ecuaciones de transporte, es decir, teorías donde se describe el proceso de fisión usando un número pequeño de variables lo cual reduce consideradamente los tiempos de cálculo. En estos modelos, los grados de libertad se dividen en dos grupos, intrínsecos y colectivos. Los grados de libertad intrínsecos se corresponden con los estados individuales de los nucleones y los grados de libertad colectivos se asocian a movimientos combinados de varios nucleones, como por ejemplo estados vibracionales, rotacionales o cualquier coordenada de deformación. Durante el proceso de desexcitación estos grados de libertad se transfieren energía. Esta transferencia de energía esta gobernada por un proceso denominado disipación, el cual determina el tiempo que necesita un grado de libertad colectivo para alcanzar el equilibrio. En los modelos de transporte este proceso de disipación es cuantificado por un coeficiente de disipación β. Sin embargo, cabe mencionar que después de siete decadas de investigacion el valor de este coeficiente así como sus posibles dependencias en temperatura o deformación aún estan bajo debate [11]. La razón principal de este debate es que la fisión es un proceso colectivo donde existen muchos grados de libertad y por tanto se necesitan medir varios observables simultaneamente para acotar su valor así como sus posibles dependencias. Sin embargo, la medida simultanea de observables es muy compleja debido a las limitaciones tecnológicas existentes.

Uno de los objetivos de este trabajo fue precisamente superar las estas limitaciones tecnológicas. Hasta ahora, sólo se habían medido observables de forma independiente y usando diferentes dispositivos experimentales que podrían afectar a los resultados. Para evitar discrepancias en los resultados entre los años 50 y 70 se realizaron varios experimentos con el fin de medir diferentes observables en el instituto Laue-Langevin [13] usando reacciones inducidas por neutrones en cinemática directa [14, 15, 173, 174, 175, 176], donde el neutron golpea un núcleo pesado en reposo, a bajas energías cinéticas. Sin embargo, estas medidas sólo permitieron medir el fragmento de fisión más ligero con buena resolución. Estas medidas fueron mejoradas en los años 90, durante los cuales se realizaron diferentes experimentos en el GSI usando el espectrómetro de masas FRS [19] para investigar la fisión inducida por reacciones de espalación en cinemática inversa, es decir, el núcleo es acelerado a altas energías cinéticas y luego se hace incidir sobre un blanco de nucleones o núcleos ligeros. Debido a la cinemática de la reacción, los dos fragmentos de fisión son focalizados en la dirección del haz con alta energía cinética lo cual favorece su identificación en carga y masa. Sin embargo, por razones de aceptancia geométrica el espectrómetro FRS sólo alcanzó a medir uno de los dos fragmentos de fisión. Unos años más tarde, ese dispositivo experimental fue modificado para medir por primera vez la carga de los dos fragmentos de fisión con gran resolución, pero sin medir sus masas, lo cual proporcionó nuevos observables de fisión así como relevante información sobre el proceso de disipación a pequeñas deformaciones [27, 28, 137]. Recientemente esta técnica ha sido mejorada en GANIL usando reacciones de transferencia y fusion [61, 62, 63], donde un espectrometro de masas fue usado para identificar en carga y masa uno de los fragmentos de fisión mientras que el otro sólo fue identificado en carga usando un detector de silicios. Estos experimentos proporcionaron por primera vez identificaciones completas de las distribuciones de carga y masa de algunos núcleos pesados ricos en neutrones, tales como el ^{240}Pu y el ^{250}Cf [62].

Con el fin de mejorar los experimentos anteriores, un nuevo dispositivo experimental fue desarrollado y montado en el GSI [23]. Este dispositivo nos permitió medir por primera vez los dos fragmentos de fisión en carga y masa con gran resolución y alta precisión, así como sus energías cinéticas, proporcionando una completa medida de la cinemática del proceso. Además, este nuevo dispositivo también nos permitió medir las partículas cargadas ligeras en coincidencia con los fragmentos de fisión. Estas medidas nos han permitido obtener observables sensibles al proceso de disipación a pequeñas deformaciones, tales como las secciones eficaces totales de fisión o las anchuras de las distribuciones de carga. Estos observables nos permitieron estudiar la dependencia del coeficiente de disipación con la temperatura y determinar su valor. Por último, hemos definido nuevos observables sensibles al proceso de disipación cuando el sistema fisionante se encuentra altamente deformado, lo cual nos ha permitido estudiar la dependencia de la disipación con la deformación.

Dispositivo experimental

En este experimento, un haz de iones de ^{208}Pb se aceleró hasta energias de 650A MeV con una intensidad del orden de 10^5 iones/s. Estos iones se guiaron desde el acelerador hasta el blanco de reacción. Debido a la cinemática de la reacción, los fragmentos de fisión son emitidos hacia delante con altas energías cinéticas permitiendo su detección con una buena eficiencia. Un nuevo dispositivo experimental fue montado depués del blanco de reacción para medir los fragmentos de fisión en carga y masa y las partículas cargadas ligeras, como mostrado en la Fig. 6.1.

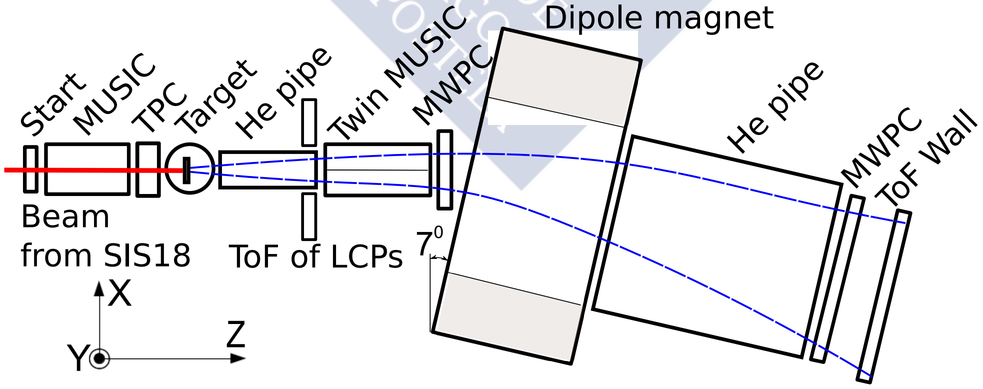

Figure 6.1: *(Color online) Vista esquemática superior del dispositivo experimental usado en este trabajo. Las dimensiones no estan a escala.*

Una doble camara de ionización (Twin MUSIC) fue montada después del blanco para medir el número atómico de los dos fragmentos de fision con una resolución de 0.43 unidades de carga (FWHM). Para determinar las trayectorias de los fragmentos de fisión dentro del imán se usaron los ángulos proporcionandos por la Twin MUSIC, medidos con una resolución entorno a 1 mrad (FWHM), y las posiciones proporcionadas por dos detectores de hilos (MWPCs), medidas con resoluciones inferiores a 1 mm (FWHM), situados antes y después del imán. Al final del dispositivo experimental se situó un detector de tiempo de vuelo con una resolución de 40 ps (FWHM) [179], lo cual fue esencial para identificar las masas de los fragmentos producidos en la reacción. Finalmente, entre el blanco de reacción y la Twin MUSIC se montó un detector de plásticos centelladores para medir las partículas cargadas ligeras emitidas en coincidencia con los fragmentos.

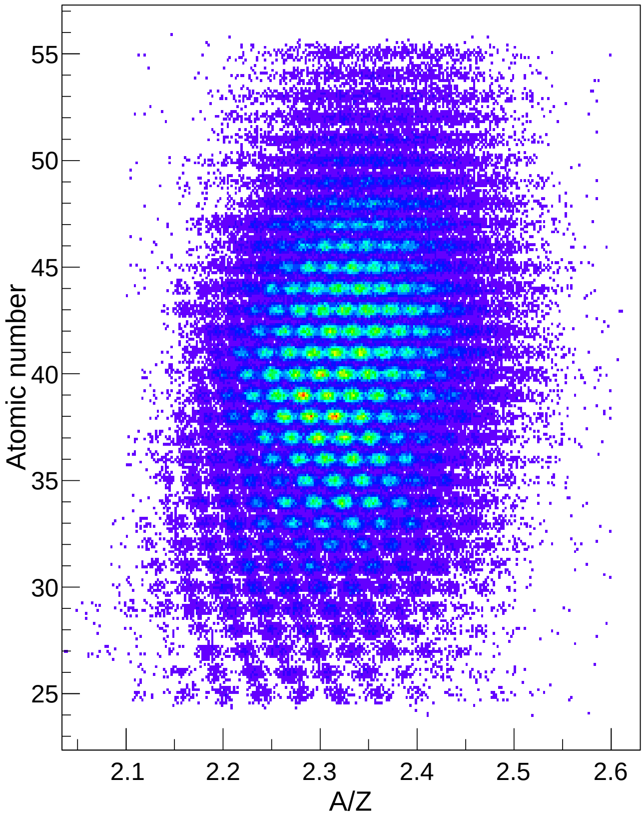

Figure 6.2: *(Color online) Matriz de identificación de los fragmentos de fisión producidos en la reacción* ^{208}*Pb(500A MeV) + p. En la figura se muestran las correlaciones entre el número atómico, determinado a partir de medidas de perdida de energía, y el cociente A/Z, determinado a partir de medidas de rigidez magnética y tiempo de vuelo. La figura proporciona una completa identificación de los fragmentos de fisión producidos en la reacción sin ambigüedades.*

Las masas de los fragmentos de fisión se midieron usando la técnica de separación magnética. Un dipolo magnético (ALADIN) fue usado para curvar las trayectorias de los fragmentos. Estas curvaturas permitieron determinar la rigidez magnética de cada fragmento de fisión por separado, que junto con la velocidad y el número atómico, permitieron obtener la masa (A):

$$A = \frac{eZ}{u}\frac{B\rho}{\beta\gamma c} \tag{6.18}$$

donde Z es el número atómico, B es el campo magnético dentro del imán, ρ es el radio de la trayectoria, u es la unidad atómica de masa, e es la carga del electrón, $\gamma = 1/\sqrt{1 - v^2/c^2}$, v es la velocidad del fragmento de fisión (determinada a partir del tiempo de vuelo) y c es la velocidad de la luz.

En la Fig. 6.2 se muestra la matriz de identificación de los fragmentos de fisión producidos en la reacción ^{208}Pb(500A MeV) + p. Cada cluster o cúmulo estadístico de la figura representa un núcleo. La alta resolución obtenida en este experimento, resoluciones en masa entorno a 0.63 unidades de masa (FWHM), nos perimitió identificar todos los fragmentos de fisión sin ambigüedades. Esta excelente identificación junto con la medida de la seccion eficaz total de fisión nos permitió determinar las secciones eficaces de producción para más de 300 isótopos, desde el cobalto ($Z = 27$) hasta el telurio ($Z = 52$). Estas nuevas medidas también nos permitieron resolver ciertas discrepacias entre las medidas ya existentes, como será discutido en la siguiente sección.

Dinámica del proceso de fisión hasta el punto de silla

El dispositivo experimental descrito en el apartado anterior nos permitió medir simulataneamente diferentes observables de fisión sensibles a la dinámica del proceso entre el estado fundamental del núcleo compuesto, formado después del proceso de espalación, y el punto de silla (saddle point). En este caso nos centraremos en las secciones eficaces totales de fisión y en las anchuras de la distribucion de carga de los fragmentos (σ_z) como una función del número atómico del núcleo fisionante, obtenido con la suma de los números atómicos de los dos fragmentos $Z_1 + Z_2$.

Las secciones eficaces totales de fisión fueron determinadas usando el cociente entre el número de sucesos de fisión y el de proyectiles, teniendo encuenta el espesor del blanco de reacción. Posteriormente, estos valores fueron corregidos cuidadosamente por diferentes factores, entre los que podemos destacar la eficiencia geométrica, la atenuación del haz y las correcciones debidas a reacciones secundarias, para obtener resultados con una alta precisión.

Las secciones eficaces de fisión medidas en este trabajo para la reacción ^{208}Pb + p a 370A, 500A y 650A MeV son mostradas en la Fig. 6.3 (círculos rellenos), donde también se comparan con medidas obtenidas en otros experimentos. Nuestros resultados confirman las medidas realizadas por Schmidt, Hagebø, Brandt y Enqvist, resolviendo la discrepancia existente entre esas medidas y la realizada por Kotov.

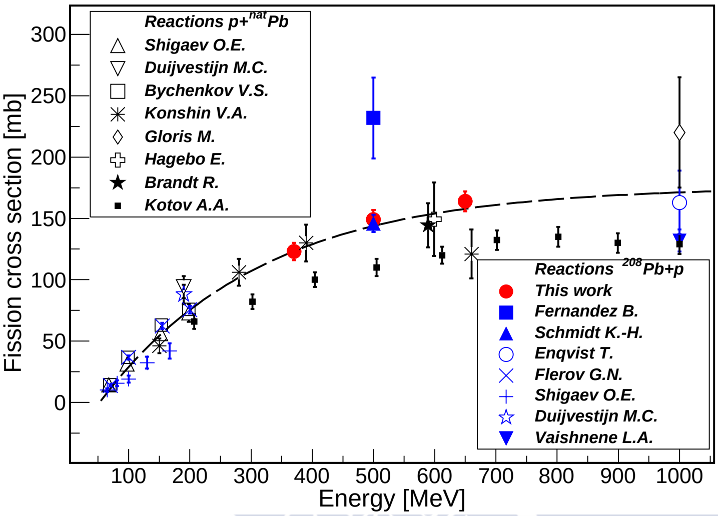

Figure 6.3: *(Color online) Secciones eficaces de fisión medidas en este trabajo para la reacción ^{208}Pb + p (círculos rellenos) comparadas con datos de experimentos anteriores. La linea a trazo es para guiar el ojo.*

Por otro lado, las anchuras de carga nos permiten investigar los efectos disipativos con la energía de excitación del sistema fisionante. Este observable es mostrado en la Fig. 6.4 como una función de $Z_1 + Z_2$ para las reacciones medidas. Uno puede observar que las anchuras de carga son muy parecidas para un sistema fisionante dado, esto nos indica que este observable is independiente del tipo de reacción y que está fuertemente ligado a la temperatura que alcanza el núcleo fisionante en el punto de silla (saddle point) porque crece cuando disminuye el número atómico del sistema fisionante [27, 28, 137].

Este conjunto de datos también se compara con diferentes cálculos para extraer información acerca de la dinámica del proceso. En este trabajo hemos usado dos códigos que nos permiten describir la física del proceso a alta energía de excitación. Para describir el proceso de espalación hemos utilizado un modelo basado en el concepto de la cascada intranuclear, también conocido como INCL4.6 [159], que describe la interacción entre el proton y el núcleo. Para describir la desexcitación de los núcleos compuestos producidos después de la espalación hemos usando el codigo ABLA07 [160] que incluye los efectos disipativos. La comparación de los datos con estos cálculos nos permitió obtener información sobre la densidad nuclear y sobre disipación nuclear, la cual regula la transferencia de energía entre grados de libertad intrínsecos y colectivos durante el proceso de fisión.

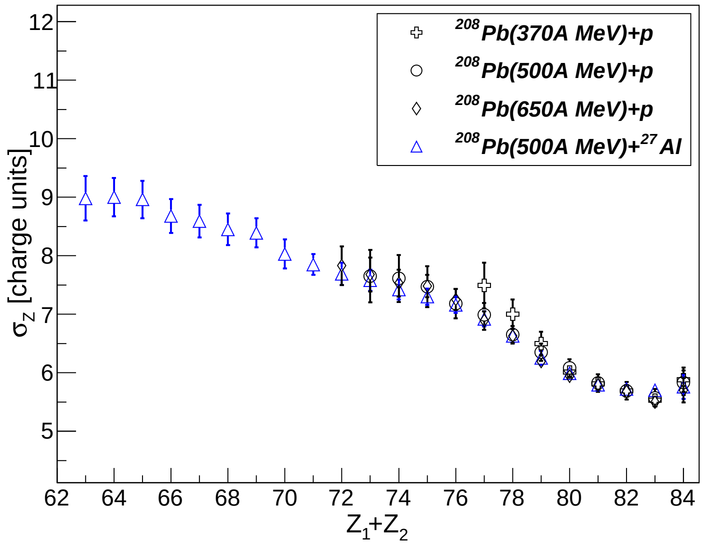

Figure 6.4: *(Color online) Anchura de la distribución de carga de los fragmentos de fisión como una función de $Z_1 + Z_2$ para las reacciones medidas en este trabajo.*

En la Fig. 6.5 se comparan las secciones eficaces de fisión medidas en este trabajo, junto con las obtenidas en experimentos anteriores, con diferentes cálculos. La linea a trazos representa un cálculo basado en el modelo de Kramers [79], el cual asume que la probabilidad de fisión es independiente del tiempo. Claramente este cálculo describe corectamente las secciones eficaces a baja energía donde el tiempo estadístico del proceso es mucho mayor que el transitorio, pero falla a altas energías donde dominan los efectos transitorio lo cual indica una dependencia de la probabilidad de fisión con el tiempo. Esta dependencia fue incluida por Jurado y colaboradores [135] en ABLA07, basandose en una solución analítica de las ecuaciones de Fokker-Planck que describen el proceso. En la figura, los datos también se comparan con diferentes cálculos realizados con ABLA07 pero para diferentes valores del coeficiente de disipación β. De esta comparación, nosotros concluimos que el valor del coeficiente de disipación es $\beta = 4.5 \times 10^{21}$ s^{-1}, lo cual confirma los resultados publicados por otros autores [9, 28, 137].

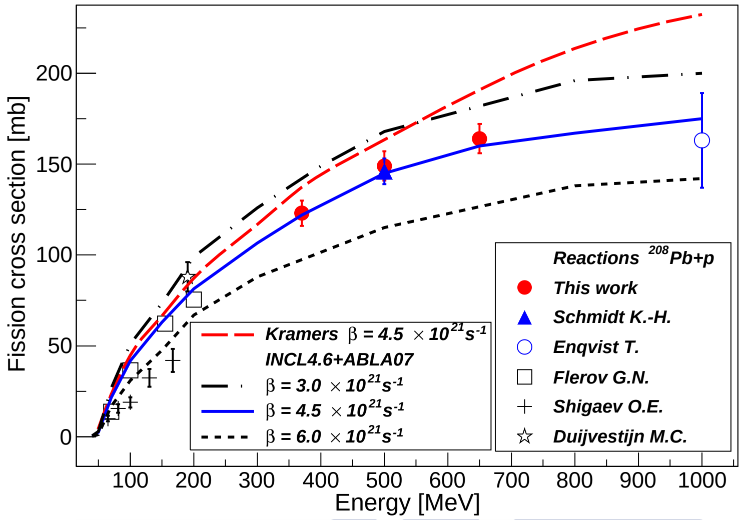

Figure 6.5: *(Color online) Secciones eficaces totales de fisión para la reacción* $^{208}Pb + p$ *como una función de la energía del proton incidente. Las lineas representan diferentes cálculos realizados con el modelo de Kramers y el codigo ABLA07.*

Por otro lado, en algunos trabajos recientes se ha encontrado que un modelo puramente estadístico pero con una densidad de niveles modificada también podria describir las secciones eficaces totales [214]. Para discutir esta posibilidad nosotros hemos usado la anchura de la distribución de carga como función del sistema fisionante Z_1+Z_2, como mostrado en la Fig. 6.6. En este caso, nosotros comparamos los datos con el cálculo anterior que describe las secciones eficaces totales de fisión y con uno asumiendo una probabilidad de fisión puramente estadística junto con un parámetro de densidad de niveles modificado según se describe en la Ref. [214], el cual permite reproducir la sección eficaz total de fisión. Uno puede observar que los cálculos puramente estadísticos junto con una densidad de niveles modificada sobrestiman las anchuras para los sistemas fisionantes más ligeros, mientras que los cálculos que tienen encuenta los efectos disipativos proporcionan una correcta descripción en todo el rango de sistemas fisionantes medidos. Estos resultados confirman que una descripcion puramente estadística, incluso con una densidad de niveles modificada, no puede describir todos los observables.

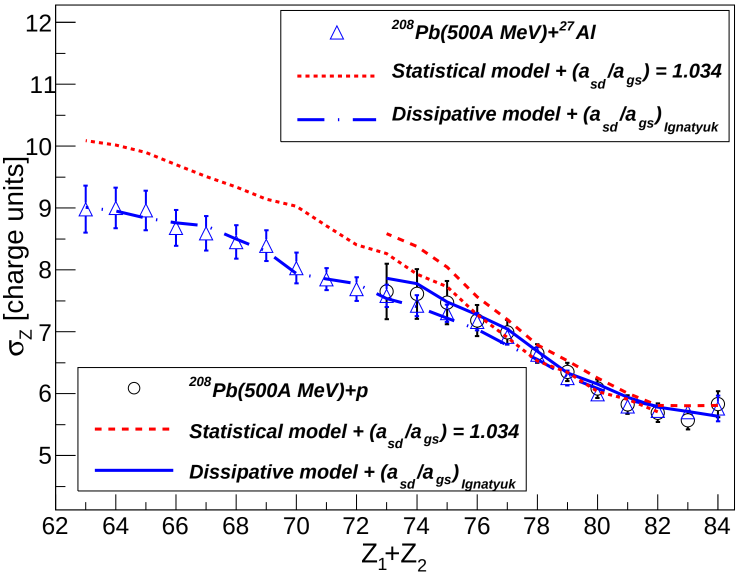

Figure 6.6: *(Color online) Anchura de la distribucion de carga de los fragmentos de fisión como una función de* $Z_1 + Z_2$. *Las lineas representan diferentes cálculos.*

Dinámica del proceso de fisión después del punto de silla

Este trabajo también nos ha permitido investigar la dependencia de la disipación nuclear con la deformación del sistema fisionante. Uno de los observables más usado es la multiplicidad de neutrones. Diferentes trabajos de investigación han encontrado que las multiplicidades de neutrones emitidos antes y después del punto de fisión son sensibles a los efectos disipativos.

Aunque en este trabajo no se ha podido medir las diferentes contribuciones de la emisión de neutrones, la completa medida cinemática de los dos fragmentos de fisión junto con un método de reconstrucción basado en las ecuaciones de Wilkins [172] nos ha permitido determinarlas de forma indirecta, como se muestra en la Fig. 6.7. En el panel inferior se muestran las multiplicidades de neutrones emitidos después del punto de fisión como función del número atómico del sistema fisionante $Z_1 + Z_2$, mientras que en el panel superior se muestran para los neutrones emitidos antes del punto de fisión. Las multiplicidades de neutrones emitidos antes del punto de fisión se obtuvieron a partir de la diferencia entre el número total de neutrones perdidos y los emitidos después del punto de fisión. Estas multiplicidades sólo se representan para $Z_1 + Z_2 > 77$ porque los sistemas más ligeros estan dominados por la emisión de partículas cargadas pesadas que impiden la correcta determinación del número total de neutrones emitidos durante todo el proceso.

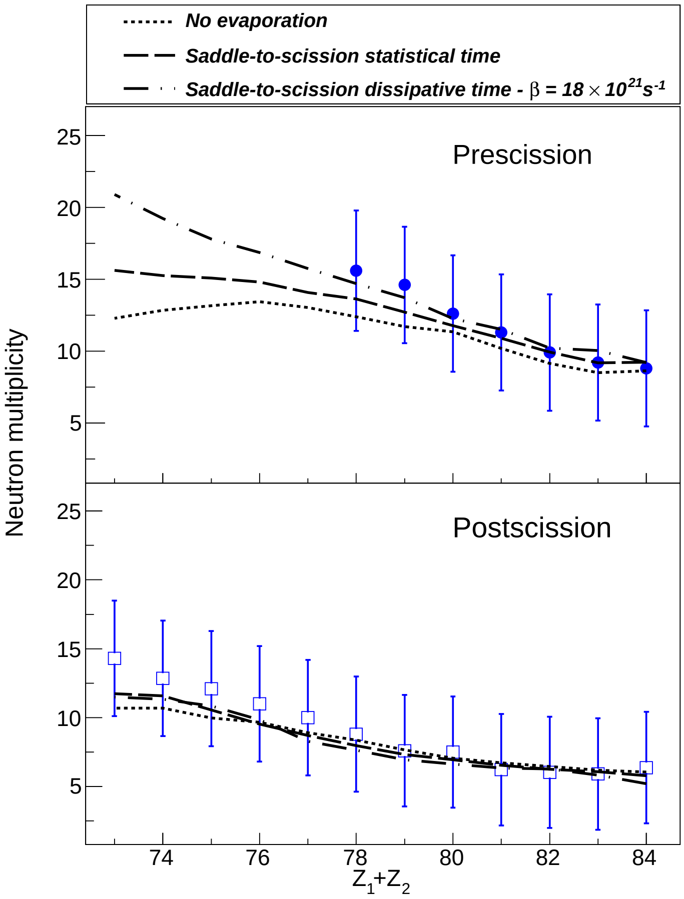

Figure 6.7: *(Color online) La multiplicidad de neutrones emitidos antes (panel superior) y después (panel inferior) del punto de fisión es representada como una función del número atómico del sistema fisionante* $Z_1 + Z_2$*. Las lineas representan diferentes cálculos.*

Las multiplicidades mostradas en la Fig. 6.7 también son comparadas con diferentes cálculos para extraer información sobre la disipación cuando el sistema fisionante se encuentra altamente deformado, es decir, entre el punto de silla (saddle point) y el punto de fisión (scission point). La linea a puntos representa un cálculo asumiendo que no se evaporan partículas entre esos dos puntos. La linea a trazos representa un cálculo asumiendo que el tiempo necesario por el sistema fisionante para moverse entre esos puntos es puramente estadístico. Finalmente, la linea de punto-trazo representa un cálculo considerando efectos disipativos con un coeficiente de disipación $\beta = 18 \times 10^{21}$ s^{-1}. Estos cálculos nos permitieron concluir que las multiplicidades de neutrones emitidos depués del punto de fisión no son sensibles a los efectos de disipación entre el punto de silla y el punto de fisión, mientras que los emitidos antes del punto de fisión si que muestran una ligera sensivilidad, especialmente para los sistemas fisionantes más ligeros donde se alcanzan altas energías de excitación [28]. Sin embargo, la incertidumbre de estas medidas no nos permite acotar el valor del coeficiente de disipación.

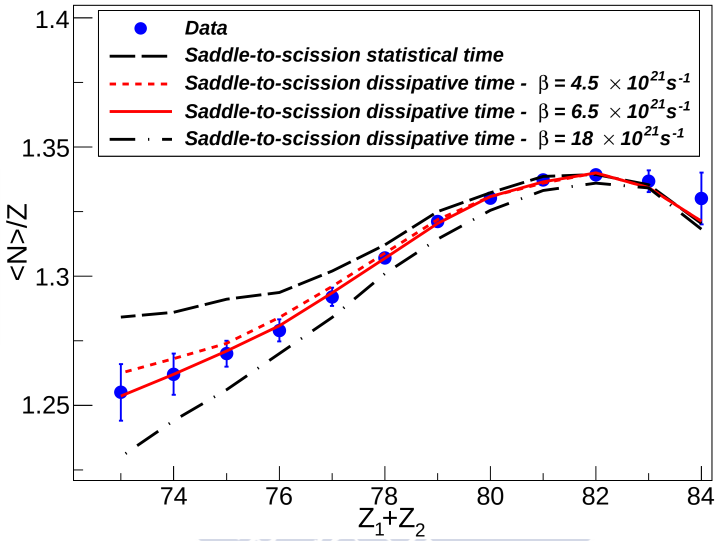

Figure 6.8: *(Color online) Promedio del exceso de neutrones de los fragmentos de fisión como una función del número atómico del sistema fisionante $Z_1 + Z_2$. Las lineas representan diferentes cálculos.*

Por último, este trabajo nos permitió definir un nuevo observable para estudiar los efectos disipativos entre el punto de silla y el punto de fisión. Este nuevo observable es el promedio del exceso de neutrones de los fragmentos de fisión como una función del número atómico del sistema fisionante $Z_1 + Z_2$, como se muestra en la Fig. 6.8. Este observable también fue comparado con diferentes cálculos para estudiar su sensivilidad a los efectos disipativos. La linea a trazos representa un cálculo considerando que el tiempo necesario por el sistema fisionante para deplazarse desde el punto de silla al punto de fisión es puramente estadísitico, el cual claramente sobrestima el exceso de neutrones para los sistemas fisionantes más ligeros. Además, estos datos se compararon con un cálculo considerando efectos disipativos pero para diferentes valores del coeficiente de disipación, lo cual nos perimitio obtener y acotar su valor entorno a $(6.5 \pm 2.5) \times 10^{21}$ s^{-1}. Este resultado podria indicar que el coeficiente de disipación no depende de la deformación ya que del análisis de los observables sensibles a efectos disipativos a pequeña deformación se determinó un valor de $\beta = (4.5 \pm 1.0) \times 10^{21}$ s^{-1}.

Conclusiones

Los resultados presentados en este trabajo representan un primer paso de una nueva generación de medidas del mecanismo de fisión, las cuales proporcionan una completa medida cinemática de los dos fragmentos de fisión y de las partículas ligeras emitidas en coincidencia, lo que suposo un gran reto tecnológico. Estas nuevas medidas nos han permitido definir diferentes observables independientes para estudiar este proceso, en particular para investigar los efectos de la disipación nuclear. Los nuevos observables nos han permitido cuantificar el valor del coeficiente de disipación β y estudiar sus posibles dependencias con la temperatura y la deformación, las cuales estan bajo debate debido a la dificultad de obtener observables sensibles a estos efectos.

Los datos analizados en este trabajo han sido comparados con diferentes cálculos para extraer información sobre la disipación. Para ello hemos dividido los observables en dos grupos, los sensibles a la disipación entre el estado fundamental y el punto de silla y los sensibles a la disipación entre el punto de silla y el punto de fisión. La comparación de las secciones eficaces totales de fisión y de las anchuras de las distribuciones de carga de los fragmentos de fisión con los cálculos nos ha permitido concluir que el valor del coeficiente de disipación es $(4.5 \pm 1.0) \times 10^{21}$ s^{-1} y que este valor no cambia con la temperatura del sistema fisionante. Confirmando la independencia en temperatura.

Para estudiar la dependencia con la deformación hemos usado las multiplicidades de neutrones, que fueron reconstruidas a partir de la cinemática de los dos fragmentos de fisión. Además, las nuevas medidas nos han permitido definir un nuevo observable sensible a la disipación a alta deformación. La comparación de estos dos observables con diferentes cálculos nos ha permitido obtener y acotar el valor de este coeficiente de disipación cuando el sistema fisionante se encuentra altamente deformado, obteniendo un valor entorno a $(6.5 \pm 2.5) \times 10^{21}$ s^{-1}. Su incertidumbre hace que sea compatible con el valor obtenido a pequeña deformación $(4.5 \pm 1.0) \times 10^{21}$ s^{-1}. Por tanto, nuestros resultados nos permiten confirmar la independencia en deformación del coeficiente de disipación.

Appendix A

Isotopic cross sections

The isotopic cross sections of the fission fragments measured in the reaction ^{208}Pb + p at 500A MeV are listed in Table A.1 with their associated uncertainties.

Table A.1: *Isotopic cross sections of the fission fragments measured in the reaction* ^{208}*Pb(500A MeV) +* p *with their associated statistical and systematical uncertainties indicated in parentheses, respectively.*

Z	A	σ [mb]	Z	A	σ [mb]	Z	A	σ [mb]
27	58	0.103(0.025)(0.004)	27	59	0.261(0.024)(0.009)	27	60	0.356(0.025)(0.012)
27	61	0.480(0.032)(0.017)	27	62	0.443(0.033)(0.016)	27	63	0.367(0.028)(0.013)
27	64	0.233(0.021)(0.008)	27	65	0.145(0.016)(0.005)	28	60	0.082(0.020)(0.003)
28	61	0.263(0.035)(0.009)	28	62	0.464(0.035)(0.015)	28	63	0.620(0.040)(0.020)
28	64	0.577(0.032)(0.019)	28	65	0.501(0.028)(0.016)	28	66	0.394(0.023)(0.013)
28	67	0.253(0.021)(0.008)	28	68	0.154(0.023)(0.005)	29	63	0.237(0.020)(0.007)
29	64	0.391(0.024)(0.012)	29	65	0.658(0.033)(0.020)	29	66	0.735(0.036)(0.023)
29	67	0.756(0.037)(0.023)	29	68	0.641(0.033)(0.019)	29	69	0.424(0.029)(0.013)
29	70	0.207(0.018)(0.007)	30	64	0.065(0.010)(0.002)	30	65	0.152(0.013)(0.004)
30	66	0.381(0.021)(0.011)	30	67	0.703(0.032)(0.020)	30	68	0.919(0.037)(0.027)
30	69	0.909(0.039)(0.026)	30	70	0.696(0.031)(0.020)	30	71	0.548(0.031)(0.016)
30	72	0.342(0.021)(0.010)	30	73	0.222(0.022)(0.006)	30	74	0.116(0.016)(0.003)
31	66	0.073(0.011)(0.002)	31	67	0.158(0.013)(0.004)	31	68	0.334(0.020)(0.009)
31	69	0.587(0.023)(0.016)	31	70	1.05(0.04)(0.03)	31	71	1.16(0.04)(0.03)
31	72	1.03(0.04)(0.03)	31	73	0.751(0.028)(0.020)	31	74	0.553(0.024)(0.015)
31	75	0.321(0.019)(0.009)	31	76	0.139(0.012)(0.004)	31	77	0.054(0.009)(0.002)
32	69	0.130(0.012)(0.003)	32	70	0.370(0.021)(0.010)	32	71	0.737(0.031)(0.019)
32	72	1.27(0.04)(0.03)	32	73	1.53(0.05)(0.04)	32	74	1.30(0.04)(0.03)
32	75	1.03(0.03)(0.03)	32	76	0.815(0.033)(0.020)	32	77	0.511(0.024)(0.013)

TABLE A.1 (Continued.)

Z	A	σ [mb]	Z	A	σ [mb]	Z	A	σ [mb]
32	78	0.273(0.020)(0.007)	32	79	0.109(0.012)(0.003)	33	72	0.160(0.011)(0.004)
33	73	0.748(0.031)(0.018)	33	74	1.29(0.04)(0.03)	33	75	1.69(0.05)(0.04)
33	76	1.70(0.04)(0.04)	33	77	1.73(0.04)(0.04)	33	78	1.34(0.04)(0.03)
33	79	0.962(0.034)(0.023)	33	80	0.545(0.029)(0.013)	33	81	0.257(0.017)(0.006)
34	74	0.201(0.013)(0.005)	34	75	0.623(0.031)(0.014)	34	76	1.38(0.05)(0.03)
34	77	1.91(0.05)(0.04)	34	78	2.20(0.05)(0.05)	34	79	2.00(0.04)(0.05)
34	80	1.69(0.04)(0.04)	34	81	1.11(0.03)(0.03)	34	82	0.731(0.029)(0.017)
34	83	0.387(0.026)(0.010)	35	76	0.139(0.011)(0.004)	35	77	0.482(0.022)(0.011)
35	78	0.964(0.039)(0.021)	35	79	1.56(0.05)(0.04)	35	80	2.01(0.05)(0.04)
35	81	2.43(0.05)(0.05)	35	82	2.36(0.05)(0.05)	35	83	1.90(0.05)(0.04)
35	84	1.31(0.04)(0.03)	35	85	0.535(0.024)(0.012)	35	86	0.236(0.020)(0.005)
36	78	0.109(0.008)(0.003)	36	79	0.417(0.023)(0.009)	36	80	1.13(0.04)(0.02)
36	81	2.09(0.06)(0.04)	36	82	2.40(0.05)(0.05)	36	83	2.49(0.05)(0.05)
36	84	2.48(0.05)(0.05)	36	85	2.18(0.05)(0.05)	36	86	1.40(0.04)(0.03)
36	87	0.785(0.032)(0.018)	36	88	0.388(0.024)(0.008)	36	89	0.109(0.012)(0.002)
37	80	0.052(0.004)(0.001)	37	81	0.315(0.018)(0.007)	37	82	0.946(0.035)(0.020)
37	83	1.47(0.04)(0.03)	37	84	2.38(0.052)(0.049)	37	85	2.64(0.049)(0.055)
37	86	2.76(0.052)(0.057)	37	87	2.61(0.052)(0.054)	37	88	1.78(0.049)(0.037)
37	89	1.04(0.034)(0.022)	37	90	0.525(0.024)(0.011)	37	91	0.294(0.018)(0.006)
37	92	0.095(0.010)(0.002)	38	82	0.073(0.009)(0.001)	38	83	0.209(0.012)(0.005)
38	84	0.627(0.021)(0.013)	38	85	1.32(0.03)(0.03)	38	86	2.13(0.04)(0.04)
38	87	2.63(0.05)(0.05)	38	88	2.89(0.05)(0.06)	38	89	2.76(0.06)(0.06)
38	90	2.29(0.05)(0.05)	38	91	1.45(0.04)(0.03)	38	92	1.14(0.04)(0.02)
38	93	0.438(0.020)(0.009)	38	94	0.105(0.009)(0.002)	39	84	0.033(0.007)(0.001)
39	85	0.109(0.007)(0.002)	39	86	0.449(0.018)(0.009)	39	87	1.20(0.03)(0.02)
39	88	2.08(0.04)(0.04)	39	89	2.60(0.04)(0.05)	39	90	2.83(0.05)(0.06)
39	91	2.91(0.06)(0.06)	39	92	2.53(0.05)(0.05)	39	93	1.87(0.05)(0.04)
39	94	0.937(0.026)(0.019)	39	95	0.877(0.030)(0.018)	39	96	0.391(0.020)(0.007)
39	97	0.175(0.012)(0.004)	40	86	0.036(0.008)(0.001)	40	87	0.107(0.010)(0.002)
40	88	0.319(0.013)(0.007)	40	89	0.860(0.024)(0.017)	40	90	1.59(0.03)(0.03)
40	91	2.48(0.05)(0.05)	40	92	2.71(0.05)(0.05)	40	93	2.81(0.05)(0.06)
40	94	2.65(0.05)(0.05)	40	95	2.43(0.05)(0.05)	40	96	1.26(0.03)(0.03)
40	97	0.927(0.030)(0.018)	40	98	0.535(0.023)(0.011)	40	99	0.246(0.017)(0.005)
40	100	0.107(0.012)(0.002)	40	101	0.037(0.006)(0.001)	41	88	0.023(0.009)(0.001)
41	89	0.112(0.012)(0.002)	41	90	0.374(0.021)(0.008)	41	91	0.766(0.024)(0.015)
41	92	1.28(0.03)(0.03)	41	93	1.88(0.04)(0.04)	41	94	2.96(0.06)(0.06)
41	95	2.63(0.05)(0.05)	41	96	2.67(0.05)(0.05)	41	97	2.52(0.05)(0.05)
41	98	1.66(0.04)(0.03)	41	99	1.13(0.03)(0.02)	41	100	0.632(0.024)(0.013)

TABLE A.1 (Continued.)

Z	A	σ [mb]	Z	A	σ [mb]	Z	A	σ [mb]
41	101	0.306(0.015)(0.006)	41	102	0.088(0.007)(0.002)	41	103	0.012(0.002)(0.001)
42	89	0.011(0.001)(0.001)	42	90	0.028(0.016)(0.001)	42	91	0.110(0.016)(0.002)
42	92	0.294(0.016)(0.006)	42	93	0.661(0.027)(0.013)	42	94	1.02(0.03)(0.02)
42	95	1.34(0.03)(0.03)	42	96	2.12(0.05)(0.04)	42	97	2.26(0.04)(0.05)
42	98	2.52(0.05)(0.05)	42	99	2.53(0.05)(0.05)	42	100	2.23(0.05)(0.04)
42	101	1.62(0.04)(0.03)	42	102	0.805(0.026)(0.016)	42	103	0.478(0.021)(0.010)
42	104	0.129(0.009)(0.003)	42	105	0.045(0.006)(0.001)	43	93	0.066(0.007)(0.001)
43	94	0.174(0.014)(0.004)	43	95	0.317(0.018)(0.007)	43	96	0.762(0.029)(0.016)
43	97	1.19(0.03)(0.02)	43	98	1.87(0.04)(0.04)	43	99	2.10(0.04)(0.04)
43	100	2.34(0.05)(0.05)	43	101	2.24(0.05)(0.05)	43	102	2.13(0.05)(0.04)
43	103	1.79(0.04)(0.04)	43	104	1.14(0.03)(0.02)	43	105	0.444(0.018)(0.009)
43	106	0.252(0.016)(0.005)	43	107	0.120(0.011)(0.003)	44	95	0.053(0.008)(0.001)
44	96	0.155(0.015)(0.003)	44	97	0.238(0.016)(0.005)	44	98	0.580(0.024)(0.012)
44	99	0.962(0.028)(0.020)	44	100	1.63(0.04)(0.04)	44	101	1.88(0.04)(0.04)
44	102	2.05(0.04)(0.04)	44	103	2.22(0.05)(0.05)	44	104	2.00(0.04)(0.04)
44	105	1.61(0.04)(0.03)	44	106	1.10(0.03)(0.02)	44	107	0.735(0.029)(0.016)
44	108	0.318(0.017)(0.007)	44	109	0.105(0.009)(0.002)	44	110	0.041(0.005)(0.001)
45	97	0.031(0.011)(0.001)	45	98	0.092(0.016)(0.002)	45	99	0.220(0.020)(0.005)
45	100	0.267(0.014)(0.006)	45	101	0.723(0.027)(0.016)	45	102	1.10(0.03)(0.02)
45	103	1.52(0.04)(0.03)	45	104	1.64(0.04)(0.04)	45	105	1.97(0.04)(0.04)
45	106	1.93(0.05)(0.04)	45	107	1.69(0.04)(0.04)	45	108	1.34(0.04)(0.03)
45	109	0.904(0.036)(0.020)	45	110	0.390(0.021)(0.009)	45	111	0.175(0.012)(0.0039)
45	112	0.051(0.006)(0.001)	46	100	0.053(0.014)(0.001)	46	101	0.105(0.015)(0.002)
46	102	0.211(0.014)(0.005)	46	103	0.421(0.018)(0.010)	46	104	0.865(0.032)(0.020)
46	105	1.28(0.04)(0.03)	46	106	1.61(0.04)(0.04)	46	107	1.77(0.04)(0.04)
46	108	1.60(0.04)(0.04)	46	109	1.40(0.04)(0.03)	46	110	1.20(0.04)(0.03)
46	111	0.926(0.038)(0.022)	46	112	0.526(0.023)(0.012)	46	113	0.211(0.012)(0.005)
46	114	0.084(0.008)(0.002)	46	115	0.042(0.007)(0.001)	47	104	0.151(0.011)(0.004)
47	105	0.311(0.016)(0.008)	47	106	0.613(0.025)(0.015)	47	107	0.984(0.031)(0.024)
47	108	1.26(0.04)(0.03)	47	109	1.38(0.04)(0.03)	47	110	1.39(0.04)(0.03)
47	111	1.33(0.04)(0.03)	47	112	1.23(0.04)(0.03)	47	113	0.934(0.033)(0.023)
47	114	0.522(0.023)(0.013)	47	115	0.231(0.014)(0.006)	47	116	0.131(0.011)(0.003)
47	117	0.070(0.010)(0.002)	48	106	0.100(0.024)(0.003)	48	107	0.212(0.021)(0.005)
48	108	0.479(0.027)(0.012)	48	109	0.785(0.036)(0.020)	48	110	0.984(0.040)(0.025)
48	111	1.10(0.04)(0.03)	48	112	1.11(0.04)(0.03)	48	113	1.10(0.03)(0.03)
48	114	1.02(0.04)(0.03)	48	115	0.845(0.032)(0.022)	48	116	0.669(0.028)(0.017)
48	117	0.299(0.018)(0.008)	48	118	0.105(0.009)(0.003)	49	109	0.193(0.026)(0.005)
49	110	0.324(0.026)(0.009)	49	111	0.505(0.031)(0.014)	49	112	0.680(0.035)(0.018)

TABLE A.1 (Continued.)

Z	A	σ [mb]	Z	A	σ [mb]	Z	A	σ [mb]
49	113	0.822(0.033)(0.022)	49	114	0.951(0.040)(0.026)	49	115	0.909(0.035)(0.025)
49	116	0.891(0.038)(0.024)	49	117	0.755(0.033)(0.021)	49	118	0.524(0.026)(0.014)
49	119	0.253(0.014)(0.007)	49	120	0.133(0.011)(0.004)	49	121	0.084(0.010)(0.002)
50	112	0.147(0.017)(0.004)	50	113	0.291(0.023)(0.008)	50	114	0.423(0.025)(0.012)
50	115	0.632(0.031)(0.018)	50	116	0.668(0.030)(0.019)	50	117	0.759(0.035)(0.022)
50	118	0.729(0.033)(0.021)	50	119	0.662(0.030)(0.019)	50	120	0.529(0.028)(0.015)
50	121	0.341(0.024)(0.009)	51	114	0.107(0.012)(0.003)	51	115	0.207(0.020)(0.006)
51	116	0.284(0.019)(0.090)	51	117	0.392(0.026)(0.012)	51	118	0.497(0.030)(0.015)
51	119	0.553(0.029)(0.017)	51	120	0.568(0.030)(0.018)	51	121	0.562(0.032)(0.017)
51	122	0.457(0.027)(0.014)	51	123	0.340(0.021)(0.010)	51	124	0.185(0.016)(0.006)
51	125	0.078(0.009)(0.002)	52	116	0.084(0.015)(0.003)	52	117	0.144(0.020)(0.005)
52	118	0.192(0.021)(0.007)	52	119	0.266(0.022)(0.008)	52	120	0.329(0.023)(0.011)
52	121	0.381(0.024)(0.012)	52	122	0.464(0.033)(0.015)	52	123	0.401(0.026)(0.013)
52	124	0.327(0.020)(0.011)	52	125	0.226(0.018)(0.007)	52	126	0.164(0.014)(0.005)
52	127	0.086(0.010)(0.003)	52	128	0.034(0.005)(0.001)			

Bibliography

[1] O. Hahn and F. Strassmann, Nature **27**, 11 (1939).

[2] N. Bohr and J. A. Wheeler, Phys. Rev. **56**, 426 (1939).

[3] D. Hilscher and H. Rossner, Ann. Phys. (Paris) **17**, 471 (1992).

[4] M. Thoennessen et al., Phys. Rev. Lett. **71**, 4303 (1993).

[5] D. J. Hofman et al., Phys. Rev. C **51**, 2597 (1995).

[6] J. P. Lestone, Phys. Rev. Lett. **70**, 2245 (1993).

[7] K. X. Jing et al., Phys. Lett. B **518**, 221 (2001).

[8] J. P. Lestone and S. G. McCalla, Phys. Rev. C **79**, 044611 (2009).

[9] W. Ye and N. Wang, Phys. Rev. C **87**, 014610 (2013).

[10] H. A. Weidenmüller, Prog. Part. Nucl. Phys. **3**, 49 (1980).

[11] D. Jacquet and M. Morjean, Prog. Part. Nucl. Phys. **63**, 155 (2009).

[12] A. V. Prokofiev, Nucl. Instrum. Methods Phys. Res., Sect. A **463**, 557 (2001).

[13] E. Moll et al., Nucl. Instrum. Methods **139**, 213 (1976).

[14] G. Siegert, H. Wollnik, J. Greif, R. Decker, G. Fiedler, and B. Pfeiffer, Phys. Rev. C **14**, 1864 (1976).

[15] W. Lang, H. G. Clerc, H. Wohlfarth, H. Schrader, and K.-H. Schmidt, Nucl. Phys. A **345**, 34 (1980).

[16] A. Turkevich and J. B. Niday, Phys. Rev. **84**, 52 (1951).

[17] I. Nishinaka et al., Phys. Rev. C **56**, 891 (1997).

[18] A. Bail et al., Phys. Rev. C **84**, 034605 (2011).

[19] H. Geissel et al., Nucl. Instrum. Methods Phys. Res., Sect. B **70**, 286 (1992).

[20] K.-H. Schmidt, J. Benlliure, and A. R. Junghans, Nucl Phys. A **693**, 169 (2001).

[21] T. Enqvist et al., Nucl. Phys. A **686**, 481 (2001).

[22] M. Bernas et al., Nucl. Phys. A **725**, 213 (2003).

[23] G. Boutoux et al., Phys. Procedia **47**, 166 (2013).

[24] E. Pellereau, Contribution à la mise en place, à la réalisation, et à l'analyse des données de rendements de fission issues de l'expérience SOFIA au GSI, Ph.D. thesis, Université Paris-Sud (2013).

[25] J.-F. Martin, Coulex fission of ^{234}U, ^{235}U, ^{237}Np, and ^{238}Np studied within the SOFIA experimental program, Ph.D. thesis, Université Paris-Sud (2014).

[26] T. Gorbinet et al., Phys. Procedia **64**, 101 (2015).

[27] B. Jurado, C. Schmitt, K.-H. Schmidt, J. Benlliure, T. Enqvist, A. R. Junghans, A. Kelić, and F. Rejmund, Phys. Rev. Lett. **93**, 072501 (2004).

[28] Y. Ayyad et al., Phys. Rev. C **91**, 034601 (2015).

[29] http://www.fair-center.eu

[30] A. Gavron et al., Phys. Rev. C **13**, 2374 (1976).

[31] K. A. Petrzhak et al., Zh. Esksp. Teor. Fiz. **10**, 1013 (1940).

[32] S. M. Polikanov et al., Sov. Phys. JETP **15**, 1062 (1962).

[33] V. I. Kuznetsov et al., Sov. J. Nucl. Phys. **4**, 202 (1967).

[34] A. N. Andreyev et al., Phys. Lett. B **312**, 49 (1993).

[35] K.-H. Schmidt et al., Nucl. Phys. A **665**, 221 (2000).

[36] L. Csige et al., Phys. Rev. C **87**, 044321 (2013).

[37] G. Boutoux et al., EPJ Web Conf. **17**, 06005 (2011).

[38] J. E. Escher et al., Rev. Mod. Phys. **84**, 353 (2012).

[39] N. Colonna, F. Belloni, E. Berthoumieux et al., Energy Environ. Sci. **3**, 1910 (2010).

[40] C. Paradela et al., Phys. Rev. C **82**, 034601 (2010).

[41] M. Calviani et al., Nucl. Instrum. Methods Phys. Res., Sect. A **594**, 220 (2008).

[42] J. Pancin et al., Nucl. Instrum. Methods Phys. Res., Sect. A **524**, 102 (2004).

[43] D. Tarrio et al., Nucl. Data Sheets **119**, 35 (2014).

[44] C. Paradela et al., Phys. Rev. C **91**, 024602 (2015).

[45] M. Mac Innes, M.B. Chadwick, and T. Kawano, Nucl. Data Sheets **112**, 3135 (2014).

[46] C. Bhatia et al., Phys. Rev. C **91**, 064604 (2015).

[47] V. P. Eismont et al., Phys. Rev. C **53**, 2911 (1996).

[48] P. Salvador-Castiñeira, T. Bryś, R. Eykens, F.-J. Hambsch, A. Göök, A. Moens, S. Oberstedt, G. Sibbens, D. Vanleeuw, M. Vidali, and C. Pretel, Phys. Rev. C **92**, 014620 (2015).

[49] I. V. Ryzhov et al., Phys. Rev. C **83**, 054603 (2011).

[50] C. Budtz-Jørgensen, H.-H. Knitter, C. Straede, F.-J. Hambsch, and R. Vogt, Nucl. Instrum. Methods Phys. Res. Sect. A **258**, 209 (1987).

[51] A. Al-Adili, F.-J. Hambsch, S. Oberstedt, S. Pomp, and S. Zeynalov, Nucl. Instrum. Methods Phys. Res. Sect. A **624**, 684 (2010).

[52] E. Kugler, Hyperfine Interact **129**, 23 (2000).

[53] V. N. Fedosseev et al., Rev. Sci. Instrum. **83**, 02A903 (2012).

[54] A. N. Andreyev et al., Phys. Rev. Lett. **105**, 252502 (2010).

[55] J. Elseviers et al., Phys. Rev. C **88**, 044321 (2013).

[56] L. Ghys et al., Phys. Rev. C **90**, 041301(R) (2014).

[57] J. Äystö, P. Taskinen, M. Yoshii, J. Honkanen, P. Jauho, J. Ärje, K. Valli, Nucl. Instrum. Methods Phys. Res., Sect. B **26**, 394 (1987).

[58] W. F. Mueller et al., Phys. Rev. C **61**, 054308 (2000).

[59] H. Kudo, M. Maruyama, M. Tanikawa, T. Shinozuka, M. Fujioka, Phys. Rev. C **57**, 178 (1998).

[60] A. Astier et al., Nucl. Instrum. Methods Phys. Res., Sect. B **70**, 233 (1992).

[61] F. Farget et al., J. Phys.: Conf. Ser. **420**, 012119 (2013).

[62] M. Caamaño et al., Phys. Rev. C **88**, 024605 (2013).

[63] C. Rodríguez-Tajes et al., Phys. Rev. C **89**, 024614 (2014).

[64] M. Caamaño et al., Phys. Rev. C **92**, 034606 (2015).

[65] H. Savajols (VAMOS Collaboration), Nucl. Instrum. Methods Phys. Res., Sect. B **204**, 146 (2003).

[66] http://www-aladin.gsi.de

[67] T. Ichikawa et al., Phys. Rev. C **86**, 024610 (2012).

[68] P. Armbruster, Rep. Prog. Phys. **62**, 465 (1999).

[69] I. Panov et al., Nucl. Phys. A **747**, 633 (2005).

[70] H. Nifenecker et al., Nucl. Instrum. Methods Phys. Res., Sect. A **463**, 428 (2001).

[71] C. D. Bowman, Annu. Rev. Nucl. Part. Sci. **48**, 505 (1998).

[72] A. L. Goodman, Adv. Nucl. Phys. **11**, 263 (1979).

[73] B. Avez, C. Simenel, and Ph. Chomaz, Phys. Rev. C **78**, 044318 (2008).

[74] G. Scamps and D. Lacroix, Phys. Rev. C **87**, 014605 (2013).

[75] Y. Tanimura, D. Lacroix, and G. Scamps, Phys. Rev. C **92**, 034601 (2015).

[76] G. F. Bertsch and S. Das Gupta, Phys. Rep. **160**, 189 (1988).

[77] W. Nörenberg, Nucl. Phys. A **428**, 177c (1984).

[78] Y. Abe, C. Gregoire, H. Delagrange, J. Phys. Colloques **47**, C4-329 (1986).

[79] H. A. Kramers, Physica **7**, 284 (1940).

[80] L. Meitner and O. R. Frisch, Nature **143**, 239 (1939).

[81] S. Cohen, F. Plasil, and W. J. Swiatecki, Ann. Phys. (New York) **82**, 557 (1974).

[82] M. Beckerman and M. Blann, Phys. Rev. Lett. **38**, 272 (1977).

[83] M. Blann, Phys. Rev. Lett. **49**, 505 (1982).

[84] H. J. Krappe, J. R. Nix, and A. J. Sierk, Phys. Rev. Lett. **42**, 215 (1979).

[85] A. J. Sierk, Phys. Rev. C **33**, 2039 (1986).

[86] W. J. Swiatecki, Phys. Rev. **100**, 937 (1955).

[87] V. Strutinsky, Nucl. Phys. A **95**, 420 (1967).

[88] N. Carjan, A. J. Sierk, and J. R. Nix, Nucl. Phys. A **452**, 381 (1986).

[89] H. J. Mang, Phys. Rep. **18** 325 (1975).

[90] J. F. Berger, M. Girod, and D. Gogny, Nucl. Phys. A **428**, 23c (1984).

[91] H. Goutte, J. F. Berger, P. Casoli, and D. Gogny, Phys. Rev. C **71**, 024316 (2005).

[92] T. H. R. Skyrme, Nucl. Phys. **9**, 635 (1959).

[93] J. Dechargé and D. Gogny, Phys. Rev. C **21**, 1568 (1980).

[94] J. R. Huizenga and L. G. Moretto, Ann. Rev. Nucl. Part. Sci. **22**, 427 (1972).

[95] T. von Egidy, H. H. Schmidt, and A. N. Behkami, Nucl. Phys. A **481**, 189 (1988).

[96] A. V. Ignatyuk et al., Yad. Fiz **21**, 485 (1975) [Sov. J. Nucl. Phys. **21**, 255 (1975)].

[97] S. Hilarei and S. Goriely, Nucl. Phys. A **779**, 63 (2006).

[98] B. Nerlo-Pormorska and K. Pormorski, Int. J. Mod. Phys. E **15**, 471 (2006).

[99] B. Krusche and K. P. Lieb, Phys. Rev. C **34**, 2103 (1986).

[100] A. Gilbert and A. G. W. Cameron, Can. J. Phys. **43**, 1446 (1965).

[101] H. A. Bethe, Rev. Mod. Phys. **9**, 69 (1937).

[102] A. V. Ignatyuk, K. K. Istekov and G. N. Smirenkin, Yad. Fiz. **29**, 875 (1979) [Sov. J. Nucl. Phys. **29**, 450 (1979)].

[103] P. Möller, J. R. Nix, W. D. Myers, and W. J. Swiatecki, At. Nucl. Data Tables **59**, 185 (1995).

[104] J. Töke and W. J. Swiatecki, Nucl. Phys. A **372**, 141 (1981).

[105] A. V. Ignatyuk, M. G. Itkis, V. N. Okolovich, G. N. Smirenkin, and A. S. Tishin, Yad. Fiz **21**, 1185 (1975) [Sov. J. Nucl. Phys. **21**, 612 (1975)].

[106] S. Bjornholm et al., Proc. third IAEA Symp. on the physics, chemestry of fission, Roechester, NY, 13-17 August 1973, vol. **1** (IAEA, Viena, 1974) p. 367.

[107] J. R. Huizenga et al., Nucl. Phys. A **223**, 589 (1974).

[108] A. R. Junghans et al, Nucl. Phys. A **629**. 635 (1998).

[109] V. F. Weisskopf and D. H. Ewing, Phys. Rev. **57**, 472 (1940).

[110] D. J. Hinde et al., Phys. Rev. Lett. **52**, 986 (1984), erratum: **53**, 2275 (1984).

[111] A. Gavrom et al., Phys. Lett. B **176**, 312 (1986).

[112] W. P. Zank et al., Phys. Rev. C **33**, 519 (1986).

[113] H. Rossner et al., Phys. Rev. C **45**, 719 (1992).

[114] D. J. Hinde et al., Phys. Rev. C **39**, 2268 (1989).

[115] J. P. Lestone, Phys. Rev. Lett. **67**, 1078 (1991).

[116] M. Thoennessen et al., Phys. Rev. Lett. **59**, 2860 (1987).

[117] R. Butsch et al., Phys. Rev. C **41**, 1530 (1990).

[118] C. R. Morton et al., Phys. Rev. C **52**, 243 (1995).

[119] P. Grangé, S. Hassani, H. A. Weidenmüller, A. Gavron, J. R. Nix, and A. J. Sierk, Phys. Rev. C **34**, 209 (1986).

[120] K. H. Bhatt, P. Grangé, and B. Hiller, Phys. Rev. C **33**, 954 (1986).

[121] H. Hofmann and J. R. Nix, Phys. Lett. B **122**, 117 (1983).

[122] S. Hassani and P. Grangé, Phys. Lett. B **137**, 281 (1984).

[123] D. J. Hinde et al., Phys. Rev. C **45**, 1229 (1992).

[124] A. Einstein, Ann. Phys. **17**, 549 (1905).

[125] D. H. E. Gross, Nucl. Phys. A **240**, 472 (1975).

[126] K. T. R. Davies, Phys. Rev. C **13**, 2835 (1976).

[127] Y. Abe et al., Phys. Rep. **275**, 49 (1996).

[128] V. E. Viola et al., Phys. Rev. C **31**, 1550 (1985).

[129] T. Wada et al., Phys. Rev. Lett. **70**, 3538 (1993).

[130] H. van der Ploeg et al., Phys. Rev. Lett. **75**, 970 (1995).

[131] N. P. Shaw et al., Phys. Rev. C **61**, 044612 (2000).

[132] I. Diószegi et al., Phys. Rev. C **63**, 014611 (2001).

[133] P. Fröbrich et al., Nucl. Phys. A **556**, 281 (1993).

[134] J. Benlliure et al., Nucl. Phys. A **700**, 469 (2002).

[135] B. Jurado, K.-H. Schmidt, and J. Benlliure, Phys. Lett. B **553**, 186 (2003).

[136] C. Schmitt, P. N. Nadtochy, A. Heinz, B. Jurado, A. Kelic, and K.-H. Schmidt, Phys. Rev. Lett. **99**, 042701 (2007).

[137] C. Schmitt, K.-H. Schmidt, A. Kelić, A. Heinz, B. Jurado, and P. N. Nadtochy, Phys. Rev. C **81**, 064602 (2010).

[138] Y. Ayyad et al., Phys. Rev. C **89**, 054610 (2014).

[139] T. Rubehn et al., Phys. Rev. C **54**, 3062 (1996).

[140] J. P. Lestone, Phys. Rev. C **59**, 1540 (1999).

[141] P. N. Nadtochy, G. D. Adeev, and A. V. Karpov, Phys. Rev. C **65**, 064615 (2002).

[142] P. Paul and M. Thoennessen, Ann. Rev. Nucl. Part. Sci. **44**, 65 (1994).

[143] E. Vardaci et al., Eur. Phys. J. A **43**, 127 (2010).

[144] D. J. Hinde et al., Nucl. Phys. A **502**, 497 (1989).

[145] M. G. Itkis, V. N. Okolovich, A. Ya. Rusanov, and G. N. Smirenkin, Sov. J. Part. Nucl. **19**, 301 (1988).

[146] P. Grangé, Li Jun-Qing, and H. A. Weidenmüller, Phys. Rev. C **27**, 2063 (1983).

[147] G. Hansen and A. S. Jensen, Nucl. Phys. A **406**, 236 (1983).

[148] R. Serber, Phys. Rev. **72**, 1114 (1947).

[149] Y. Yariv and Z. Fraenkel, Phys. Rev. C **20**, 2227 (1979).

[150] A. Boudard et al., Phys. Rev. C **66**, 044615 (2002).

[151] J. J. Griffin, Phys. Rev. Lett. **17**, 478 (1966).

[152] N. Metropolis et al., Phys. Rev. **110**, 185 (1958).

[153] N. Metropolis et al., Phys. Rev. **110**, 204 (1958).

[154] J. Cugnon, Nucl. Phys. A **462**, 751 (1987).

[155] D. J. Morrissey et al., Phys. Rev. C **18**, 1267 (1978).

[156] J. J. Gaimard and K.-H. Schmidt, Nucl. Phys. A **531**, 709 (1991).

[157] J. Aichelin and G. Bertsch, Phys. Rev. C **13**, 1730 (1985).

[158] H. Kruse, B. V. Jacak, and H. Stöcker, Phys. Rev. Lett. **54**, 289 (1985).

[159] A. Boudard, J. Cugnon, J. C. David, S. Leray, and D. Mancusi, Phys. Rev. C **87**, 014606 (2013).

[160] A. Kelić, M. V. Ricciardi, and K.-H. Schmidt, Proceedings of Joint ICTP-IAEA Advanced Workshop on Model Codes for Spallation Reactions, ICTP Trieste, Italy, 4-8 February 2008, edited by D. Filges, S. Leray, Y. Yariv, A. Mengoni, A. Stanculescu, and G. Mank (IAEA INDC(NDS)-530, Vienna, 2008), pp. 181-221.

[161] M. V. Ricciardi et al., Phys. Rev. C **73**, 014607 (2006).

[162] C. Villagrasa-Canton et al., Phys. Rev. C **75**, 044603 (2007).

[163] D. Mancusi, A. Boudard, J. Cugnon, J.-C. David, P. Kaitaniemi, and S. Leray, Phys. Rev. C **90**, 054602 (2014).

[164] J. Alcántara-Núñez et al., Phys. Rev. C **92**, 024607 (2015).

[165] L. G. Moretto, Nucl. Phys. A **247**, 211 (1975).

[166] H. Risiken, The Fokker-Planck Equation, Springer-Verlag, Berlin, 1989.

[167] B. Jurado et al., Nucl. Phys. A **747**, 14 (2005).

[168] R. W. Hasse and W. D. Myers, Geometrical Relationships of Macroscopic Nuclear Physics, Springer-Verlag, Berlin, 1988.

[169] J. Benlliure, A. Grewe, M. de Jong, K.-H. Schmidt, and S. Zhdanov, Nucl. Phys. A **628**, 458 (1998).

[170] A. Ya. Rusanov, M. G. Itkis, and V. N. Okolovic, Phys. At. Nucl. **60**, 683 (1997).

[171] P. Armbruster, Nucl. Phys. A **140**, 385 (1970).

[172] B. D. Wilkins, E. P. Steinberg, and R. R. Chasman, Phys. Rev. C **14**, 1832 (1976).

[173] U. Quade et al., Nucl. Phys. A **487**, 1 (1988).

[174] C. Schmitt et al., Nucl. Phys. A **430**, 21 (1984).

[175] D. Rochman et al., Nucl. Phys. A **710**, 3 (2002).

[176] M. Djebara et al., Nucl. Phys. A **496**, 346 (1989).

[177] C. Böckstiegel, S. Steinhäuser, J. Benlliure, H. G. Clerc, A. Grewe, A. Heinz, M. de Jong, A. R. Junghans, J. Müller, and K.-H. Schmidt, Phys. Lett. B **398**, 259 (1997).

[178] E. Pellereau et al., EPJ Web Conf. **62**, 06005 (2013).

[179] A. Ebran et al., Nucl. Instrum. Methods Phys. Res., Sect. A **728**, 40 (2013).

[180] M. Pfützner et al., Nucl. Instrum. Methods Phys. Res., Sect. B **86**, 213 (1994).

[181] R. Janik et al., Nucl. Instrum. Methods Phys. Res., Sect. A **640**, 54 (2011).

[182] B. Voss, Proceedings of the Nuclear Science Symposium and Medical Imaging Conference (NSS/MlC-IEEE, Valencia, Spain, 2011).

[183] C. Finck et al., J. Phys.: Conf. Ser. **50**, 397 (2006).

[184] D. Lee, S. Sobottka, and H. Thiessen. Nucl. Instrum. and Methods **104**, 179 (1972).

[185] L. Barabash et al., Nucl. Instrum. Methods Phys. Res., Sect. A **236**, 271 (1985).

[186] K. Lau and J. Pyrlik. Nucl. Instrum. Methods Phys. Res., Sect. A **366**, 298 (1995).

[187] B. Fernández-Domínguez et al., Nucl. Phys. A **747**, 227 (2005).

[188] A. Kelić et al., Phys. Rev. C **70**, 064608 (2004).

[189] L. Audouin et al., Nucl. Phys. A **768**, 1 (2006).

[190] F. Méot, Nucl. Instrum. Methods Phys. Res., Sect. A **767**, 112 (2014).

[191] http://geant4.cern.ch/

[192] J. L. Rodríguez-Sánchez, H. Álvarez-Pol, Y. Ayyad, J. Benlliure, P. Cabanelas, C. Paradela, GSI Sci. Rep. 2013, p. 153.

[193] D. Bertini, J. Phys.: Conf. Ser. **331**, 032036 (2011).

[194] J. Benlliure, E. Casarejos, J. Pereira, and K.-H. Schmidt, Phys. Rev. C **74**, 014609 (2006).

[195] K.-H. Schmidt et al., Phys. Rev. C **87**, 034601 (2013).

[196] P. J. Karol, Phys. Rev. C **11**, 1203 (1975).

[197] J. L. Rodríguez-Sánchez et al., Phys. Rev. C **90**, 064606 (2014).

[198] G. N. Flerov et al., Sov. J. At. Energy **33**, 1144 (1972).

[199] O. E. Shigaev et al., Khlopin Radiev. Inst., Leningrad Reps., No. **17** (1973).

[200] M. C. Duijvestijn et al., Phys. Rev. C **59**, 776 (1999).

[201] V. S. Bychenkov et al., Sov. J. Nucl. Phys., Vol. **17**, 496 (1973).

[202] V. A. Konshin et al., Yad. Fiz. Vol. **2**, 682 (1965).

[203] M. Gloris, et al., Nucl. Instrum. Methods Phys. Res., Sect. A **463**, 593 (2001).

[204] E. Hagebø and T. Lund, J. Inorg. Nucl. Chem. **37** 1569 (1975).

[205] R. Brandt et al., Rev. Phys. Appl. (Paris) **7**, 243 (1972).

[206] A. A. Kotov et al., Phys. Rev. C **74**, 034605 (2006).

[207] L. A. Vaishnene et al., Z. Phys. A **302**, 143 (1981).

[208] T. Fukahori and S. Pearlstein, Proceedings of the Advisory Group Meeting Organized by IAEA, Vienna, October 9-12, 1990, IAEA Report INDC(NDS)- **245**, p. 93 (1991).

[209] D. Mancusi, A. Boudard, J. Carbonell, J. Cugnon, J.-C. David, and S. Leray, Phys. Rev. C **91**, 034602 (2015).

[210] B. Jurado el al., Nucl. Phys. A **757**, 329 (2005).

[211] S. Chandrasekhar, Rev. Mod. Phys. **15**, 1 (1943).

[212] P. Fröbrich and I. I. Gontchar, Nucl. Phys. A **563**, 326 (1993).

[213] C. Schmitt, B. Jurado, A. R. Junghans, K.-H. Schmidt, and J. Benlliure, Inter. J. of Mod. Phys. E **13**, 97 (2004).

[214] D. Mancusi, R. J. Charity, and J. Cugnon, Phys. Rev. C **82**, 044610 (2010).

[215] S. Lo Meo, D. Mancusi, C. Massimi, G. Vannini, and A. Ventura. Nucl. Phys. A **933**, 43 (2015).

[216] O. A. Shcherbakov et al., J. Nucl. Sci. Technol. Suppl. **2**, 230 (2002).

[217] D. Tarrio et al., Phys. Rev. C **83**, 044620 (2011).

[218] T. Fukahori et al., J. Nucl. Sci. Technol. Suppl. **2**, 25 (2002).

[219] Y. Watanabe et al., J. Korean Phys. Soc., Vol. **59**, 1040 (2011).

[220] J. Randrup and P. Möller, Phys. Rev. C **88**, 064606 (2013).

[221] P. Möller and J. Randrup, Phys. Rev. C **91**, 044316 (2015).

[222] J. Khuyagbaatar et al., Phys. Rev. C **91**, 054608 (2015).

[223] K. Mazurek, C. Schmitt, and P. N. Nadtochy, Phys. Rev. C **91**, 041603(R) (2015).

[224] C. Scheidenberger et al., Nucl. Instrum. Methods Phys. Res., Sect. B **141**, 441 (1998).

[225] T. Enqvist et al., Nucl. Phys. A **703**, 435 (2002).

[226] F. Gönnenwein and B. Börsig, Nucl. Phys. A **530**, 27 (1991).

[227] I. Companis, M. Mirea, and A. Isbasescu, Rom. J. Phys. **56**, 63 (2011).

[228] C. Böckstiegel, S. Steinhäuser, K.-H. Schmidt, H. G. Clerc, A. Grewe, A. Heinz, M. de Jong, A. R. Junghans, J. Müller, and B. Voss, Nucl. Phys. A **802**, 12 (2008).

[229] P. Fröbrich and I. I. Gontchar, Phys. Rep. **292**, 131 (1998).

[230] J. B. Rosser, Theory and Application of $\int_0^z e^{-x^2} dx$ and $\int_0^z e^{-p^2y^2} dy \int_0^y e^{-x^2} dx$. Part I. Methods of Computation, New York, 1948.

[231] J. P. Lestone, Phys. Rev. C **51**, 580 (1995).

[232] P. N. Nadtochy, E. G. Ryabov, and A. E. Gegechkori, Yu. A. Anischenko, and G. D. Adeev, Phys. Rev. C **89**, 014616 (2014).

[233] G. Chaudhuri and S. Pal, Phys. Rev. C **63**, 064603 (2001).

[234] P. Fröbrich, Prog. Theor. Phys. **154**, 279 (2004).

[235] W. F. Henning, http: //asrc.jaea.go.jp/soshiki/gr/chiba_gr/workshop2 /&Henning.pdf

[236] H. Álvarez-Pol, J. Benlliure, E. Casarejos, D. Cortina, I. Durán, and M. Gascón, Nucl. Instrum. Methods Phys. Res., Sect. B **266**, 4616 (2008).

[237] CALIFA/R^{3}B Collaboration. Technical Report for the Design, Construction and Commissioning of the CALIFA Barrel. Technical report, 2011.

[238] CALIFA/R^{3}B Collaboration. Technical Report for the Design, Construction and Commissioning of the CALIFA EndCap. Technical report, 2014.

[239] https://www.gsi.de/work/forschung/nustarenna/nustarenna_divisions/kernreaktionen/activities/r3b.htm

[240] K. Boretzky et al., GSI Sci. Rep. 2011, p. 174.

[241] K. Boretzky et al., GSI Sci. Rep. 2012, p. 190.

[242] M. Bendel et al., J. Phys.: Conf. Ser. **587**, 012049 (2015).

[243] B. Pietras et al., Nucl. Instrum. Methods Phys. Res., Sect. A **729**, 77 (2013).

[244] H. Álvarez-Pol et al., Nucl. Instrum. Methods Phys. Res., Sect. A **767**, 453 (2014).

[245] http://npg.dl.ac.uk/R3B/Project.html


USC
UNIVERSIDADE
DE SANTIAGO
DE COMPOSTELA

This work was partially supported by the European Commission under Project No. ANDES-FP7-249671.